MIZEX

BULLETIN

III. MODELING THE MARGINAL ICE ZONE

MIZEX BULLETIN SERIES: INFORMATION FOR CONTRIBUTORS

The main purpose of the MIZEX Bulletin series* is to provide a permanent medium for the interchange of initial results, data summaries, and theoretical ideas relevant to the Marginal Ice Zone Experiment. This series will be unrefereed and should not be considered a substitute for more complete and finalized journal articles.

Because of the similarity of the physics of the marginal ice zone in different regions, contributions relevant to any marginal ice zone are welcome, provided they are relevant to the overall goals of MIZEX.

These overall goals are discussed in Bulletin I (Wadhams et al., CRREL Special Report 81-19), which described the research strategy, and Bulletin II (Johannesen et al., CRREL Special Report 83-12), which outlined the science plan for the main 1984 summer experiment. Copies of earlier or current bulletins may be obtained from the Technical Information Branch, USA CRREL.

Persons interested in contributing articles to the bulletin should send copies to one of the editors listed below with figures reproducible in black and white. Proofs of the retyped manuscripts will not be sent to the author unless specifically requested.

Science Editors: Technical Editor:

W.D. Hibler III   Maria Bergstad
USA Cold Regions Research and   USA Cold Regions Research
and Engineering Laboratory   and Engineering Laboratory
72 Lyme Road   72 Lyme Road
Hanover, New Hampshire 03755   Hanover, New Hampshire 03755

Peter Wadhams
Scott Polar Research Institute
Lensfield Road
Cambridge CB2 1ER
United Kingdom

Cover: Landsat image of the East Greenland marginal ice zone, the location of the main MIZEX 84 summer experiment.

MIZEX
A Program for Mesoscale Air-Ice-Ocean Interaction Experiments in Arctic Marginal Ice Zones

III. MODELING THE MARGINAL ICE ZONE

William D. Hibler III, Editor

April 1984

PREFACE

The main goal of the marginal ice zone experiment (MIZEX) is to understand the processes that dictate the advance and retreat of the ice margin. Mechanistic model sensitivity studies can greatly aid in this goal by identifying the relative importance of different processes in the total system. In addition, more complete simulation models can be used both to test the adequacy of current understanding of the marginal ice zone and to serve as an integrating device for complex data sets.

This volume contains the main results from a MIZEX modeling workshop held 18-20 October in Hanover, New Hampshire. Modelers interested in both Arctic and Antarctic sea ice were present. The purpose of the workshop was to determine the status of marginal ice zone modeling and to discuss different views on modeling processes in the MIZ. Results from full simulation models, mechanistic models, and empirical statistical models were presented and discussed. In addition, recommendations relevant to experimental measurements were made. The recommendations were divided into ocean, ice, and atmospheric categories; these were also the three main subject areas covered by the presentations.

Overall, the workshop helped to identify areas where further simulations are needed to test our understanding and where knowledge of certain processes is lacking. The workshop also illustrated the paucity of modeling done for this important region to date and accentuated the need for more intense modeling efforts together with data analysis to understand the complex phenomena occurring near the ice edge. As data become available from the main 1984 summer experiment, this process will undoubtedly be accelerated.

W.D. HIBLER III
April 1984

CONTENTS

A Large–Scale Ice/Ocean Model for the Marginal Ice Zone

W.D. HIBLER III
U.S. Army Cold Regions Research and Engineering Laboratory
Hanover, New Hampshire 03755

K. BRYAN
Geophysical Fluid Dynamics Laboratory, Princeton, New Jersey 08540

The growth, drift, and decay of sea ice are closely related to the circulation of the polar oceans. This is especially true in the Greenland and Norwegian Seas in winter where warm northward currents encounter rapidly cooling atmospheric conditions and southward-advancing sea ice. In previous models of the seasonal cycle of Arctic sea ice the ocean has been approximated by a fixed-depth, motionless mixed layer (Washington et al., 1976; Parkinson and Washington, 1979; Hibler, 1980; Hibler and Walsh, 1982) with possibly a small constant heat flux from the deeper ocean or, more recently, by a one-dimensional, variable-thickness mixed layer (Pollard et al., 1983). This approach has also been used in most CO_2 Atmospheric GCM Sensitivity Studies (Manabe and Stouffer, 1980).

In this report, we examine the dominant effects of a more realistic treatment of three-dimensional ocean circulation on seasonal sea ice simulations. For this purpose a diagnostic ice/ocean model is constructed and used to carry out a series of seasonal simulations of the Arctic, Greenland, and Norwegian Seas. The results show that including the ocean circulation yields first-order improvements to the ice margin location and ice velocity fields. Moreover, the improvement in modeling the ice margin requires inclusion of the full three-dimensional circulation of the ocean.

The basic approach in this study is to couple an existing dynamic-thermodynamic sea-ice model (Hibler, 1979, 1980) with a multi-level baroclinic ocean model (Bryan, 1969). The sea-ice model supplies heat flux, salt flux, and momentum exchange boundary conditions for the top of the ocean. The ocean model, in turn, supplies current and heat exchange information to the ice model. Since our main concern here is examining the ef-

fect of ocean circulation on sea ice, observed oceanic temperature and salinity data (Levitus, 1982) are used to weakly force the ocean model so that its equilibrium time scale is similar to that of the ice model (3 to 5 years). This "diagnostic" method allows the ocean model to be forced to available climatological ocean data, while at the same time allowing considerable adjustment in the upper ocean due to the effects of ice/ocean interaction. In addition, the barotropic mode of the ocean is fully simulated so that temporally varying currents due to surface stress fluctuations are part of the model predictions.

The details of the coupling may be briefly outlined as follows. Hibler's (1979, 1980) dynamic–thermodynamic sea-ice model is used to calculate the ice drift, thickness, and compactness. The momentum transfer from the ocean to the ice is determined a) by using the ocean velocity at the second level as the ocean current in the ice calculations (the first level of 30 m thickness in the ocean is a de facto mixed layer), and b) by allowing the surface pressure term in the rigid-lid ocean model to act on the ice in the same manner as sea surface "tilt" in conventional ice dynamic calculations. For the momentum transfer into the ocean, the force due to ice interaction is explicitly calculated by the ice model and subtracted from the wind stress. The remainder is taken to be the wind stress term transferred into the ocean. An important feature of this procedure is that in general the ice will drift in a direction other than the average Ekman motion of the upper 30 m layer of the ocean.

With regard to thermodynamic exchanges, heat transferred by the ocean into the upper mixed layer is used either to melt ice (until the mixed layer returns to freezing) or to warm up the mixed layer if no ice is present. The ice model in turn cal-

culates energy exchanges with the atmoshere, utilizing a complete surface heat budget (Hibler, 1980). For salt fluxes, the amount of melting or freezing of ice is used to supply a salt flux in or out of the ocean. Because the ice model includes advection, annual average salt fluxes at given locations will differ substantially from zero.

The ocean model uses 14 vertical levels with deeper levels of increasing thickness. Bottom topography is resolved by using differing numbers of vertical levels at different locations. The diagnostic forcing to observed data is done at all but the upper level of the ocean with a uniform 3-year relaxation time. In addition, at lateral boundaries of the ocean without land, all levels of the ocean are forced with a 30-day relaxation time over several grid cells closest to the boundary. This procedure follows techniques determined by Sarmiento and Bryan (1982). To simulate river runoff, river inflow was specified seasonally at various boundary locations, yielding mean annual river runoff identical to that employed by Semtner (1976) in a prognostic simulation of the Arctic Ocean without explicit sea ice.

To force the ice model, daily time-varying atmospheric pressure from the FGGE year (Dec. 1978 to Nov. 1979), together with monthly mean climatological temperature and humidity fields, were used. In addition, empirical long- and short-wave radiation calculations (Hibler, 1980) were used in conjunction with these atmosheric data to drive the thermodynamic portion of the model.

Horizontal resolution was taken to be 1.45 ° for the ocean model and 160 km for the ice model. The ocean model was formulated in a spherical grid system with the equator of the grid system going through the geographical North Pole. The ice model on the other hand was formulated in a rectangular grid. However, because of this particular spherical projection, there was little difference between the ice model grid and the ocean grid (specifically, the ice advection terms will yield slight errors in the heat and salt exchanges). In light of the diagnostic forcing of the ocean, these small differences were not felt to be critical.

To obtain seasonally varying equilibrium results, the coupled model was integrated for 5 years using one-day time steps. For comparison, a 5-year simulation was also carried out with an ice-only model, which included only a motionless, fixed-depth, 30-m mixed layer and no ocean currents. In addition, to examine the role of different processes, 1-year sensitivity simulations without surface salt fluxes and without ocean currents were carried out.

Some of the main motion results from the model simulations are shown in Figures 1 through 4. The average annual ice velocity and second-level ocean velocity fields are shown in Figure 1. For a more detailed comparison to observed data, Figure 2a compares observed ice buoy (Thorndike and Colony, 1980) drift to simulated results both with and without the ocean model included, while Figure 2b compares long-term averaged ice and wind stresses. Although of considerable magnitude, the ocean currents are smaller than the ice drift, and in buoy-drift comparisons they account for less than 50% of the net ice drift. While not apparent from this figure, more detailed analyses show both the ice motion and current structure to have considerable temporal variability, with the ice motion varying everywhere, while the main current variability is in shallower regions or near rapid topographic variations.

The main overall effect of the ocean model on the ice drift model is to substantially increase the East Greenland ice drift and to create more of a transpolar drift in the Arctic Basin. Basically, inclusion of the complete ocean model consistently improves turning angles and especially the simulated drift direction and magnitudes of ice drift in the East Greenland Sea. Specifically, for the drift vectors shown in Figure 2a, the average turning angle error in the full model is 23 °, as compared to 38 ° for the ice-only model. The drift magnitudes also show an improvement, with a cumulative magnitude error of 45% for the full model as compared to 58% for the ice-only model.

An important feature of this coupled ice/ocean model is the modification by the ice interaction of the wind stress transferred into the ocean. This effect is particularly pronounced on long time scales since large fluctuations in wind stress tend to average out. Figure 2b shows that in this model the force due to the ice interaction is indeed a major component in the force balance. Note also that, while in most cases the ice stress opposes the wind stress, in some cases it can combine with the wind stress or be at right angles to the ice drift due to the configuration of the land boundary and the ice edge. This result emphasizes the fact that ice interaction effects cannot be modeled by simply modifying free-drift rules and using the local wind. In addition, more detailed analysis shows that the ice interaction can introduce not only magnitude changes but also sign changes in the wind stress and near boundaries. Such effects should be particularly relevant to longer term prognostic ocean simulations, and emphasize the need for better understanding of the nature of ice interaction.
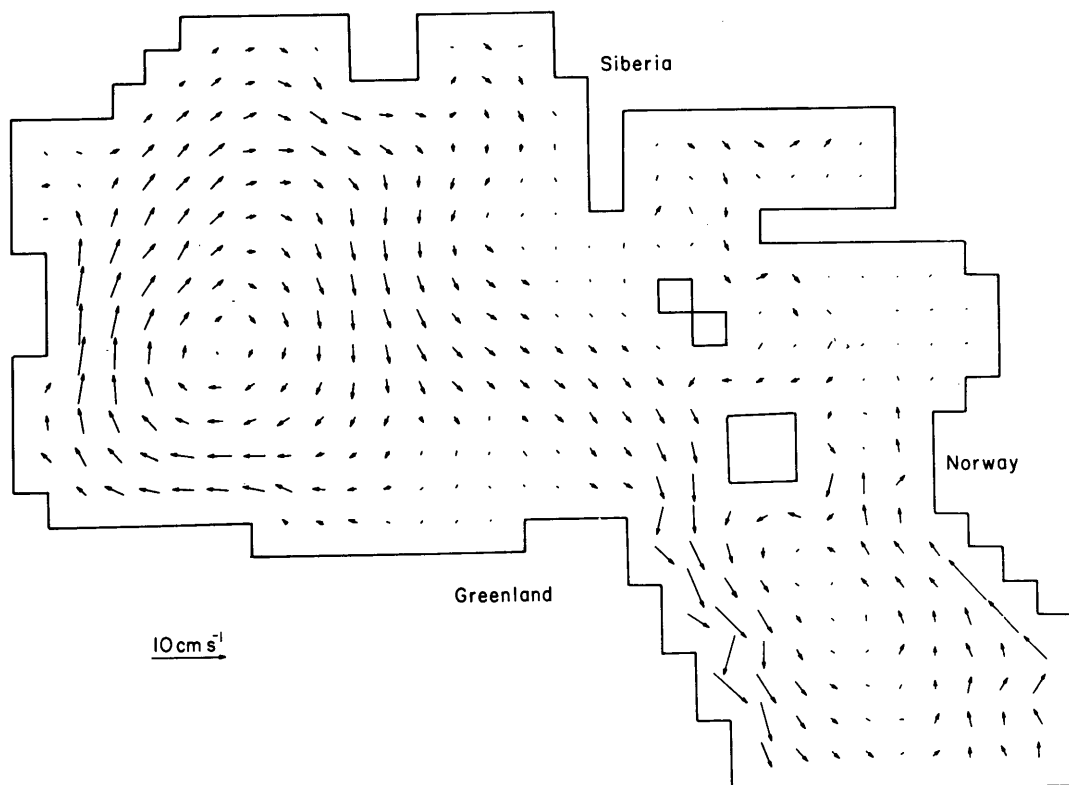
a) The second level of the ocean in the coupled ice ocean model.
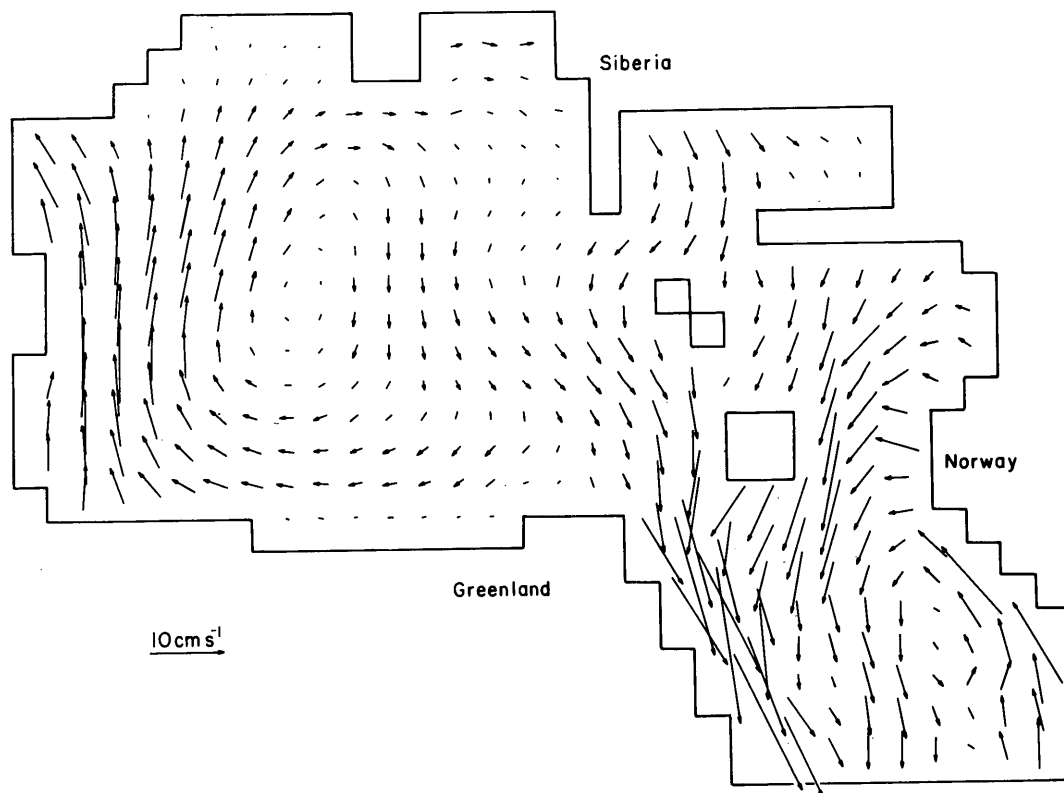
b) The ice motion from the coupled model.

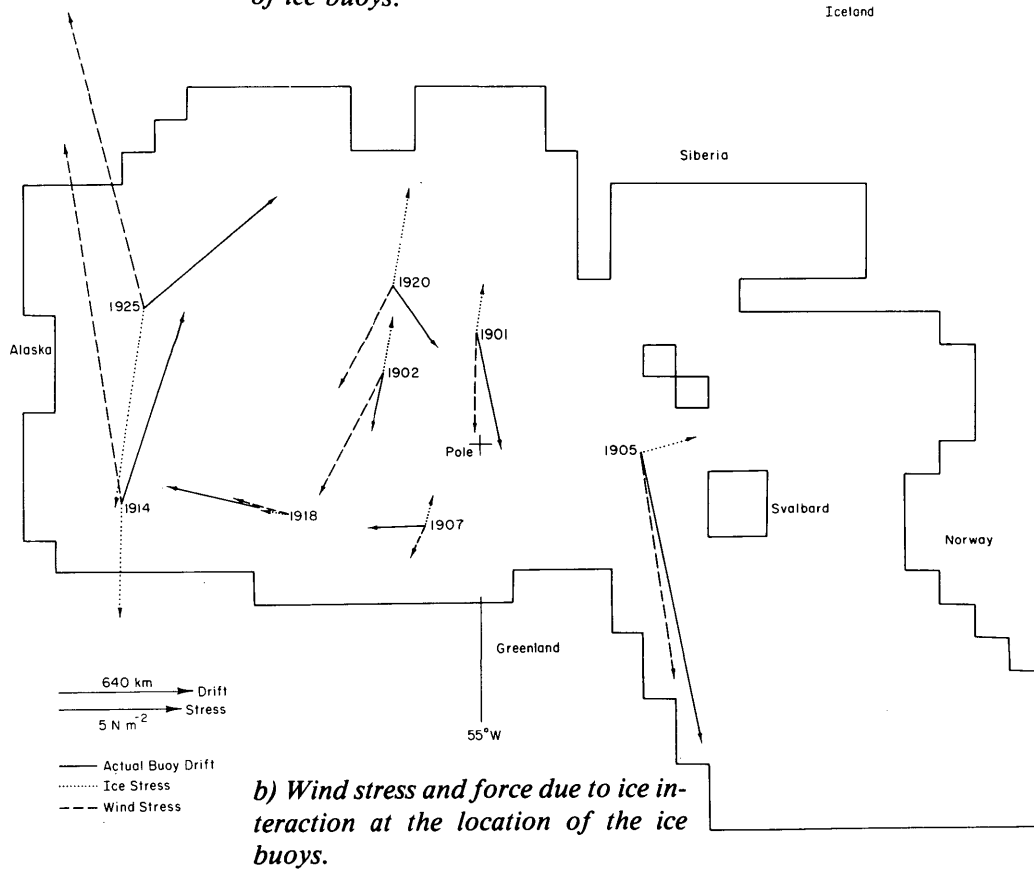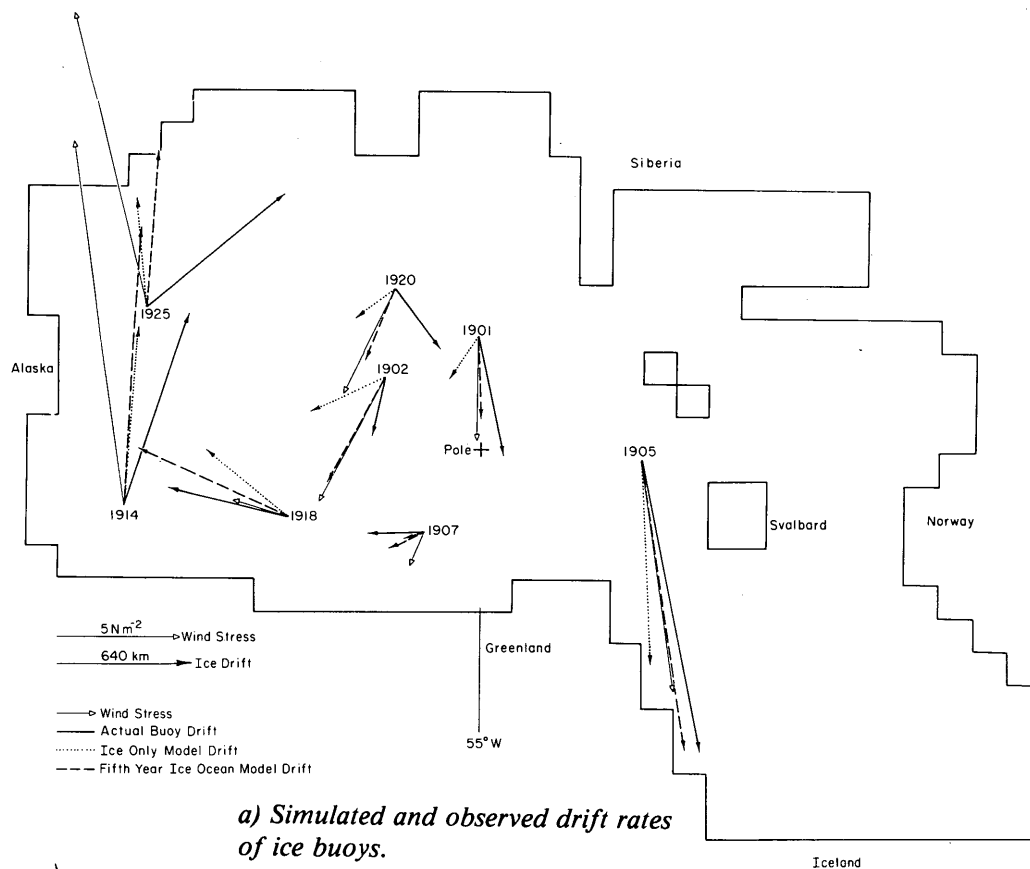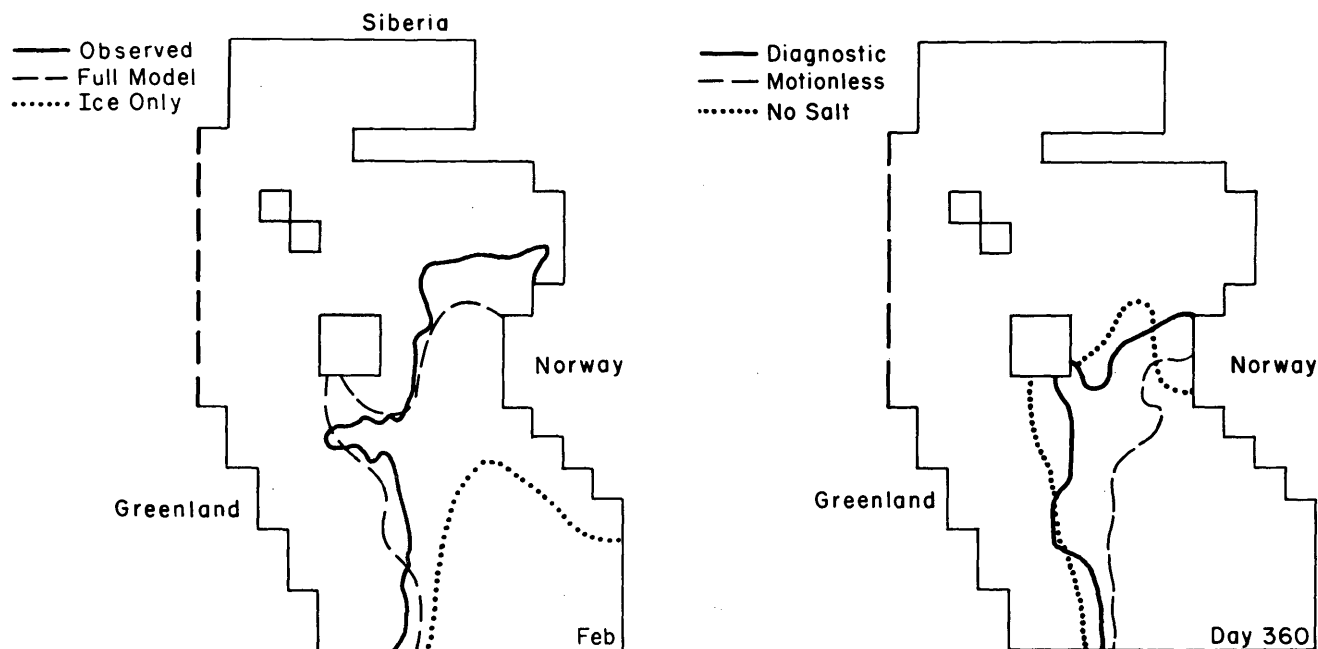Fig. 1. Annual average simulated velocity fields.

3

Fig. 2. Long-term averages of drift rates and wind stress and force. Drift rates have been converted to distances by multiplication by time. The time intervals used were Feb-Nov for buoys 1901 and 1902, Mar-Sept for buoy 1905, May-Nov for buoy 1907, and Mar-Nov for the remaining buoys.

(a) February 50% concentration limits from the full coupled ice ocean model and for the ice-only model, which includes a fixed-depth mixed layer. The observed limit is taken from fleet weather (Suitland, Md., U.S. Navy) charts for the end of February.

(b) Simulated 0.05 m thickness contours for day 360 for the full model, a "motionless" ocean model, and a coupled ice/ocean model with no salt fluxes due to ice freezing and melting. The "motionless" model and the no-salt simulations were run for only 1 year and were initialized to ice thickness and ocean fields at the end of the fourth year of the full diagnostic model simulation.

Fig. 3. Comparisons of simulations of ice concentration and ice thickness.

Probably the most noticeable effect of the modeled ocean circulation is to greatly improve the ice margin simulation, as shown in Figure 3a. This improved ice margin is due to the large oceanic heat flux from the deeper ocean into the upper mixed layer in this region (Fig. 4). The heat flux occurs primarily in winter; analysis shows that much of the enhancement is due to deep convection, which brings up warm water and prevents ice formation in early winter. This convection explains the absence of ice in the full model simulation far from the ice margin.

Near the ice margin a similar physics applies, but the precise location of the ice edge becomes more sensitive to the surface salt balance and to lateral effects in the oceanic circulation. The sensitivity simulations shown in Figure 3b, for example, indicate that the fresh-water flux from melting at the advancing ice edge tends to seal off the ice margin to upward oceanic heat flux and allows a farther advance than would otherwise occur. A sensitivity simulation without lateral motion in the ocean (Fig. 3b) also tends to produce a more excessive edge at the end of one year, since the

lateral transport of heat to both the deep and upper layers is missing. This later result demonstrates the difficulty of simulating the seasonal cycle of sea ice using only a one-dimensional mixed layer model.

A particularly notable feature of these results is the very large value of the oceanic heat flux (see Fig. 4) in the Greenland-Norwegian Seas and the complex way that this heat flux varies in space and time. These results underscore the need for including a full ocean model in seasonal sea-ice simulations.

These simulations also provide a challenge to prognostic ocean models. The realistic results obtained here are partially due to the diagnostic forcing. To sustain these large heat losses in a fully prognostic ocean model requires very substantial northward heat transport. Whether such transports can be successfully simulated remains to be seen.

Finally, the sensitivity of these simulations to salt fluxes from the ice amplifies the need for more detailed examination of the processes dictating the advance and retreat of the ice margin, and the
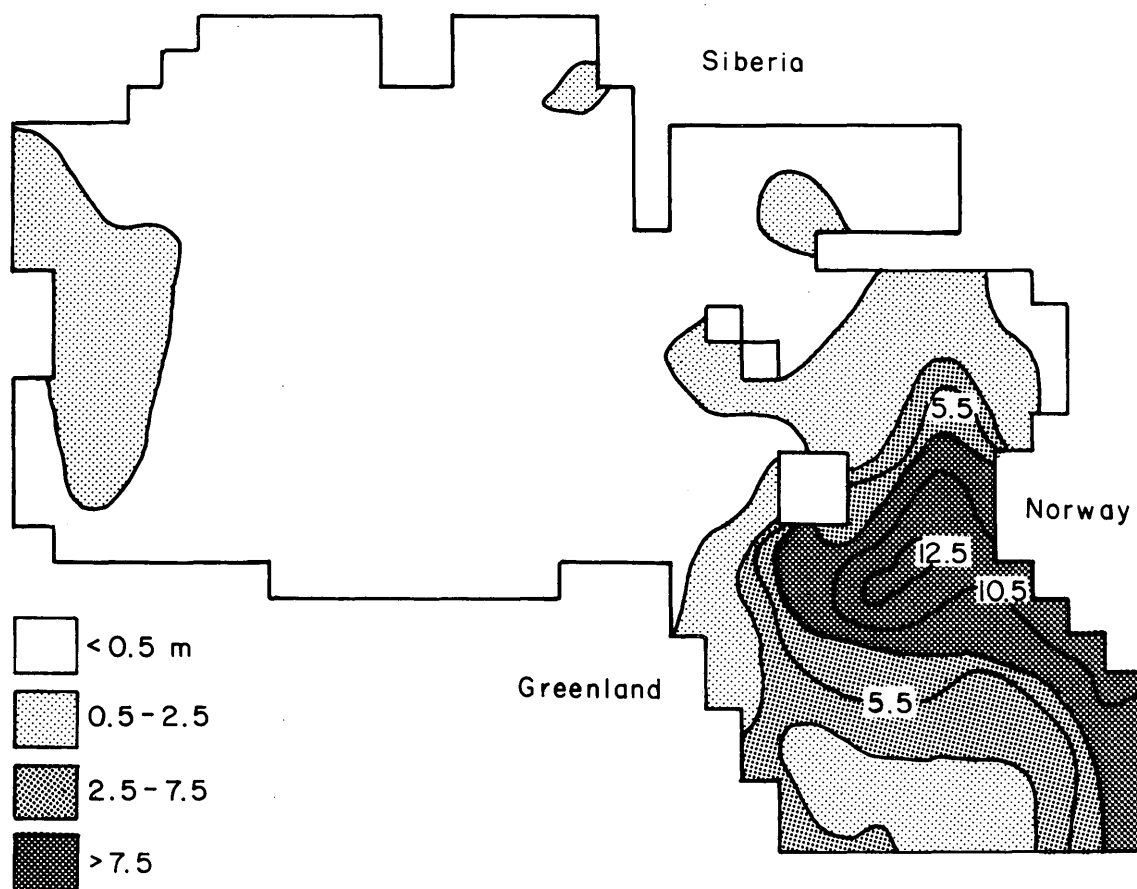
Fig. 4. Average annual heat gained by the upper layer of the ocean from the deeper ocean and by lateral heat transport. The contours are in terms of the melting capacity of the heat in meters of ice per year. For comparison, a melt rate of 1 m of ice per year is equivalent to 9.57 W m^{-2}.

need for the development and verification of more realistic boundary-layer formulations (Lemke, in press) than were used here. Such work is currently under way in the MIZEX program (Johannessen et al., 1983).

This work was supported by NOAA and by the Office of Naval Research.

REFERENCES

Bryan, K., A numerical method for the study of the circulation of the world oceans, *J. Comput. Physics, 4,* 347-376, 1969.

Hibler, W.D. III, A dynamic thermodynamic sea ice model, *J. Phys. Oceanogr., 9,* 815-846, 1979.

Hibler, W.D. III, Modeling a variable thickness sea ice cover, *Mon. Weather Rev., 108,* 1943-1973, 1980.

Hibler, W.D. III, and J.E. Walsh, On modeling seasonal and interannual fluctuations of Arctic Sea ice, *J. Phys. Oceanogr., 12,* 1514-1523, 1982.

Johannessen, O.M., W.D. Hibler III, P. Wadhams, W.J. Campbell, K. Hasselmann, I. Dyer and M. Dunbar, MIZEX, A program for mesoscale air-ice-ocean interaction experiments in Arctic marginal ice zones, II. A science plan for a summer marginal ice zone experiment in the Fram Strait/Greenland Sea, USA Cold Regions Research and Engineering Laboratory, Hanover, N.H., Special Report 83-12, 1983.

Lemke, P., *J. Geophys. Res.,* in press.

Levitus, S., *Climatological Atlas of the World Ocean,* NOAA Professional Paper 13, Rockville, Md., 173 pp., Dec. 1982.

Manabe, S., and R.J. Stouffer, Sensitivity of a global climate model to an increase of CO_2 concentration in the atmosphere, *J. Geophys. Res., 85,* 5529-5554, 1980.

Parkinson, C.L., and W.M. Washington, A large-scale numerical model of sea ice, *J. Geophys. Res., 84,* 311-337, 1979.

Pollard, D., M.L. Batteen and Y.J. Han, Development of a simple upper-ocean and sea ice

model, *J. Phys. Oceanogr., 13,* 754–768, 1983.

Sarmiento, J.L., and K. Bryan, An ocean transport model for the North Atlantic, *J. Geophys. Res., 87,* 394–414, 1982.

Semtner, A.J. Jr., A model for the thermodynamic growth of sea ice in the numerical investigation of climate, *J. Phys. Oceanogr., 6,* 379–389, 1976.

Thorndike, A.S., and R. Colony, *Arctic Ocean Buoy Program, Data Report,* 19 January 1979–31 December 1979, 131 pp., Univ. of Wash., Seattle, 1980.

Washington, W.M., A.J. Semtner, Jr., C. Parkinson, and A.L. Morrison, On the development of a seasonal change sea ice model. *J. Phys. Oceanogr., 6,* 697–685, 1976.

East Greenland Sea Ice Variability
in Large-Scale Model Simulations

J.E. WALSH

Department of Atmospheric Sciences, University of Illinois, Urbana, Illinois 61801

W.D. HIBLER III

U.S. Army Cold Regions Research and Engineering Laboratory
Hanover, New Hampshire 03755

As the primary focus of the MIZEX program, the East Greenland region has recently been the subject of various ice modeling experiments (Vinje, 1977; Wadhams, 1981; Tucker, 1982; Hibler and Bryan, 1984; Johannessen et al., 1983). The observational data show that the seasonal and interannual fluctuations of East Greenland sea ice are substantial. While the relative roles of local and remote forcing in these fluctuations are not well understood, most of the modeling studies cited above have been based on regional simulations of the North Atlantic. Large-scale model simulations provide an alternative approach to the study of East Greenland ice variability in a broader context. In this paper we present some results of large-scale ice model simulations as they pertain to the East Greenland region. The emphasis is on the seasonal and interannual variability of ice thickness, thermodynamic growth and melt, and advective transport over a 20-year period from 1961 to 1980.

Hibler's (1975) two-level dynamic model was used in conjunction with a seven-level thermodynamic treatment based on the formulations of Parkinson and Washington (1979) and Hibler (1980). In place of the mean thickness, h_{eff} of the ice-covered portion of each grid cell, the model now employs seven nonzero thicknesses evenly spaced between 0 and $2h_{eff}$. While a more realistic thickness distribution can be obtained from multi-level dynamic computations (Hibler, 1980) using the ice thickness distribution theory developed by Thorndike et al. (1975), the treatment used here is a first-order attempt to incorporate the strong thickness-dependence of ice growth into the model thermodynamics. The model thermodynamics also includes an explicit treatment of snow cover.

The values used for the conductivity and albedo of snow are 0.31 W m1' °K1' and 0.80, respectively. Snowfall is prescribed according to the smoothed climatological accumulation rates of Parkinson and Washington (1979).

The model was run with a one-day timestep using observed atmospheric forcing data from the years 1961–1980, inclusive. Daily wind fields were computed geostrophically from the NCAR (National Center for Atmospheric Research) set of Northern Hemisphere sea-level pressure analyses. Air temperature anomalies were obtained from the so-called "Russian surface temperature data set" (Robock, 1982), which contains monthly temperature anomalies for the Northern Hemisphere on a 5°×10° latitude-longitude grid. These anomalies were added to the climatological monthly mean temperatures of Crutcher and Meserve (1970) and interpolated bilinearly to the ice model grid. Daily temperatures were then computed by a cubic spline interpolation from the monthly values, which were assumed to correspond to the midpoints of the respective calendar months. Because the Russian temperature tape available for this work ended with December 1976, monthly climatological mean temperatures were used for the final four years, 1976–1980. The monthly means were computed from the temperatures of the first 16 years (1961–1976) of the simulation period. The relative humidities required for the computations of the downcoming longwave radiation were assumed to be 90% at all times and grid points.

The simulations were performed on a 38×31 grid with a resolution of 222 km (Figure 1). The simulations were initialized with thickness fields varying linearly from 0 at the lateral boundaries to 3 m at the center of the grid. A 2-year "spin-up"
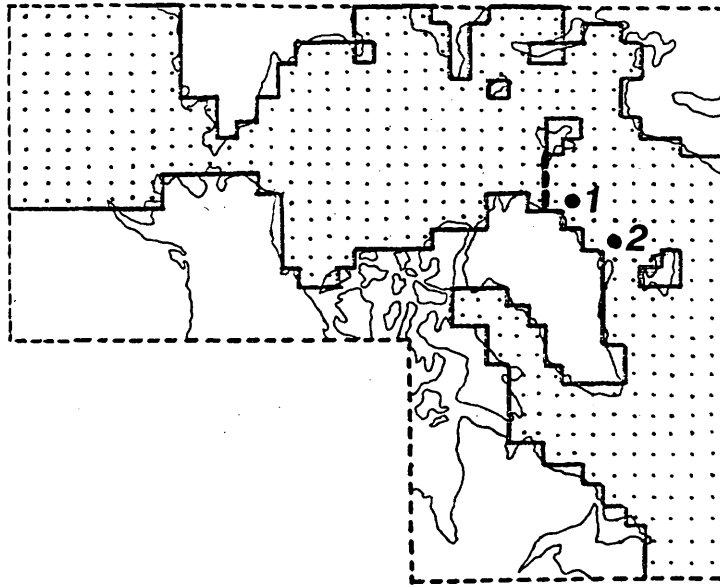
Fig. 1. The model grid. Ice transport into East Greenland Sea was evaluated along dashed transect. Mass budgets for points 1 and 2 are described in text.

using observational data from 1961-62 was performed prior to the 1961-80 simulation. The model was therefore run for 22 years of simulation time, although the results from the 2-year spin-up are not included in the following discussion. Similarly, results from a corresponding simulation without dynamics are not discussed here.

Figure 2 shows the 20-year mean fields of the annual ice thickness *changes* resulting from growth/melt and ice motion. The latter includes advection, convergence or divergence, and a small amount of numerical diffusion. The major regions of ice production (growth) are the water offshore from Alaska and, especially, the Soviet Union. Annual net growth exceeds 1 m in the Laptev Sea and in the northern Bering Sea (Norton Sound) west of Alaska. The major sink region for sea ice is clearly the East Greenland region, where large amounts of ice advection are offset by correspondingly large amounts of ice melt. The annual means of the net melt of advected ice exceed 1.5 m in the water south of Fram Strait.

Figure 2 also illustrates the major discrepancy between the simulated and observed ice extent. The nonzero values of the annual thickness changes in the Norwegian and Barents Seas are indicative of the oversimulation of ice extent in the North Atlantic during the winter. The excessive winter ice coverage in the North Atlantic is attributable primarily to oceanic effects not included in the present simulation. Coupled ice/ocean model experiments performed recently by Hibler

and Bryan (1984) have shown that the position of the North Atlantic ice edge is improved considerably by the inclusion of oceanic processes (currents, deep convection, salinity effects).

The 20-year mean fields of Figure 2 are subject to large interannual fluctuations. The interannual variability is illustrated in Figure 3, which shows the time series of the simulated outflow of ice from the Arctic Basin into the Fram Strait. The plotted values are the mass fluxes across the transect in Figure 1. A strong annual cycle is apparent in the mean seasonal outflow, which is much greater in winter and spring than in summer. The seasonality results from larger ice thicknesses as well as from the stronger wind-induced ice velocities during the winter/spring portion of the year. As a measure of the interannual variability, the annual total outflow (km^3) ranges from 408 (in 1964) and 541 (in 1963) to 2109 (in 1962) and 2118 (in 1975). These large excursions may play significant roles in the mass and salinity budgets of the various subregions of the Arctic and the peripheral seas.

Finally, Figure 4 illustrates the interannual variability of the simulated April ice thicknesses at two grid points (see Figure 1) near the location of the 1983-84 MIZEX field experiments. (April thicknesses were chosen for the illustrations because the maximum ice thickness is generally achieved in April.) The April thicknesses vary considerably on an interannual basis at both points: from 1.5 to 3.5 m at point 1, and from 1.2 to 2.5 m

10
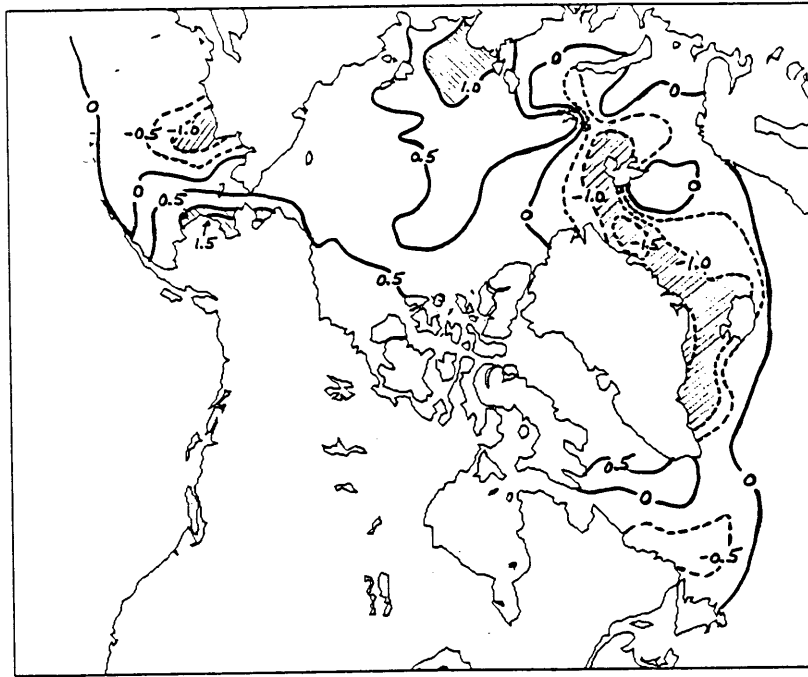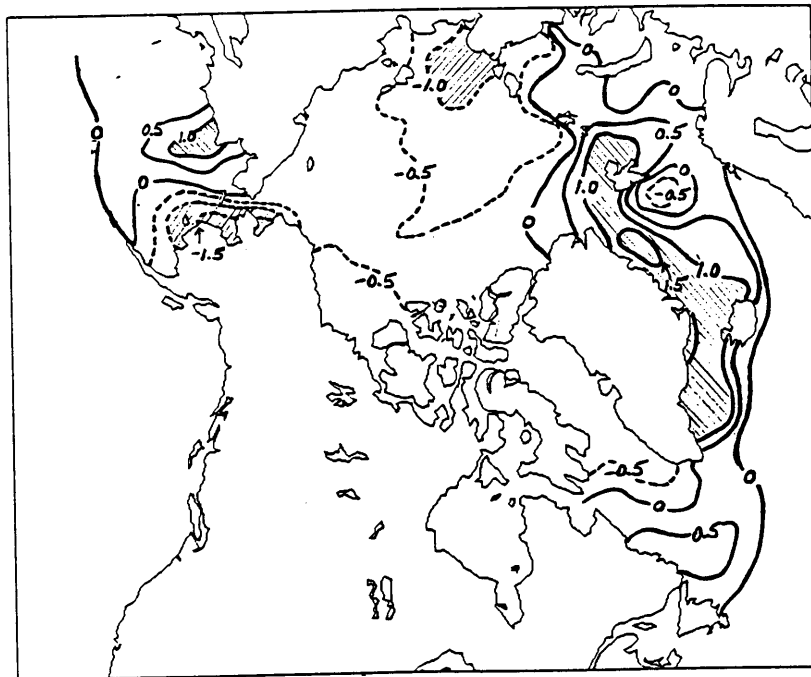
Fig. 2. 20-year simulation for (a) annual net ice growth (m) and (b) thickness changes associated with ice transport. Regions in which magnitudes of annual values exceed 1.0 meter are shaded. Positive values indicate net growth, negative values indicate net melt.

11

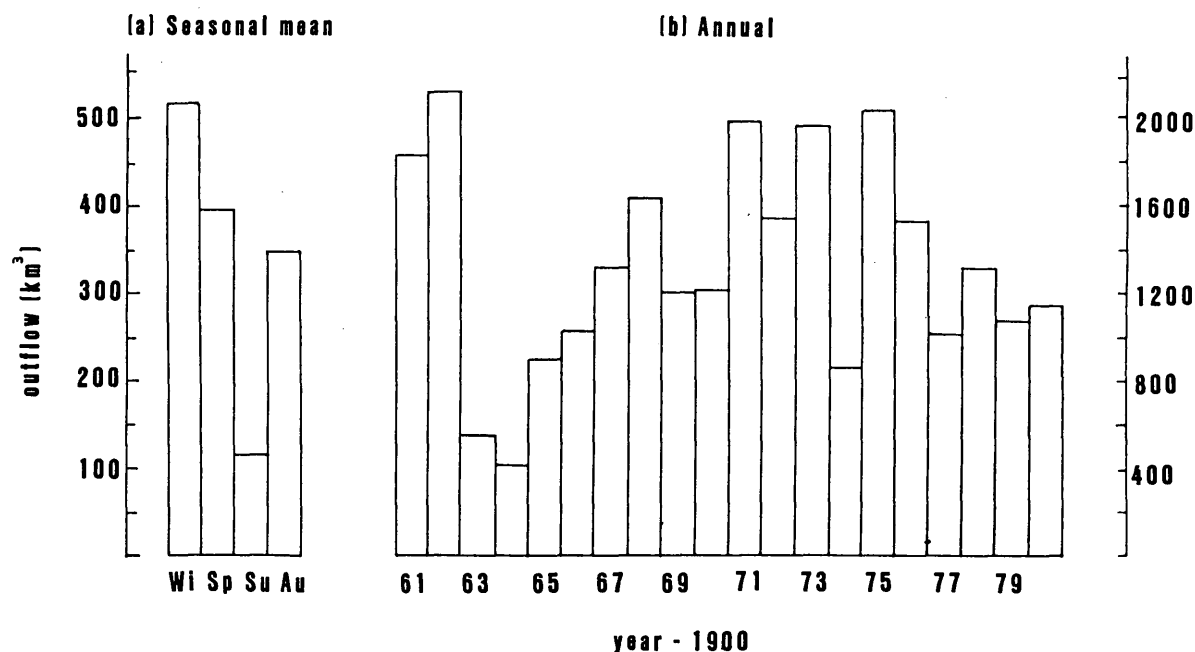Fig. 3. Outflow of ice (km³) from central Arctic into East Greenland Sea. (a) 20-year seasonal means, where Wi = winter, Sp = spring, Su = summer and Au = autumn. (b) Annual totals.

at point 2. A general increase in the ice thickness between 1964 and 1973 is especially apparent at point 2. The interannual fluctuations at the two points are quite consistent with each other and with the simulated outflow in Figure 3.

Also shown in Figure 4 are the relative contributions of ice melt and advection to the annual changes of ice thickness at the two points. These dynamic (advection) and thermodynamic (melt) contributions to the year-to-year changes tend to vary similarly. As shown in Table 1, the correlations between these two quantities are -0.62 at point 1 and -0.81 at point 2. Greater amounts of advection evidently lead to correspondingly greater amounts of melt in the same year. The correlations between the 12-month advective changes and the net melt during the *subsequent* 12 months are -0.52 and -0.80 at the same two points, suggesting that the thermodynamic effects of transport anomalies are not limited to the seasons in which the transport anomalies occur. Table 1 also provides evidence that thickness anomalies in the East Greenland region are determined primarily by fluctuations of ice transport rather than by thermodynamic factors. The April thicknesses at the two points correlate at 0.80 and 0.82 with the advective contribution to the antecedent 12-month change of thickness, while the corresponding correlations with the thermodynamic contributions are only -0.32 and -0.49. A more precise delinea-

Table 1. Correlations between April thickness (h_A) and advective (h_a) and thermodynamic (h_t) contributions to 12-month thickness change (Δ) at Points 1 and 2 (Figure 1).

Parameters*	Point no.	
	1	*2*
h_A vs $\Delta h_{a(-)}$	0.80	0.82
h_A vs $\Delta h_{t(-)}$	-0.32	-0.49
$\Delta h_{a(-)}$ vs $\Delta h_{t(-)}$	-0.62	-0.81
$\Delta h_{a(-)}$ vs $\Delta h_{t(+)}$	-0.52	-0.80
h_A vs h_{A-12} mo.	0.39	0.46

* - and + denote changes during antecedent and subsequent 12-month periods, respectively.

tion of the "source region" for the fluctuations of ice export appears to be in order. The relative dominance of the variable transport in effecting thickness changes also suggests that *regional* simulations of the ice/ocean system east of Greenland will require careful consideration of the inflow boundary conditions.

12
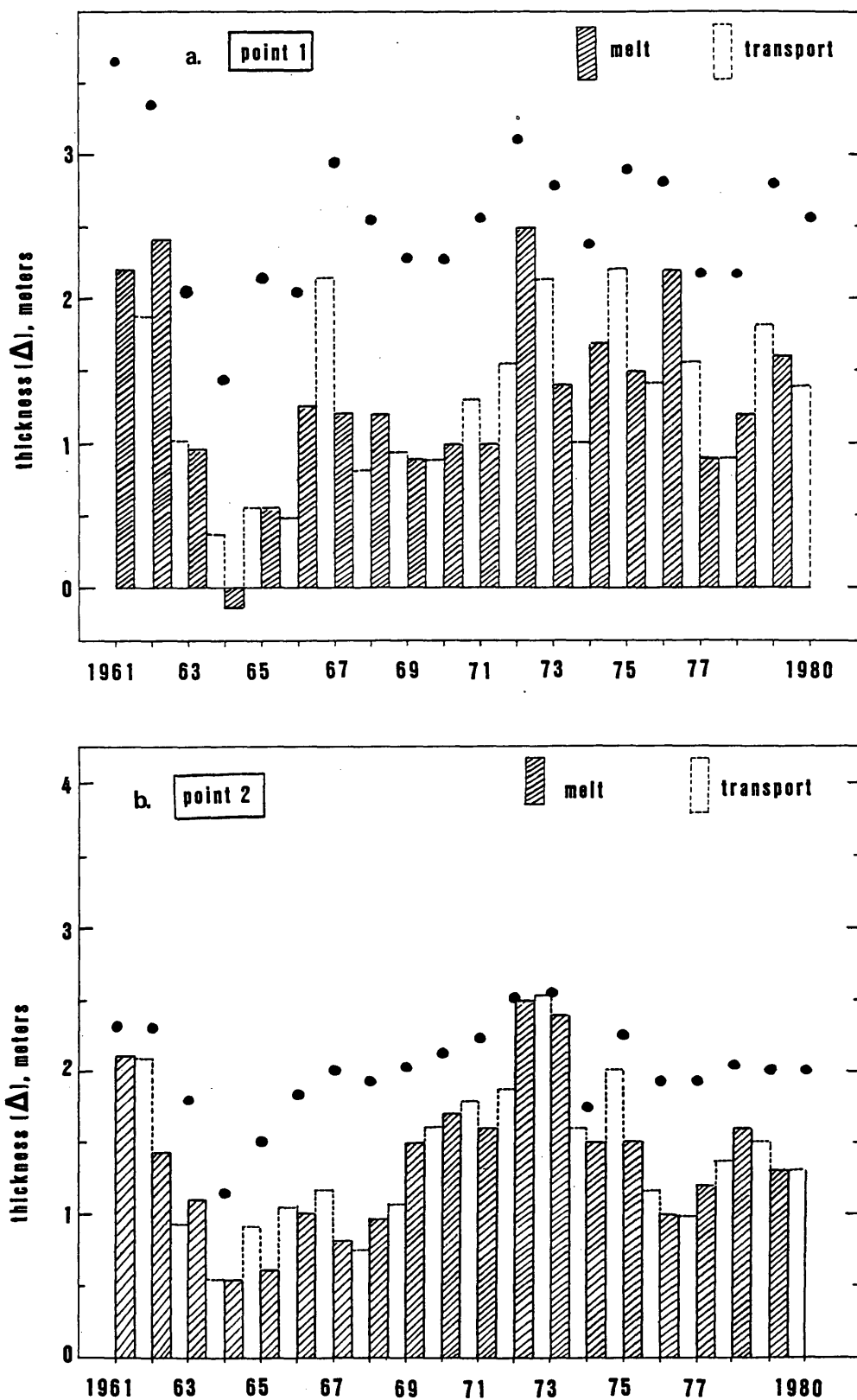
Fig. 4. April ice thickness (heavy dots). (a) Point 1. (b) Point 2. Changes (Δ) of ice thickness by melt and transport during intervening 12-month periods are represented by vertical bars. (Note that net annual melt is plotted as a positive quantity.)

13

REFERENCES

Crutcher, H.L., and J.M. Meserve, Selected level heights, temperatures and dew points for the Northern Hemisphere, *NAVAIR Report 50-1C-52*, revised, U.S. Naval Weather Service Command, Washington, D.C., 1970.

Hibler, W.D. III, A dynamic thermodynamic sea ice model, *J. Phys. Oceanogr., 9*, 815–846, 1975.

Hibler, W.D. III, Modeling a variable thickness sea ice cover, *Mon. Wea. Rev., 108*, 1943–1973, 1980.

Hibler, W.D. III, and K. Bryan, Ocean circulation: Its effects on seasonal sea-ice simulations, *Science, 224*, 489–492, 1984.

Johannessen, O.M., J.A. Johannessen, J. Morison, B.A. Farrelly, and E.A.S. Svendsen, Oceanographic conditions in the marginal ice zone north of Svalbard in early fall 1979 with an emphasis on mesoscale processes, *J. Geophys. Res., 88*, 2755–2769, 1983.

Parkinson, C.L., and W.M. Washington, A large-scale numerical model of sea ice, *J. Geophys. Res., 84*, 311–337, 1979.

Robock, A., The Russian surface temperature data set, *J. Appl. Meteor., 21*: 1781–1785, 1982.

Thorndike, A.S., D.A. Rothrock, G.A. Maykut, and R. Colony, The thickness distribution of sea ice, *J. Geophys. Res., 80*, 4501–4513, 1975.

Tucker, W.B. III, An application of a numerical sea ice model to the East Greenland area, USA Cold Regions Research and Engineering Laboratory, Hanover, N.H., CRREL Report 82-16, 1982.

Vinje, T.E., Sea ice conditions in the European sector of the marginal seas of the Arctic, 1966–1975, *Arbok Nor. Polarinst. 1975*, 163–174, 1977.

Wadhams, P., The ice cover in the Greenland and Norwegian seas, *Rev. Geophys. Space. Phys., 19*, 345–393, 1981.

On the Decay and Retreat of the Ice Cover in the Summer MIZ

G.A. MAYKUT

Department of Atmospheric Sciences/Geophysics, University of Washington
Seattle, Washington 98195

The position, movement, and decay of the ice cover in the summer MIZ depends not only on conditions in the atmospheric and oceanic boundary layers, but also on the state of the ice itself. Understanding the response of the ice to thermal and mechanical forcing is a necessary prerequisite to modeling the MIZ. The principal energy source driving the summer decay cycle is shortwave radiation, and the properties of the ice cover that affect its interaction with the ice and ocean are important variables in a detailed treatment of the summer MIZ. Variables and processes that are likely to be needed in modeling the summer ice cover include: ice concentration, lateral melting, floe size distribution, open water distribution, ice type and thickness, oceanic heat flux, and ice movement.

Modeling position of the MIZ

Seasonal ice covers some 2.5×10^7 km^2 of the polar oceans. Annual variations in the extent of this ice can produce large changes in the position of the MIZ. In the Southern Ocean, which loses some 80% of its ice cover each summer, poleward retreat of the MIZ varies between 500 and 1500 km. This means that between the time of maximum and minimum extent, movement of the MIZ *averages* up to 10 km/day. In the Arctic where roughly 50% of the ice is seasonal, ice retreat is much more variable, ranging from over 1500 km along 170°W (Bering-Chukchi Seas) to a nearly stationary ice edge in the area of the MIZEX field program (0°, 80°N).

For predicting the position of the winter MIZ, large-scale studies suggest that the ice model is of secondary importance to models of the atmosphere and ocean. This is not the case with the decay and retreat of the MIZ, which depend not only on conditions in the atmospheric and oceanic boundary layers, but also on the state of the ice itself. To calculate summer ice extent under varying climates requires a model that treats both the dynamics and the thermodynamics of the ice.

Models of greatly varying degrees of sophistication have been used to describe the location and movement of the MIZ. Pollard et al. (1983) combined a one-dimensional model of the upper ocean with a simple thermodynamic model of the ice. Despite neglecting ice movement, leads, penetration of solar radiation, and internal ice temperatures, the model gave reasonable ice extents and thicknesses along 170°W in the Arctic and along 160°E in the Southern Ocean. Good agreement with observations was also obtained by Parkinson and Washington (1979) using a thermodynamic ice model that included the effects of leads and ice movement in a highly parameterized form. The hope was that such models could be coupled with GCMs or climate models to carry out large-scale climate studies where the first order concern would be ice extent. However, simulations with a much more complete ice model (Hibler and Ackley, 1983) have shown that a realistic treatment of ice dynamics is crucial to accurate predictions of ice extent during the decay phase.

The problem with testing the simple models is that realistic thermal forcing contains implicit information on the extent and state of the present-day ice cover. Specified air temperatures, for example, reflect the presence or absence of ice. While this should not present a problem if the ice is coupled to an adequate atmospheric model, such a model does not allow proper treatment of the oceanic heat flux, even if it includes an ocean model. The difficulty is that the energy input to the bottom of the ice (F_w) originates from two sources: heat entrained from the deeper ocean and shortwave radiation entering the upper ocean through leads and thin ice. As I shall discuss later, it is the latter source that appears to dominate F_w in most regions. All the numerical simulations indicate that ice extent is sensitive to assumptions regarding the magnitude of F_w, particularly during the retreat phase. Models that do not take into ac-

count the solar component of F_w must choose an F_w only on the basis that it produces agreement with present conditions. Such an F_w contains assumptions regarding ice concentration, ice thickness, and incident shortwave radiation. There is no guarantee that this value would be appropriate to a different climatic regime where winds, currents, clouds, and deformational activity may be substantially altered.

A truly general ice extent model should contain enough detail to treat the interaction of shortwave radiation with the ice and upper ocean. Parkinson and Washington (1979) assumed that all the solar radiation absorbed in their leads went to warming in the leads or to lateral melting. With no solar heating below the ice, they had to assume an input of 25 W/m² from the deeper ocean in the Antarctic. Hibler and Ackley (1983), on the other hand, assumed that all the energy entering the leads went directly to F_w and took 2 W/m² as the contribution from the deeper ocean. Although our studies suggest that this is closer to the mark, substantial energy is absorbed in the first couple of meters of the water column where it is available for lateral rather than bottom melting. A more realistic distribution of the shortwave energy in the water would affect both the predicted ice concentrations and thicknesses. Applying some of the absorbed shortwave radiation to lateral melting in the Hibler and Ackley (1983) calculations would lower the amount of energy going to F_w, suggesting that a larger heat contribution from the lower ocean would be needed to match observed changes in ice extent. This is not necessarily the case, however, because a lower ice concentration would increase solar heating beneath the ice. The overall effects of including lateral melting and an improved treatment of shortwave radiation in the model are difficult to assess because they are influenced by the ice dynamics. Numerical experiments are needed to address the problem more completely.

Important factors affecting the position and behavior of the summer MIZ are thus: ice advection, deformation, thickness, concentration, lateral melting, and solar heating beneath the ice. Dynamic processes in the ice are also important during the winter, not so much because of their effect on ice extent, but because they affect regional rates of ice production and, hence, turbulent heat input to the atmosphere and mixed-layer development in the ocean. Inclusion of these factors in large-scale models appears necessary if interactions between the ice, atmosphere, and ocean are to be adequately simulated.

Modeling summer decay

Melting alters not only the properties of the ice cover, but also the structure of the upper ocean. Horizontal gradients in melt-water input and the proximity of warmer and more saline water can give rise to a variety of mesoscale phenomena in the ocean (eddies, jets, upwelling), which impact biological activity and acoustical properties across the MIZ. Floe breakup and increasing stratification beneath the ice affects the response of the ice to winds and currents and the rate at which heat is transferred from the water to the ice. To understand and model this system will require a much more detailed consideration of ice-ocean-atmosphere interactions than appears in present large-scale treatments. In the following sections I will examine some of the variables and processes that are likely to be needed in modeling the summer ice cover.

Both the atmosphere and the ocean supply the energy needed to drive the melt. The primary source of energy from the atmosphere is incoming shortwave radiation, with turbulent heat input tending to balance longwave radiation losses at the surface. Although warm air advected over the ice in coastal regions and near the ice/ocean boundary can result in a net addition of heat to the ice, the shortwave radiation and the properties of the ice cover that affect its absorption can be considered as the principal variables. Heat transfer from the water to the ice occurs at both the edges and the bottoms of floes. As discussed earlier, this heat is derived from the deeper ocean and from solar energy absorbed in the upper ocean. The rate at which this heat is lost to the ice is complicated by lateral advection of ice or water across the ice edge, mixed-layer stratification, waves, floe breakup, and mesoscale circulations associated with the MIZ.

Few observational data are yet available from the summer MIZ, and we are unable to answer many basic questions regarding the heat and mass balance of the ice cover. For example, what fraction of the mass loss in the MIZ occurs at the extreme ice edge? What is the relative importance of atmosphere and ocean in the decay cycle? How is solar energy absorbed in the water partitioned between lateral melting, bottom melting, temporary storage in the ocean, and loss to the atmosphere? MIZEX 84 should provide basic data needed to address these questions. Factors that are likely to be important include:

Ice concentration. Because the albedo of leads is low (0.08–0.1) compared to that of melting ice

16

(0.4–0.7), changes in ice concentration (A_i) can produce large changes in the amount of shortwave radiation absorbed in the MIZ. There is, in addition, a positive feedback between energy absorbed in the leads and A_i due to lateral melting on floe edges. Previous studies have focused largely on the positive feedback aspects of the problem, neglecting much of the physics involved. Zubov (1943), for example, assumed that all the energy entering the leads was lost through lateral melting and derived a simple expression for the increase in the amount of open water (A_w) with time,

$$A_w = A_{wo} e^{at} \qquad (1)$$

where $a \equiv (1 - \alpha_w) F_r / \varrho_i L h$ and A_{wo} is the amount of open water at time $t = 0$; α_w is the lead albedo, F_r is the flux of incoming shortwave radiation, ϱ_i is the ice density, L is the latent heat of fusion of water, and h is the ice thickness, which was assumed to be constant. The exponential increase in $A_w(t)$ results in the complete decay of a 1-m-thick ice cover in 6–7 weeks. Langleben (1972) found that (1) was too slow to explain the disappearance of ice in sheltered bays and fjords in the Canadian archipelago. Modifying the equation to include melting at the surface of the ice, he obtained

$$A_w = A_{wo}\left[1 - \frac{(1 - \alpha_i)F_r t}{\varrho_i L h_o}\right]^{-\gamma} \qquad (2)$$

where α_i is the ice albedo, h_o is the initial ice thickness, and $\gamma = (1 - \alpha_w)/(1 - \alpha_i)$. Equation (2) yielded decay times of 3–4 weeks, in agreement with observations. A serious problem with the above formulations is that they allow no energy input beneath the ice and, as a result, must overestimate the amount of lateral melting. Even more serious for modeling the MIZ is the lack of ice dynamics. Changes in wind direction can produce large and rapid changes in A_i that are unrelated to the thermodynamics, but that can have a significant impact on the heat and mass balance.

Lateral melting/erosion. An important step in developing a more realistic model of ice decay is to improve the treatment of melting on flow edges. Serious weaknesses in previous treatments were in determining (a) the amount of solar energy utilized for lateral melting and (b) the rate at which this energy was transferred to floe edges. At the University of Washington, Don Perovich and I have examined several different approaches to the problem. The simplest approach is to assume that
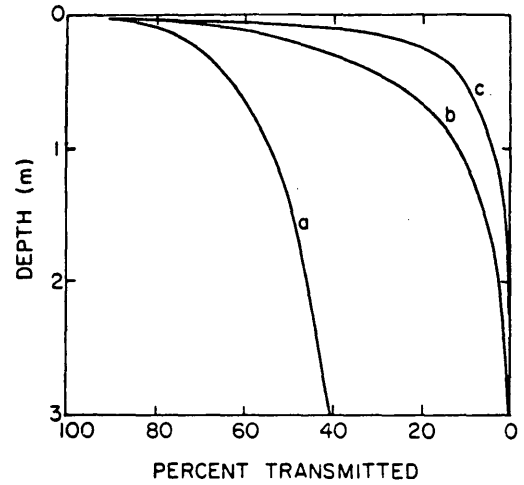

Fig. 1. Percent of incoming shortwave radiation transmitted by a) leads, b) blue ice, and c) white ice. Curves were calculated using the radiative transfer model of Grenfell (1979) and optical data from Grenfell and Maykut (1977).

leads are well mixed and can be characterized by a single temperature T_w. To estimate (a), we assumed that relative motion between ice and water would prevent shortwave energy absorbed beneath the ice from contributing to lateral melting—energy absorbed between the surface of the lead and the bottom of the ice is thus available for lateral melting and heating of the lead. Figure 1 shows that for 1-m ice 45% of F_r remains in the lead, while for 3-m ice this figure increases to 60%. To estimate (b), we initially used a parameterization based on laboratory measurements of melting on vertical ice walls (Josberger and Martin, 1981),

$$\bar{f} = 2.46(T_w - T_f)^{1.36} = \frac{1}{2}(dW/dt) \qquad (3)$$

where $\bar{f}$ is the vertically averaged rate of lateral melting, T_f is the freezing point temperature of the water, and W is the lead width. The heat balance equation for the lead can be written

$$W[(1 - \alpha_w)F_r - I_w(h) + F_L - \epsilon_w \sigma T_w^4 + F_{sw} + F_{\varrho w}] - \varrho_i L\, h(dW/dt) = \varrho_w c_w h W(\partial T_w/\partial T) \qquad (4)$$

where $I_w(h)$ is the shortwave radiation absorbed beneath the ice, F_L is the incoming longwave radiation, ϵ_w is the longwave emissivity of the water, F_{sw} is the sensible heat flux, $F_{\varrho w}$ is the latent heat flux, ϱ_w is the density of the water, and c_w is the specific heat of the water. Analogous heat balance equations can also be written for the upper and

17

Fig. 2. Schematic illustration of the simple lead/ice model.

lower boundaries of the surrounding floes (see Figure 2).

Equations (3) and (4) can be solved to obtain predictions on how changes in W, h, and the thermal forcing affect lateral melting. The model predicts that dW/dt becomes increasingly insensitive to W and other environmental parameters as lead width increases. The reason is that an increasing W produces warming in the lead and greater heat losses to the atmosphere. Figure 3 shows dW/dt as a function of W for conditions representative of the MIZ. While the results conform to

intuition, we suspect that (3) may underestimate the rate of heat transfer to lead walls under actual field conditions. Using idealized lead geometries, we carried out several combined lead/ice simulations. With (3), the calculations indicated that a 1.5-m ice cover would vanish by thinning rather than by lateral ablation. If, on the other hand, we assumed that $T_w = T_f$ (i.e. all the excess heat in the lead was used for lateral melting), the ice thinned substantially, but A_i approached zero faster than h. Clearly what is assumed about heat transport in the leads can make a large difference in the pattern
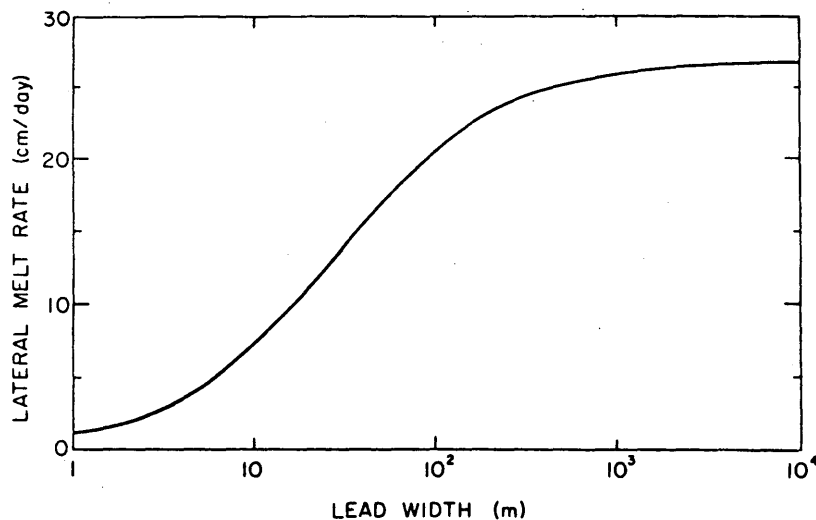

LEAD WIDTH (m)

Fig. 3. Lateral melt rates as a function of lead width, as predicted by the lead/ice model for midsummer conditions similar to those in the MIZ (after Perovich, 1983).
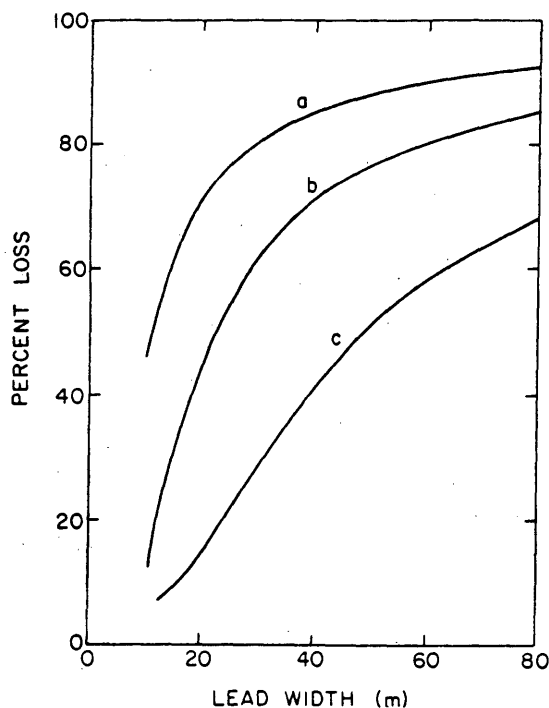
18

Fig. 4. Percent of energy deposited in the upper lead that is lost to the underlying water for horizontal diffusivities of a) 1, b) 5, and c) 30 cm^2/s (after Perovich, 1983).

of ice decay. The most serious problem with (3) is that it produced T_w values of up to $+5\,°C$. Such temperatures seem unrealistically high and suggest that there is either more rapid heat transfer to the ice or that some of the energy absorbed in the upper lead is transported below the ice—or a combination of both.

Field data from the MIZ are presently inadequate to answer questions about lateral melting there. However, Perovich (1983) has recently carried out measurements in a small (10 m) lead in static ice adjacent to Prince Patrick Island that bear on the problem. He found that, with lead salinities in the 5-10%₀₀ range, roughly 50% of the energy absorbed in the upper lead did not contribute to lateral melting. Observed rates of lateral melting were about 5 times those predicted by (3). By replacing the well mixed assumption in the lead with a two-dimensional diffusion model, it was possible to obtain good agreement between observed and predicted values of melt rate, heat content, and heat loss to the underlying ocean. Numerical experiments with this model indicate that the fraction of heat transported downward from the lead (B) increases with increasing W (Figure 4). In areas such as the MIZ where the ice is much more active, we expect that horizontal heat

transport in the leads will be much larger than in static ice. Figure 4 shows that B should decrease as the horizontal diffusivity (x_x) increases. Predicted values of B can be approximated by the expression

$$B(W,h) = a + b(\ln W/h) \tag{5}$$

where a and b are constants that depend on the diffusivity. While the two-dimensional treatment would be awkward to use in a MIZ model, it is possible to reproduce the predicted rates of lateral melting using a modified version of the simple model (Figure 2). This involves adding a parameterization of B [eq (5)] and replacing (3) with an expression that depends not only on T_w, but also on air temperature and F_r.

There are many processes at work in the MIZ carrying heat to the ice (and vice versa). Among those affecting lateral ablation are waves, edge erosion from floe bumping, mechanical mixing, and ice deformation. Whether these processes can be successfully parameterized by suitable choices of x_x and x_z is not clear. MIZEX 84 should help to answer this question.

Floe size distribution. As the ice cover becomes increasingly broken up, the probability decreases that heat absorbed by the leads will be lost to the atmosphere or underyling ocean, and heat transfer to floe edges becomes increasingly efficient. Ice concentration alone is thus inadequate to characterize the state of the ice cover in areas like the MIZ. Experiments with the simple lead/ice models demonstrate that, for a given ice concentration, the rate of lateral decay depends directly on the number of leads, i.e. on the total floe perimeter. Floe perimeter in a particular region can be determined if the floe size distribution (N) is known. N appears to be of fundamental importance in modeling the MIZ, affecting not only the lateral melting but also average drag coefficients, melt pond coverage, and the distribution of open water. Floe size distributions have been measured in several locations (e.g. Wadhams, 1973; Vinje, 1977; Rothrock and Thorndike, in press), but a general theory is not yet available. The equation governing N is analogous to that for the ice thickness distribution, containing terms describing advection, thermodynamics (lateral melting), and mechanical processes (breaking). The difficulty in developing a model for N is in formulating the dynamic and thermodynamic terms. Some of the thermodynamic problems have been mentioned above. Floe breaking in the outer MIZ appears to be controlled largely by wave action (Wadhams, in press), but the factors affecting interior breaking

are less certain. Perovich (1983) has examined the effect of random breaking on N. Although it was possible to find breaking functions that would approximate observed N's, the approach did not consider the underlying of physics and would be difficult to generalize. Additional work is needed to understand and quantify the processes involved in floe breakup away from the ice edge.

Ice type. Usually neglected in discussions of the heat and mass balance of the MIZ are variations in the optical properties of the ice, which can have a significant effect on the input of shortwave radiation. Grenfell and Maykut (1977) report that there are basically two types of melting first-year ice: (a) "blue" ice, where the surface is saturated with melt water, and (b) "white" ice, where the surface layer is well drained. The shallow melt ponds typical of first-year ice can be considered blue ice. Blue ice absorbs about twice as much energy as white ice and can transmit a substantial portion of this to the underlying ocean. Table 1 compares how 1-m-thick layers of blue ice and white ice distribute F_r for different ice concentrations. When A_i is high, transmission through blue ice accounts for most of the energy absorbed beneath the ice. As A_i decreases, leads quickly begin to dominate solar input to the water. Of particular interest is the fairly weak relation between regional shortwave absorption and ice concentration when the ice is blue—decreasing A_i from 90% to 50% produces only a 10% change in heat input. Areas with substantial amounts of blue ice are thus much less sensitive to changes in A_i than areas of white ice.

Thin floes whose upper surfaces are flat tend to be blue, while on those with more irregular surfaces, only ponded areas are blue. Multi-year ice generally falls into the latter category. During MIZEX 83 up to 10% of the floes in some areas comprised a third ice type, "dirty" ice. Such ice was formed in very shallow seas where substantial amounts of sediment were incorporated into the ice during growth. Such floes tended to be bare early in the melt season, even when a thick snow cover was present on surrounding floes. Although measurements were not made, the albedos of dirt-covered ice probably fall between those of leads and blue ice. Unlike leads and blue ice, however, essentially all of the radiation absorbed by the dirt layer goes directly to surface melting, with little, if any, transmitted to the water.

The relative proportions of different ice types in the various MIZ areas is unknown, but will depend on time and location. In the Bering–Chukchi Seas, where surface melting is vigorous, blue ice is likely to be a major component of the summer MIZ. In regions like the Southern Ocean, where surface melting is minimal, blue ice is probably unimportant, except possibly near the extreme ice edge. MIZEX 83 observations were carried out early in the melt season when much of the ice was still snow-covered and ice type was largely a function of thickness—1-m floes tended to be ponded and blue, and thicker floes were generally white. Further melting should produce a strong decrease in the amount of blue ice, making it likely that blue ice will make up a significant fraction of the MIZEX area during late July and August.

Oceanic heat flux. Bottom ablation and the resultant thinning of the ice plays an important part in the decay of the MIZ, influencing light transmission, floe breakup, and the buoyancy flux. A basic concern is the source of the energy producing this melt. If the oceanic flux is largely derived from shortwave radiation absorbed in the upper ocean, then an ice model that treats the fac-

Table 1. Absorption and transmission of incoming shortwave radiation by a 1-m-thick ice cover. Values are expressed as percentages of F_r, weighted by relative area.

Ice concentration	Surface type	Surface input (%)	% absorbed ($z < 1$ m)	% transmitted below 1 m	Regional sw input (%)
0.9	blue ice	61	48	13	70
	white ice	27	25	2	36
	leads	9	4	5	
0.5	blue ice	34	27	7	80
	white ice	15	14	1	61
	leads	46	19	27	

tors discussed above is crucial in modeling the behavior of the MIZ. If, on the other hand, the deeper ocean supplies most of the heat to F_w, a somewhat cruder ice model may be adequate. Available evidence points to solar energy as the principal component of F_w. Simulations in the north have generally used the Central Arctic value of 2 W/m^2, but calculations by Maykut (1982) indicate that this heat is due almost completely to F_r. The same conclusion should hold in the peripheral seas surrounding the basin, except possibly where Atlantic water is involved. To get an idea of F_w in the Greenland Sea, I have utilized buoy data supplied by J. Morison (Polar Science Center, University of Washington) to infer the heat and mass balance of the ice cover in the vicinity of the buoy during its four-and-a-half-month drift. Solar input beneath the ice was calculated from daily values of A_i interpolated from weekly ice charts; heat input from the deeper ocean was assumed to be zero. Average surface winds were estimated from daily pressure maps. Surface ablation totaled some 1.5 m by the time the buoy reached the ice edge, indicating that more than half the ice melt had to be the result of heat supplied from the ocean. If all the energy absorbed between the surface of the leads and the bottom of the ice was used for lateral melting, the calculations predict an ice thickness of about 50 cm at the end of the drift; if only half this energy went to lateral melting, the predicted thickness would be close to zero. Even though uncertainties in the lateral melting and the initial thickness distribution of the ice make it difficult to pin down the heat contribution from below the mixed layer, it appears to have been small. In the Antarctic the role of the deeper ocean may be somewhat more important. The small amount of surface melting (Andreas and Ackley, 1982) means that most of the mass loss there must occur at the ice/water interface. Gordon (1981) estimates that up to 50% of F_w could be derived from water below the pycnocline, but the uncertainty in this estimate appears to be large. Given the magnitude of F_r during the summer and the rate at which it can add heat to the ocean, it seems best to proceed on the assumption that it dominates F_w.

Discussion

Although most of the previous discussion has centered on thermodynamic problems, it should be reiterated that the dynamics and thermodynamics are intimately connected. Dynamic factors such as floe breakup, band formation, ice advection, and deformation clearly affect the thermal response of the ice cover. Perhaps more troublesome to treat are changes in lateral erosion and heat transport in the leads that are introduced by ice movement. What happens to heat contained in the water as floes move relative to one another? Does the heat tend to move laterally in the stable surface layer, or to mix downward? What is an appropriate way to treat the complex geometry of open water areas in the MIZ? We really don't know the answers to these questions yet. Likewise, it is unclear to what extent our approach to the thermodynamic part of the summer decay problem will provide a framework for including dynamic effects. The primary thrust of our efforts during MIZEX 84 will be to quantify interactions between shortwave radiation, the upper ocean, and the moving ice cover in an effort to answer such questions.

REFERENCES

Andreas, E.L., and S.F. Ackley, On the differences in ablation seasons of arctic and antarctic sea ice, *Mon. Weather Rev., 39,* 440-447, 1982.

Gordon, A.L., Seasonality of Southern Ocean sea ice, *J. Geophys. Res., 86,* 4193-4197, 1981.

Grenfell, T.C., and G.A. Maykut, The optical properties of ice and snow in the Arctic Basin, *J. Glaciol., 18,* 445-463, 1977.

Hibler, W.D., III, and S.F. Ackley, Numerical simulation of the Weddell Sea pack ice, *J. Geophys. Res., 88,* 2873-2887, 1983.

Josberger, E.G., and S. Martin, A laboratory and theoretical study of the boundary layer adjacent to a vertical melting ice wall in salt water, *J. Fluid Mech., 111,* 439-473, 1981.

Langleben, M.P., The decay of an annual cover of sea ice, *J. Glaciol., 11,* 337-344, 1972.

Maykut, G.A., Large scale heat exchange and ice production in the Central Arctic, *J. Geophys. Res., 87,* 7971-7984, 1982.

Parkinson, C.L., and W.M. Washington, A large-scale numerical model of sea ice, *J. Geophys. Res., 84,* 311-337, 1979.

Perovich, D.K., On the summer decay of a sea ice cover, Ph.D. thesis, Geophysics Program, Univ. Washington, Seattle, 1983.

Pollard, D., M.L. Batteen, and Y.J. Han, Development of a simple upper ocean and sea ice model, *J. Phys. Ocean., 13,* 754-768, 1983.

Rothrock, D.A., and A.S. Thorndike, Floe size distribution of arctic sea ice, *J. Geophys. Res.,* in press.

Vinje, T.E., Sea ice studies in the Spitz-

bergen-Greenland Sea area, Landsat Report E77-10206, U.S. Dept. Commerce, 1977.

Wadhams, P., The effect of a sea ice cover on ocean surface waves, Ph.D. thesis, Univ. Cambridge, Cambridge, England, 1973.

Wadhams, P., The seasonal ice zone, in *Geophysics of Sea Ice,* edited by N. Untersteiner, NATO Advanced Study Institute, Chapter 15, in press.

Zubov, N.N., *Arctic Ice (L'dy Arktiki),* Izdatel' stvo Glavsevmorputi, 360 pp., Moscow, 1943. (Translated for AFCRC by the U.S. Naval Oceanographic Office and American Meteorological Society).

On The Role of Ice Interaction in Marginal Ice Zone Dynamics

M. LEPPÄRANTA* AND W.D. HIBLER III

*U.S. Army Cold Regions Research and Engineering Laboratory
Hanover, New Hampshire 03755*

On leave from the Institute of Marine Research, Helsinki, Finland

Under appropriate conditions, the nonlinear plastic nature of ice interaction together with the nonlinear coupling between ice thickness characteristics and ice rheology can substantially modify the character of marginal ice zone (MIZ) dynamics. The purpose of this paper is to examine the ramifications of these nonlinearities using Hibler's (1979) model. Among other things, the results of this investigation show that if the ice thickness distribution is allowed to equilibrate in response to a given wind field, then the shape of the compactness profile will be dictated by the thickness strength coupling. The results also indicate that rheology-induced ice-edge jet effects will not be present for an ideal plastic rheology, but can exist in Hibler's viscous plastic model with a sufficiently "weak" viscosity. It is worth noting that these results are in contrast to recent studies by Røed and O'Brien (1981) where the ice rheology has been approximated by a hydrostatic pressure term only rather than by a full plastic ice interaction model.

To examine how a plastic ice rheology modifies MIZ dynamics we have carried out a series of idealized small-scale simulations using the dynamic part of Hibler's (1979) two-level model. In addition, analytic solutions for the equilibrium plastic adjustment case are constructed. The configuration (Fig. 1) consists of an idealized north–south ice edge; spatial variations in the direction of the ice edge are ignored.

A complete description of the results will be given in a subsequent paper. Here we will discuss some of the main features of the results.

The model consists of momentum balance, mass conservation, two-level ice thickness distribution, and viscous plastic rheology (Hibler, 1979). We use it to study the response of the MIZ to winds on short time scales; geostrophic ocean currents and thermodynamic effects are ignored. We also ignore the inertia of ice, which is small on time scales of more than an hour or two. It is considered that spatial variations in the MIZ are much larger perpendicular to the ice edge than parallel to it and, hence, derivatives with respect to y (Fig. 1) are assumed to be zero.

The Hibler model is now reduced to

$$\frac{\partial}{\partial x}(\sigma_{xx}, \sigma_{xy}) - \varrho_i hf\mathbf{k}x\bar{u} + \bar{\tau}_w + \bar{\tau}_a = 0, \qquad (1)$$

$$\frac{\partial h}{\partial t} = -\frac{\partial}{\partial x}(uh), \qquad (2)$$

$$\frac{\partial A}{\partial t} = -\frac{\partial}{\partial x}(uA), \qquad (3)$$

where σ = ice stress tensor
ϱ_i = ice density
h = thickness
f = Coriolis parameter
$\mathbf{k}$ = unit vector vertically upward
$\bar{u} = (u, v)$ = ice velocity
$\bar{\tau}_a$ and $\bar{\tau}_w$ = air and water stresses
A = ice compactness
t = time.

The air and water stresses are given by

$$\bar{\tau}_a = \varrho_a C_a |\bar{U}_a|(\cos\phi + \sin\phi\,\mathbf{k}x)\bar{U}_a, \qquad (4a)$$

$$\bar{\tau}_w = \varrho_w C_w |\bar{u}|(\cos\theta + \sin\theta\,\mathbf{k}x)\bar{u}, \qquad (4b)$$

where U_a is the geostrophic wind, ϱ_a and ϱ_w are the air and water densities, C_a and C_w are the air and water drag coefficients, and ϕ and θ are the boundary layer turning angles for air and water.
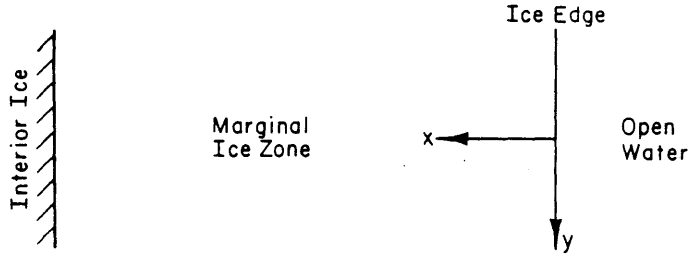
Fig. 1. The model MIZ and the coordinate system.

The viscous plastic rheology of the Hibler model gives linear viscous creep for small strain rates and plastic flow otherwise. While other shapes could be employed, the yield curve used here is an ellipse in the principal stress space and the plastic flow is determined according to the associated flow rule. The rheology is defined by

$$\sigma = 2\eta\dot{\epsilon} + [(\xi-\eta)\dot{\epsilon}_I - \tfrac{1}{2}P]I \qquad (5)$$

$$\dot{\epsilon} = \tfrac{1}{2}[\nabla\bar{u} + (\nabla\bar{u})^T] \qquad (6)$$

$$P = P^*h\exp[-C(1-A)] \qquad (7)$$

$$\xi = \tfrac{1}{2}P/\max[(\dot{\epsilon}_I^2 + \dot{\epsilon}_{II}^2 e^{-2})^{1/2}, \dot{\epsilon}_0], \quad \eta = \xi e^{-2}. \qquad (8)$$

Here η and ξ are the shear and bulk viscosities, P is the hydrostatic pressure term, $\dot{\epsilon}$ is the strain rate tensor, $\dot{\epsilon}_I$ and $\dot{\epsilon}_{II}$ are the strain rate invariants equal to the sum and difference of the principal strain rates, and I is the unit tensor. P^*, C, $\dot{\epsilon}_0$ and e are rheological parameters: P^* is the strength constant, C is the reduction constant for opening, $\dot{\epsilon}_0$ is the maximum viscous creep rate, and e is the ratio of compressive to shear strength. Without y-derivatives the strain rate tensor is reduced to

$$\dot{\epsilon} = \begin{pmatrix} \partial u/\partial x & \tfrac{1}{2}(\partial v/\partial x) \\ \tfrac{1}{2}(\partial v/\partial x) & 0 \end{pmatrix} \qquad (9)$$

and its invariants to $\dot{\epsilon}_I = \partial u/\partial x$, $\dot{\epsilon}_{II} = |\partial \bar{u}/\partial x|$. As a result, the stress state can lie only in a restricted region within or on the yield curve (Fig. 2). The momentum equation can now be written as

$$\frac{\partial}{\partial x}\left[(\xi+\eta)\frac{\partial u}{\partial x} - \frac{P}{2}\right] + \varrho_i hfv + \tau_{wx} + \tau_{ax} = 0, \qquad (10a)$$
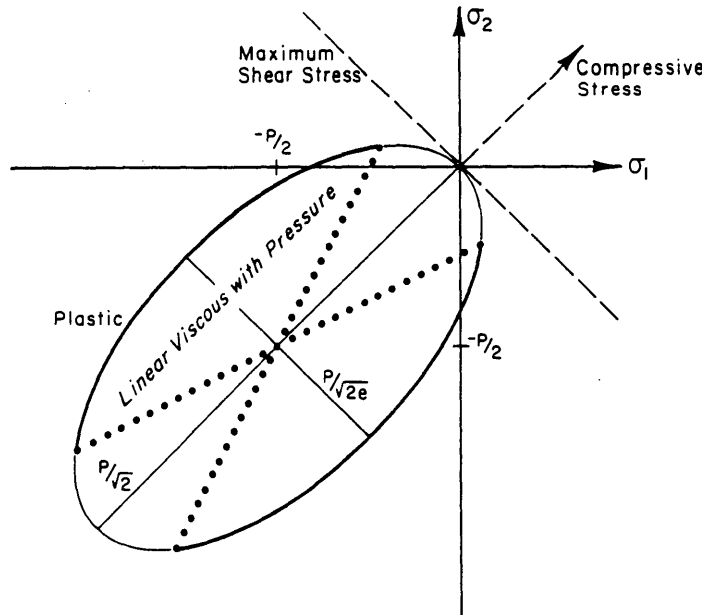

Fig. 2. The yield ellipse. Thick lines indicate the possible stress states in the MIZ model.

24

Table 1. The standard model parameters.

$\varrho_a = 1.3$ kg m^{-3}	$C_a = 1.2 \times 10^{-3}$	$\{\phi = 25°$
$\varrho_w = 10^3$ kg m^{-3}	$C_w = 5.5 \times 10^{-3}$	$\{\phi = 25°$
$\varrho_i = 910$ kg m^{-3}	$\{f = 1.46 \times 10^{-4}$ s^{-1}	$P^* = 10^4$ Nm^{-2}
$C = 20$	$\{e = 2$	$\{\dot{\varepsilon}_0 = 2 \times 10^{-7}$ s^{-1}

$$\frac{\partial}{\partial x}\left(\eta \frac{\partial v}{\partial x}\right) \qquad -\varrho_i h f u + \tau_{wy} + \tau_{ay} = 0. \quad (10b)$$

The standard parameters for the present calculations are shown in Table 1. Except for P^* and $\dot{\varepsilon}_0$ they are the same as in the original model. The former has been the main tuning parameter of the model and has ranged from 5×10^3 in the original model to 2.75×10^4 Nm^{-2} in a recent work of Hibler and Walsh (1982). Our creep limit $\dot{\varepsilon}_0$ is one to two orders of magnitude larger than usually applied.

The numerical scheme and the computer code of the original model (Hibler, 1979, 1980) have been employed. The grid size is 4 km and the time step is half an hour. Initially, the MIZ is 60 km wide, and the ice cover is compact and 1.5 m thick. This thickness corresponds to a characteristic MIZ value given in Wadhams et al. (1979). At time zero a constant wind starts to blow. Its speed is always 10 m/s, and in different runs its direction varies around the whole circle at 30° spacing. In the following discussion, the direction, noted by ψ_a, is defined as the wind vector direction and is reckoned counterclockwise from the x-axis. The interior ice is assumed to be motionless.

The free-drift case is a useful reference solution for considering the importance of ice interaction in ice drift. For a 1.5-m ice thickness, the free-drift speed is 15.9 cm/s and the direction is 10.6° to the right from the direction of geostrophic wind. As the thickness decreases to zero, free drift becomes aligned with the wind and its speed increases to 16.8 cm/s.

Initialization of the MIZ flow

The initial velocity distribution was calculated by solving the momentum equation only. Ice thickness and compactness were therefore equal to their initial values, 1.5 m and 1.0, over the whole MIZ. The results show a plastic slip at the left-hand boundary and a nearly constant ice velocity in the MIZ (Figs. 3 and 4). In this nearly constant flow the ice creeps in a linear viscous manner and

the creep limit restricts velocity differences between neighboring grid cells to less than 0.8 mm/s. As an exception, in the case of $\psi_a = 330°$, the yield strength is not overcome and the plastic slip is missing.

The results indicate that the free-drift solution is a very good approximation if it is directed more than about 45° away from the MIZ. On the other hand, strictly on-ice forcing gives practically no motion at all. Between these two extremes there are wide regions of nearly edge-parallel flows. Comparing with free-drift, it is seen that the ice interaction has a rectifying effect on these flows. This is an important feature and it is not difficult to distinguish from observations. The reason for this rectification is that ice has compressive strength. There is a slight asymmetry between northward and southward flow patterns due to the Coriolis and oceanic turning angle effects.

The basic dimensionless parameter in our problem is

$$\gamma^* = \frac{\tau_a L}{P^* h} \qquad (11)$$

where L is the width of the MIZ. First, plastic deformation is possible only for $\gamma^* \geq \gamma$, where γ depends on the mode of deformation at the left-hand boundary and on the yield ellipse elongation e. Second, in plastic flow the effect of ice interaction can be thought of as reducing the wind stress by the factor of $1-\gamma/\gamma^*$. The values of γ for some specific cases are:

	General	Standard ($e = 2$)
Uniaxial extension	$\frac{1}{2}(\sqrt{1+e^{-2}}-1)$	0.06
Pure shear	$\frac{1}{2}e^{-1}$	0.25
Uniaxial contraction	$\frac{1}{2}(\sqrt{1+e^{-2}}+1)$	1.06

The present work has $\gamma^* \approx 0.62$, and we can see from Figure 3 that the $1-\gamma/\gamma^*$ dependence describes the solution qualitatively well.

Adjustment between mass and velocity

As the MIZ flow evolves with time, the motion toward the interior ice must come to a stop. Consequently, the MIZ gets separated from the interior ice, or a strictly edge-parallel flow develops (Fig. 5). The critical factor seems to be whether the free-drift solution is inward or outward.

When the MIZ separates from the interior ice, its motion is approximately that of the free-drift
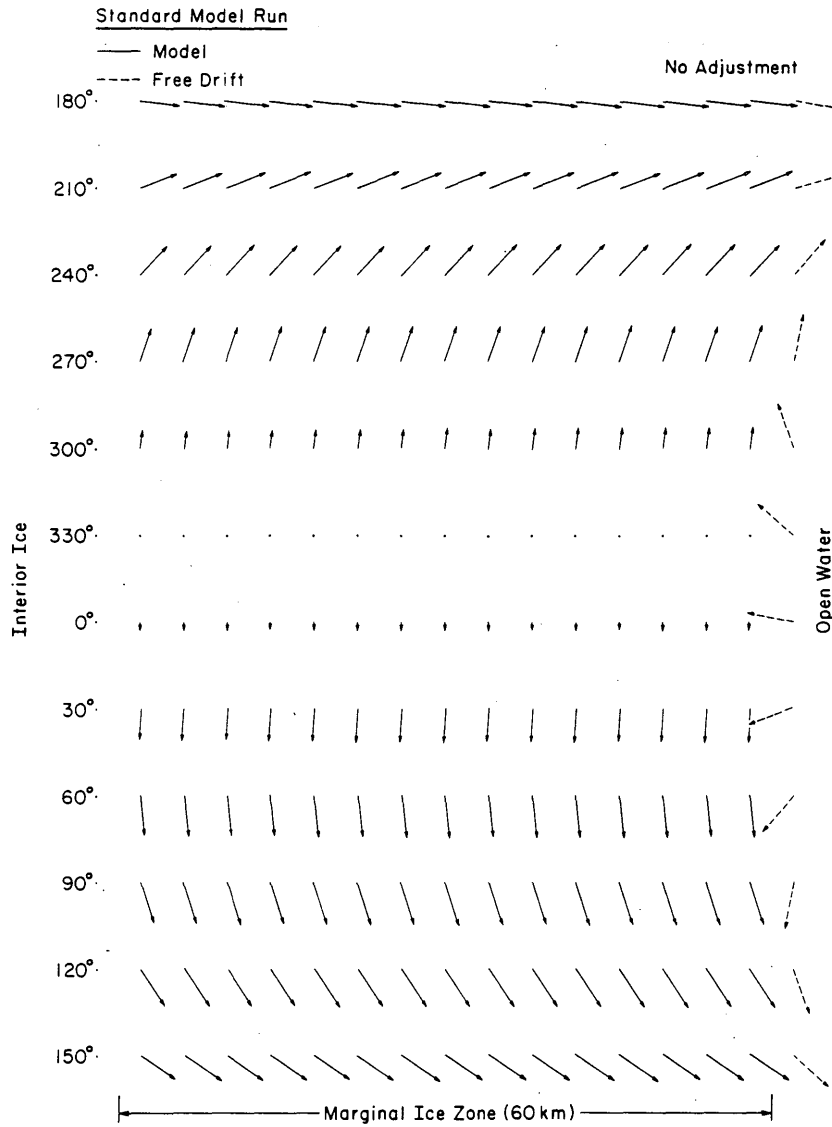
25

Fig. 3. The initial MIZ flow. The degree-numbers on the right give the direction of the geostrophic wind.

state. The velocity is not exactly a constant, as it is slightly modified by the Coriolis effect and the hydrostatic pressure term. The variations are less than 2 cm/s, which is about one-tenth of the average speed.

Mutual adjustment between the ice mass distribution and the velocity keep the motion parallel to the edge. On-ice forcing becomes balanced with the pressure gradient within the MIZ. After 48 hr of model simulation, edge-parallel flows are already well developed and have approximate gradient within the MIZ. After 48 hrs of model simulation, edge-parallel flows are already well developed and have approximately constant velocities except for the last grid cell (Fig. 5). The high edge velocities are partially a numerical artifact due to

the fixed grid. One should, however, note that the velocity of the MIZ is generally lower than the free-drift velocity. Introducing perturbations at the ice edge would give a free-drifting ice edge and, hence, a sharp increase in ice velocity close to the edge. The form of the compactness profile is very sharp (Fig. 6). For along-edge winds, the compactness drops from 0.8 to 0 in 8 km (two grid cells).

We can gain a perspective on the numerical solution by analytically examining the steady state adjustment case. In steady edge-parallel flow, the u velocity must be identically zero. The continuity equation is then automatically satisfied and the momentum equation becomes

$$-\frac{1}{2}\frac{dP}{dx} + \varrho_i h f v + \varrho_w C_w \sin\theta \, |v| v + \tau_{ax} = 0 \quad (12a)$$
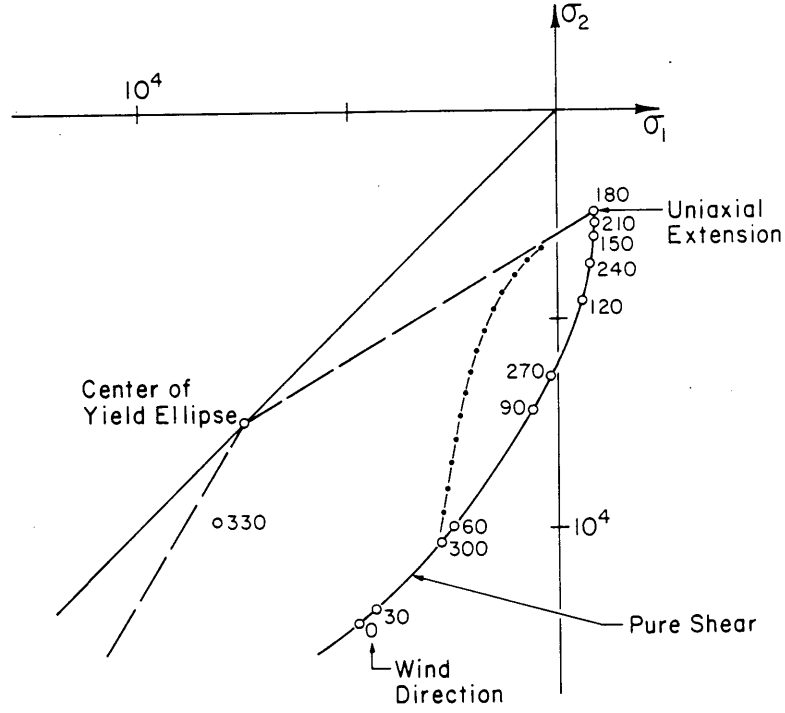
26

Fig. 4. The stress state for the initial MIZ flow. The open circles show the stress at the left-hand boundary, and the solid dots show the stress through the MIZ for 300°-wind case.

$$\frac{d}{dx}\left(\eta \frac{dv}{dx}\right) - \varrho_w C_w \cos\theta |v|v + \tau_{ay} = 0 \qquad (12b)$$

and now

$$\eta = P\Big/\left[2e^2 \max\left(\dot{\epsilon}_0,\ e^{-1}|\frac{dv}{dx}|\right)\right] \qquad (13)$$

Since $P = P(h,A)$, our problem contains three unknowns: ice thickness, compactness, and velocity. We have only two equations (12). The results, however, depend only weakly on the thickness and, hence, we take it as constant in the following analytic considerations.

Without shear strength, ice velocity must be constant, with the absolute value $[|\tau_{ay}|/\varrho_w C_w \cos\theta]^{1/2}$. For finite shear strength, the ideal plastic case is approached as $\dot{\epsilon}_0 \to 0$. Then, in plastic deformation

$$\eta \frac{dv}{dx} = \frac{P}{2e} sgn\left(\frac{dv}{dx}\right) \qquad (14)$$

and the pressure gradient can be easily eliminated from (12). Then we have a simple quadratic equation for v, and the solution is

$$|v| = \sqrt{(|\tau|/C_*)+(r/C_*)^2} - r/C_* \qquad (15)$$

where

$$|\tau| = |\tau_{ay}|-e^{-1}|\tau_{ax}| \qquad (16a)$$

$$C_* = \varrho_w C_w(\cos\theta \pm e^{-1}\sin\theta) \qquad (16b)$$

$$r = \pm e^{-1}\varrho_i hf \qquad (16c)$$

In $\pm$ pairs, $+$ is for southward flow and $-$ is for northward flow. For a given spatially constant wind stress the solution is constant. Thus, plastic slip occurs at the left-hand boundary, and in the MIZ ice velocity is the given constant while the stress state remains indeterminate.

Next, since v is constant, it follows directly from (12a) that P is linear:

$$P = \beta(x - L_0) \qquad (17)$$

where L_0 is the location of the ice edge after adjustment and

$$\beta = \tau_{ax} + \varrho_w C_w \sin\theta |v|v + \varrho_i hfv.$$

27

Standard Model Run

—— Model
---- Free Drift

With Adjustment (time = 48 hrs)

180°·
210°·
240°·
270°·
300°·

Interior Ice

330°·
0°·

Open Water

30°·
60°·
90°·
120°·
150°·
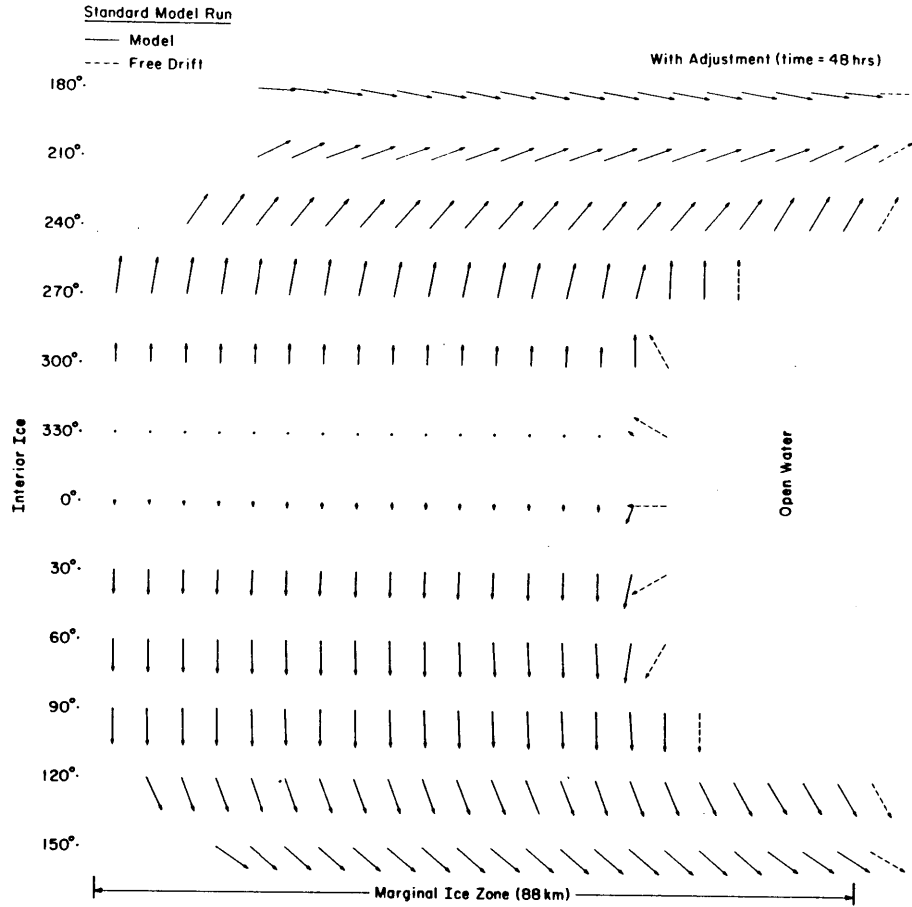
|—————————— Marginal Ice Zone (88 km) ——————————|

Fig. 5. The MIZ flow after 48 hours. The degree-numbers on the right give the direction of the geostrophic wind.

Naturally, for the solution to be valid β must be positive. Through (7) we can then obtain the compactness profile:

$$A = 1 + C^{-1}\log\left[\frac{\beta}{P_*h}(x - L_0)\right]. \qquad (18)$$

This analytic form gives a very sharp profile. For example, if $\beta \approx 0.05$ N m^{-2} then $A = 0.78$ at 4 km from the edge.

The model calculations at 48 hrs agree rather well with the ideal plastic steady state. In some cases the model solution has not yet fully developed to the steady state. The applied creep limit is so small that the results should really approximate well the ideal plastic flow. On the other hand, if the creep limit is increased, linear viscous flow is approached. Then the viscosity would be spatially varying and, as shown in Leppäranta (1983), it would be possible to obtain sharp changes in ice velocity close to the ice edge.

Discussion

The standard form of Hibler's (1979) viscous plastic sea-ice model predicts a nearly constant MIZ flow under constant forcing. If the free-drift solution is directed toward the open water, the MIZ loses contact with the interior ice and goes to the free-drift state. Otherwise there is generally a plastic slip at the boundary and the ice creeps elsewhere. The ice velocity is naturally less than the free-drift if the ice compactness is allowed to equilibrate in response to a given wind field. The profile of ice compactness is sharp close to the ice
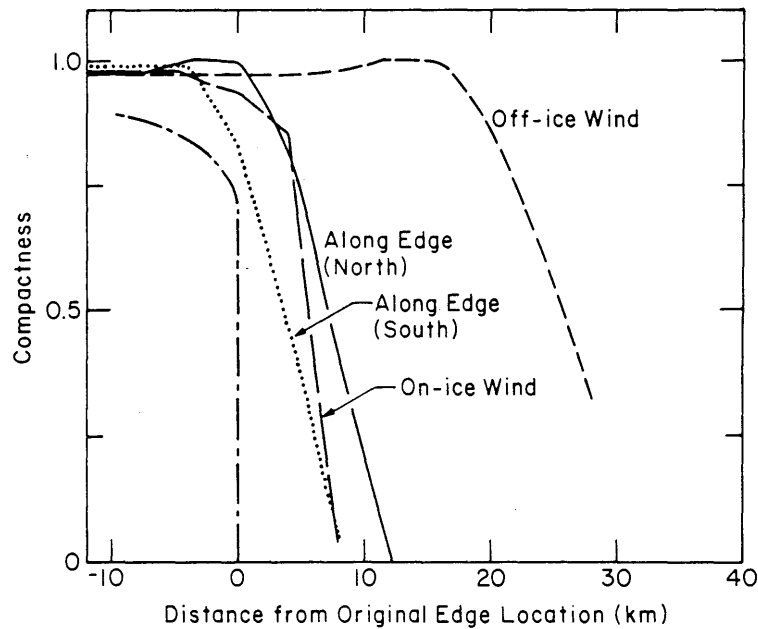
28

Fig. 6. The compactness profile after 48 hours. The line at 0 gives the ideal plastic analytic profile for along edge wind; the shape is relevant but not the location.

edge. Typically compactness drops from about 0.8 to 0 in about 5 km.

One overall feature of the model results is that in the absence of wind nothing happens, since with a plastic rheology the ice will not flow unless forced. This is in contrast to Røed and O'Brien's (1981) results where their simple pressure term causes the ice to flow and undergo geostrophic adjustment in the absence of wind. Results also show that divergence of ice near the ice margin is caused by ice interaction. Hence, divergence of ice cannot be used alone as an argument for the absence of ice interaction.

Recently considerable discussion has been devoted to the so-called "ice edge jet." Its existence has been indicated by the observations of Johannessen et al. (1983), but its nature is not known. The present results show that a jet-like feature can be present as a perturbation in an ideal plastic model. In addition, it may be possible that the ice behavior becomes more viscous-like when approaching the edge. This would increase the creep limit in the model. Then sharp velocity profiles would be possible, although they would still be restricted by the creep limit.

Model calculations have shown that the adjustment process may last several days and, hence, it is considered that the transient case needs further study.

This work was made possible by support from the office of Naval Research. The first author of this paper is supported by the U.S. Army European Research Office, Contract No. DACA45-83-C-0034, via a reimbursable ONR grant through USACRREL.

REFERENCES

Hibler, W.D., III, A dynamic thermodynamic sea ice model. *J. Phys. Oceanogr.,* **9,** 815-846, 1979.

Hibler, W.D., III, Documentation for a two-level dynamic thermodynamic sea ice model. CRREL Special Report 80-8, U.S. Army Cold Regions Research and Engineering Laboratory, Hanover, N.H., 1980.

Hibler, W.D., III and J.E. Walsh, On modeling seasonal and interannual fluctuations of Arctic sea ice, *J. Phys. Oceanogr.,* **12,** 1514- 1523, 1982.

Johannessen, O.M., J.A. Johannessen, J. Morison, B.I. Farrelly, and E.A.S. Svendsen, Oceanographic conditions in the marginal ice zone north of Svalbard in early fall 1979 with an emphasis on mesoscale processes, *J. Geophys. Res.,* **88,** 2755-2769, 1983.

Leppäranta, M., Analysis of linear sea ice models with an ice margin, this issue, 1984.

Røed, L.P. and J.J. O'Brien, Geostrophic adjustment in highly dispersive media: An application to the marginal ice zone, *J. Geophys. Astrophys. Fluid Dyn.,* **18,** 263-278, 1981.

Wadhams, P., A.E. Gill, and P.F. Linden, Transects by submarine of the East Greenland Polar Front, *Deep Sea Res.,* **26,** 1311-1328, 1979.

29

Analysis of Linear Sea Ice Models With an Ice Margin

M. LEPPÄRANTA

U.S. Army Cold Regions Research and Engineering Laboratory
Hanover, New Hampshire 03755

On leave from the Institute of Marine Research, Helsinki, Finland

The steady-state momentum equation of pack ice with linear viscous rheology is applied here to the marginal ice zone (MIZ). The linear approach makes it possible to obtain analytical solutions for certain interesting cases. A general major point is that in the MIZ we neglect variations parallel to the ice edge, which eliminates one independent space variable from the problem. This simplification has also been used in Røed and O'Brien (1981) and Leppäranta and Hibler (1984). A general solution with constant bulk and shear viscosities and spatially varying external forcing is derived, and selected special cases are shown. In addition, one specific case with spatially varying viscosity is considered.

Linear viscous rheology is a classical description of the pack ice material. It was first introduced by Laikhtman (1958) and extended later by Glen (1970). During the 1970s its applicability to the Arctic ice pack was questioned (e.g. Coon et al., 1974). The arguments against linear viscosity were mainly based on the ridging process, and it is not certain how they hold in the MIZ. There has been much speculation on the MIZ ice flow on the basis of the free drift law, and linear ice models give it a first-order correction that considers ice interaction.

In general form the steady-state momentum equation of pack ice is written as

$$\nabla \cdot \sigma - \varrho_i h f \mathbf{k} \cdot \mathbf{u} + \tau_w + \tau_a + \mathbf{G} = 0, \tag{1}$$

where σ is the ice stress tensor, ϱ_i is ice density, h is ice thickness, f is the Coriolis parameter, $\mathbf{k}$ is the unit vector vertically upward, $\mathbf{u}$ is (u,v) or ice velocity, τ_w is water stress, τ_a is wind stress and $\mathbf{G}$ is the gravitational force due to the sea surface tilt. In practice, under time-independent forcing the steady state is achieved within a few hours or less. Now the coordinate system is fixed so that the y-axis coincides with the ice edge. The MIZ covers the zone $(0 \le x \le L, y)$ where the line $x = L$ is the boundary between the MIZ and the interior ice pack (or coast). We assume that spatial variations are much larger perpendicular than parallel to the ice edge and hence ignore y-dependency. Thus all variables are functions of x only.

Linear viscous rheology is expressed (Glen, 1970) as

$$\sigma = 2\eta\dot{\epsilon} + (\zeta - \eta)\mathrm{tr}\,\dot{\epsilon}\,I \tag{2}$$

where $\dot{\epsilon} = \frac{1}{2}[\nabla\mathbf{u} + (\nabla\mathbf{u})T]$ is the strain rate tensor, I is the unit tensor, and η and ζ are the shear and bulk viscosities of ice. With zero y-derivatives,

$$\nabla \cdot \sigma = d_x[(\zeta + \eta)d_x u, \eta d_x v]. \tag{3}$$

We take the linear water-stress formula

$$\tau_w = c_w(\cos\theta + \sin\theta\,\mathbf{k}x)(\mathbf{U}_w - \mathbf{u}), \tag{4}$$

where c_w is the linear drag coefficient, θ is the turning angle in the oceanic boundary layer, and $\mathbf{U}_w$ is the geostrophic current velocity.

Denote

$$\mathbf{F} = \tau_a + c_w(\cos\theta + \sin\theta\,\mathbf{k}x)\mathbf{U}_w + \mathbf{G}. \tag{5}$$

Utilizing (3-5), (1) can be written in component form as

$$d_x[(\zeta + \eta)d_x u] - c_w \cos\theta\,u +$$

$$(c_w \sin\theta + \varrho_i h f)v + F_x = 0, \tag{6a}$$

31

$$d_x(\eta d_x v) - c_w \cos\theta\, v -$$

$$(c_w \sin\theta + \varrho_i h f)u + F_y = 0 \qquad (6b)$$

The boundary conditions are specified by no stress at the ice edge and a given ice velocity at the MIZ-interior ice boundary:

$$x = 0: \quad (\zeta + \eta)d_x u = \eta d_x v = 0 \qquad (7a)$$

$$x = L: \quad u = u_L, v = v_L. \qquad (7b)$$

General solution with constant viscosities

First, to shorten our notations, (6a) and (6b) are divided by the constants $\zeta + \eta$ and η, respectively, and rewritten as

$$d_{xx}u - \alpha_1 u + \beta_1 v + \gamma_1 = 0, \qquad (8a)$$

$$d_{xx}v - \alpha_2 v - \beta_2 u + \gamma_2 = 0, \qquad (8b)$$

where

$$(\zeta + \eta)\alpha_1 = \eta\alpha_2 = c_w \cos\theta,$$

$$(\zeta + \eta)\beta_1 = \eta\beta_2 = c_w \sin\theta + \varrho_i h f,$$

$$(\zeta + \eta)\gamma_1 = F_x, \quad \eta\gamma_2 = F_y. \qquad (9)$$

Using the elimination method, (8) can be combined to one for u:

$$d_{xxxx}u - (\alpha_1 + \alpha_2)d_{xx}u + (\alpha_1\alpha_2 + \beta_1\beta_2)u -$$

$$(\beta_1\gamma_2 + \alpha_2\gamma_1) = 0. \qquad (10)$$

Once this is solved, v is obtained directly from (8a).

The characteristic polynomial of (10) has the roots

$$\lambda_{1,2,3,4} = \pm\left[\frac{\alpha_1 + \alpha_2}{2} \pm \left(\frac{\alpha_1 - \alpha_2^2}{2} - \beta_1\beta_2\right)^{1/2}\right]^{1/2} \qquad (11)$$

and thus the solution is

$$u = \sum_{\ell=1}^{4} C_\ell \exp(\lambda_\ell x) + u_1, \qquad (12)$$

where u_1 is a particular integral of (10) and C_ℓ's are undetermined constants. Then,

$$v = \beta_1^{-1}\left[\sum_{\ell=1}^{4}(\alpha_1 - \lambda_\ell^2) C_\ell \exp(\lambda_\ell x) + \alpha_1 u_1 - d_{xx}u_1 - \gamma_1\right]. \qquad (13)$$

Clearly, the roots λ_ℓ consist of four real values when the expression in the brackets in (11) is nonnegative; this is true when

$$\frac{1}{2}\frac{e}{\sqrt{1 + e^{-1}}} \geq \tan\theta + \frac{\varrho_i h f}{c_w \cos\theta} \qquad (14)$$

where $e = \zeta/\eta$. Otherwise, the roots are two complex conjugate pairs. The constants C_ℓ are determined using the boundary conditions of (7). In the general case, one has to solve four simultaneous linear equations.

Constant viscosity and forcing

Now the free-drift solution

$$\mathbf{u} = \mathbf{u}_f = \frac{1}{c_w \cos\theta}\begin{pmatrix} 1 & -\xi \\ \xi & 1 \end{pmatrix}^{-1} \mathbf{F}, \qquad (15)$$

where $\xi = \tan\theta + \varrho_i h f/c_w \cos\theta$, is clearly a particular integral of (10). Thus

$$u = u_f + \sum_{\ell=1}^{4} C_\ell \exp(\lambda_\ell x), \qquad (16a)$$

$$v = v_f + \sum_{\ell=1}^{4} \frac{\alpha_1 - \lambda_\ell^2}{\beta_1} C_\ell \exp(\lambda_\ell x). \qquad (16b)$$

Constants C_ℓ and solutions (16) were calculated with a computer. The following parameters were held fixed:

$\varrho_i = 910$ kgm^{-3}	$\theta = 25°$
$h = 1.5$ m	$L = 100$ km
$f = 1.46 \times 10^{-4}$ s^{-1}	$u_L = 0$
$c_w = 0.55$ kgm^{-2} s^{-1}	$v_L = 0$

Inequality (14) is now valid for $e \geq 2.1$. This lies in a realistic range, so both real and complex characteristic roots λ_ℓ are possible.

We chose the standard viscosities of $\zeta = 2 \times 10^9$ kgs^{-1} and $\eta = 10^9$ kgs^{-1}. These are one order of magnitude lower than obtained by Hibler and Tucker (1979) for Arctic summer conditions, and one order of magnitude larger than used by Leppäranta (1981) in an ice forecasting model for the Baltic Sea. The ratio ζ/η was taken as the same as in the nonlinear model of Hibler (1979). The forcing term was set equal to 0.2 Nm^{-2} and directed 30° to the left from the positive y-axis (i.e. 30° off-ice with ice on the right). This choice gives nearly edge-parallel solutions.

The standard case results in v-velocity about 10% less than free drift at the ice edge (Figure 1).
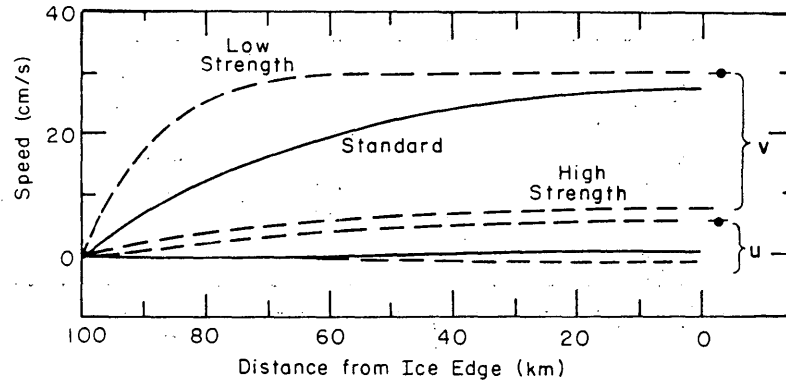
32

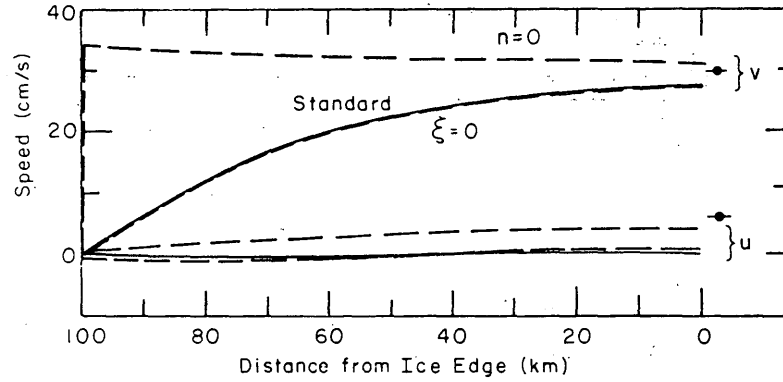Fig. 1. Standard, low — strength, and high — strength solutions. The symbols → — on the left show free — drift values.

Fig. 2. Solutions with no shear viscosity and with no bulk viscosity compared with the standard case. The symbols → on the left show free drift values.

Viscosity also slightly changes the direction from free drift and hence u-velocity is very small. In the standard case, $e = 2$ and the characteristic roots λ_f are complex. Consequently, there is an Ekman-type oscillation present in the solution. This has a small amplitude but still it can be seen in u-velocity. For comparison, low and high strength cases were solved (Figure 1); they were defined as having one order of magnitude lower and higher viscosities than the standard values (the ratio e was the same).

Removing the bulk viscosity does not change the standard case much because we consider basically an edge-parallel shear flow (Figure 2). The situation would be different if we had an on-ice forcing. With no shear viscosity v-velocity becomes larger than free drift value and even increases slightly towards the MIZ-interior ice boundary (Figure 2). This is easy to understand when looking at the original equations (6): with $\eta = 0$, v needs to satisfy a balance similar to free drift but with less retarding force through u because u is affected by bulk viscosity.

Constant viscosity and variable forcing

For simplicity, we neglect now the terms due to the earth's rotation, i.e., we set $\theta = 0$ and $f = 0$. In addition, the forcing is aligned with the ice edge. Then $u \equiv 0$ and v must be solved from

$$\eta d_{xx}v - c_w v + F = 0 \qquad (17)$$

This has a general solution

$$v = C_1 \exp(\lambda x) + C_2 \exp(-\lambda x) + v_1 \qquad (18)$$

where C_1 and C_2 are undetermined constants, $\lambda = \sqrt{c_w/\eta}$ and v_1 a particular integral of (17). We take now a quadratic polynomial for F,

$$F = F_0 + F_1 x + F_2 x^2 \qquad (19)$$

and then

$$v_1 = (1/c_w)(F_0 + 2F_2\lambda^{-1} + F_1 x + F_2 x^2). \qquad (20)$$

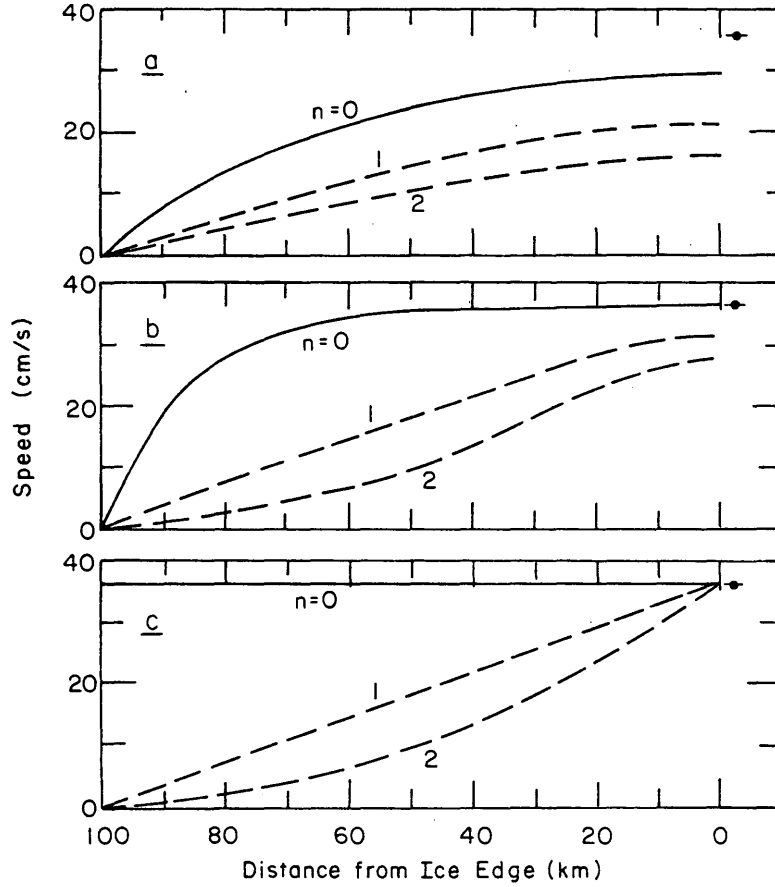Utilizing the boundary conditions $d_x v(0) = 0$,

Fig. 3. Variable forcing cases: a) standard ($\eta = 10^9$ kgs^{-1}), b) low strength ($\eta = 10^8$ kgs^{-1}), and c) free drift. The symbols $\rightarrow$—on the left show free-drift values at the ice edge.

$v(L) = 0$, the solution becomes

$$v = v_1 - v_1(L)\frac{\cosh(\lambda x)}{\cosh(\lambda L)} + \frac{F_1}{c_w\lambda}\frac{\sinh[\lambda(L-x)]}{\cosh(\lambda L)}.$$

(21)

We fixed as earlier $c_w = 0.55$ kgm^{-2} s^{-1} and $L = 100$ km. For F three cases are considered: $F = F_0(1-x/L)^n$, $n = 0$, 1, and 2; $F_0 = 0.2$ Nm^{-2}.

The free-drift solution is shown in Figure 3c. It illustrates also the form of the forcing term since now free drift equals c_w^{-1} times the local force. A nonzero viscosity smooths the curves especially near the ice edge where the no stress condition must be satisfied (Figures 3b, c). Let us look at the point where the speed has dropped by 20% from its value at the edge. With quadratic forcing, it is 11 km for $\eta = 0$, 20 km for $\eta = 10^8$ kgs^{-1}, and 30 km for $\eta = 10^9$ kgs^{-1}. Thus, to produce a sharp increase in the velocity near the ice edge in a con-

stant viscosity model, one must have a very sharp increase in forcing.

Variable viscosity and constant forcing

As above, we neglect the earth's rotation and align the forcing with the ice edge. Our equation for v is thus

$$d_x(\eta d_x v) - c_w v + F = 0 \qquad (22)$$

This can be solved for some specific forms of η only. We consider a quadratic function

$$\eta = \eta_L(x/L)^2, \qquad (23)$$

where η_L is the viscosity at the MIZ-interior ice boundary. Equation (22) becomes now the Euler equation

$$x^2 d_{xx} v + 2x d_x v - \frac{c_w L^2}{\eta_L} v + \frac{L^2 F}{\eta_L} = 0 \qquad (24)$$
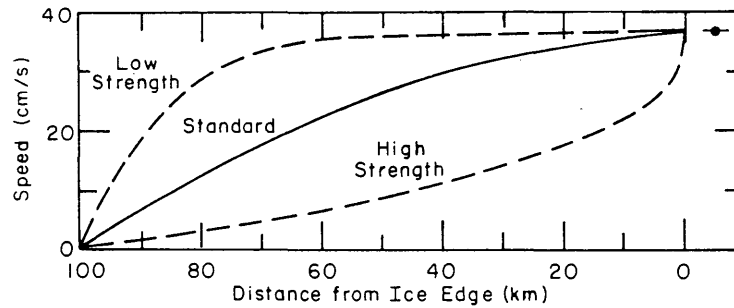
34

Fig. 4. Variable viscosity cases. The symbol ─•─ shows free-drift value.

which has a general solution

$$v = C_1 x^{\alpha_1} + C_2 x^{\alpha_1} + F/c_w, \qquad (25)$$

where C_1 and C_2 are undetermined constants and

$$\alpha_{1,2} = \pm \sqrt{c_w L^2/\eta_L + \frac{1}{4}} - \frac{1}{2}$$

(let α_1 take the plus sign). With the boundary conditions $\eta d_x v(0) = 0$, $v(L) = 0$, we have

$$v = (F/c_w)[1 - (x/L)^{\alpha_1}]. \qquad (26)$$

Three cases are considered: low, standard, and high strength, defined by $\eta_L = 10^8$, 10^9 and 10^{10} kgs^{-1}, respectively. The parameters c_w and L are as earlier and $F = 0.2$ Nm^{-2}.

The curvature of the velocity distribution across the MIZ may have either sign, depending on the magnitude of the limiting viscosity η_L (Figure 4). Since the viscosity and its gradient vanish at the ice edge, the ice velocity there equals the free-drift value. In the case of high strength, 20% drop in the velocity is reached at 1.6 km from the ice edge. Thus, sharp jet-like features in ice velocity can be produced by variations in the strength. Several kinds of viscosity distributions are of course possible. However, it seems reasonable to assume, as here, that the viscosity decreases to zero when the ice edge is approached.

Linear viscous law is a rather crude approximation of pack ice rheology. However, it is much more realistic than the free drift assumption and gives an insight into how the ice interaction may modify the velocity distribution. Especially, it is possible to obtain analytical solutions for the MIZ flow for certain interesting cases. In this work edge-parallel MIZ flow has been studied.

With constant viscosity and constant forcing, ice velocity does not vary much closer than 30–40 km to the ice edge (Figure 1). With the standard value of viscosity, the edge velocity was 10% less

than the free-drift. The solution may contain an Ekman-type oscillation of small amplitude [see (11)]. Monotonically varying forcing did not change the standard case (Figure 3) much, and thus the integral of forcing and not the local force is most significant. Free drift must follow the local force exactly. Variable viscosity may produce quite different forms of the velocity distribution (Figure 4). Especially, a very sharp change near the ice edge is possible. Much discussion has recently been devoted to such a feature, termed the "ice edge jet." It is clear that if the MIZ is loose it has no strength and obeys the free-drift law; the jet may then be caused by the forcing distribution only. But if the ice strength increases to a high value farther from the ice edge, the present results indicate that the jet can be produced by the variations in the strength alone.

This work was carried out at the U.S. Army Cold Regions Research and Engineering Laboratory, Hanover, N.H., and was supported by the U.S. Army European Research Office, Contract No. DACA45-83-C-0034.

REFERENCES

Coon, M.D., G.A. Maykut, R.S. Pritchard, D.A. Rothrock, and A.S. Thorndike, Modeling the pack ice as an elastic–plastic material, *AIDJEX Bull., 24,* 1–105, 1974.

Glen, J.W., Thoughts on a viscous model for sea ice, *AIDJEX Bull., 2,* 18–27, 1970.

Hibler, W.D., III, A dynamic thermodynamic sea ice model, *J. Phys. Oceanogr.,* 815–846, 1979.

Hibler, W.D., III and W.B. Tucker, III, Some results from a linear-viscous model of the Arctic ice cover, *J. Glaciol., 22,* 293–304, 1979.

Laikhtman, D.L., O vetrovom dreife ledjanykh polei, *Tr. Leningr. Gidromet. Inst., 7,* 129–137, 1958.

Lepparanta, M., An ice drift model for the Baltic

Sea, *Tellus, 33*, 583-596, 1981.

Lepparanta, M. and W.D. Hibler III, The role of ice interaction in marginal ice zone dynamics, this issue, 1984.

Røed, L.P. and J.J. O'Brien, Geostrophic adjustment in highly dispersive media: An application to the marginal ice zone, *Geophys. Astrophys. Fluid Dynam., 18,* 263-278, 1981.

Mesoscale Coupled Ice/Ocean Modeling of the Marginal Ice Zone

L.P. RØED

Det Norske Veritas, Research Division, P.O. Box 300, N-1322, Høvik, Norway

O.M. SMEDSTAD

University of Oslo, Institute of Geophysics, P.O. Box 1022, N-Oslo 3, Norway

This note presents some recent modeling efforts in which a thermodynamic model (Røed, 1983) is coupled with a dynamic model (Røed and O'Brien, 1983) to study the joint effect of thermodynamic and dynamic processes in the marginal ice zone (MIZ).

The dynamic model used in the result presented here is a numerical coupled ice/ocean model without internal ice stress. Røed and O'Brien (1983) reported that this model produces an oceanic response very similar to a model including internal ice stress (in the form of ice pressure), although the details of the ice concentration distribution were somewhat different. For details the reader is referred to the Røed and O'Brien (1983) paper. A nontrivial extension of this model is to allow for two or more ice edges to be present. This is an important feature if the model is going to be able to handle ice banding, etc. It is also important when the dynamic model is coupled to a thermodynamic model in that local melting (or freezing) may produce more than a single ice edge. As an example, Figure 1 depicts a situation where three ice edges are present. A band of ice with maximum ice concentration slightly above 20% and width about 10 km was added to the initial configuration. The subsequent development as displayed by Figure 1, with a wind similar to that of Røed and O'Brien (1983), shows that the band moves parallel to the main ice edge. This is to be expected since the ice in the band receives the same momentum from the atmosphere as the main pack.

The thermodynamic model is described in Røed (1983) and was developed with a coupling to the dynamic model in mind. An important feature of this model is that the melting and freezing processes on a microscale manifest themselves on the mesoscale predominantly by changing the ice concentration rather than average ice thickness. Røed argues that this is especially true in the MIZ. Here the random motion of the individual ice floes comprising the ice medium breaks up newly frozen ice. This ice in turn either forms into thicker and larger floes or it attaches itself to the already existing floes and thereby creates changes in compactness. In the thermodynamic model, the heat flux is simply parameterized to be proportional to temperature differences across thin boundary layers adjacent to the ice/ocean, ocean/atmosphere, and ice/atmosphere interfaces. To evaluate the necessary coefficients in this parameterization, a melting rate of 20 cm/day was first assumed, with an atmospheric temperature of about -2 °C and a mixed-layer temperature of 1 °C. This estimate is conservative when compared to a melting rate of 1 m/day, as reported by Josberger (1983) with similar ambient conditions. Furthermore, it was assumed that as time approached infinity the ice compactness reached a value of about 85% when the atmospheric temperature was as low as -32 °C. With this assumption, Røed (1983) showed that the freezing time scale was about 2 days (e-folding time) and that the melting time scale (only due to oceanic heat flux) was about 6 days.

The thermodynamic and dynamic models were coupled numerically. The same grid size and timestep were used in the integration of the two models. The chosen numerical procedure was to integrate the thermodynamic part before computing the effect of dynamics. The effect of the thermodynamic model is visualized in Figures 2a and b. These figures depict the result of the thermodynamic model alone. Initially, the ice concentration $A = 0$ everywhere. The atmospheric temperature is specified as a monotonically decreasing function northward (positive x) in the
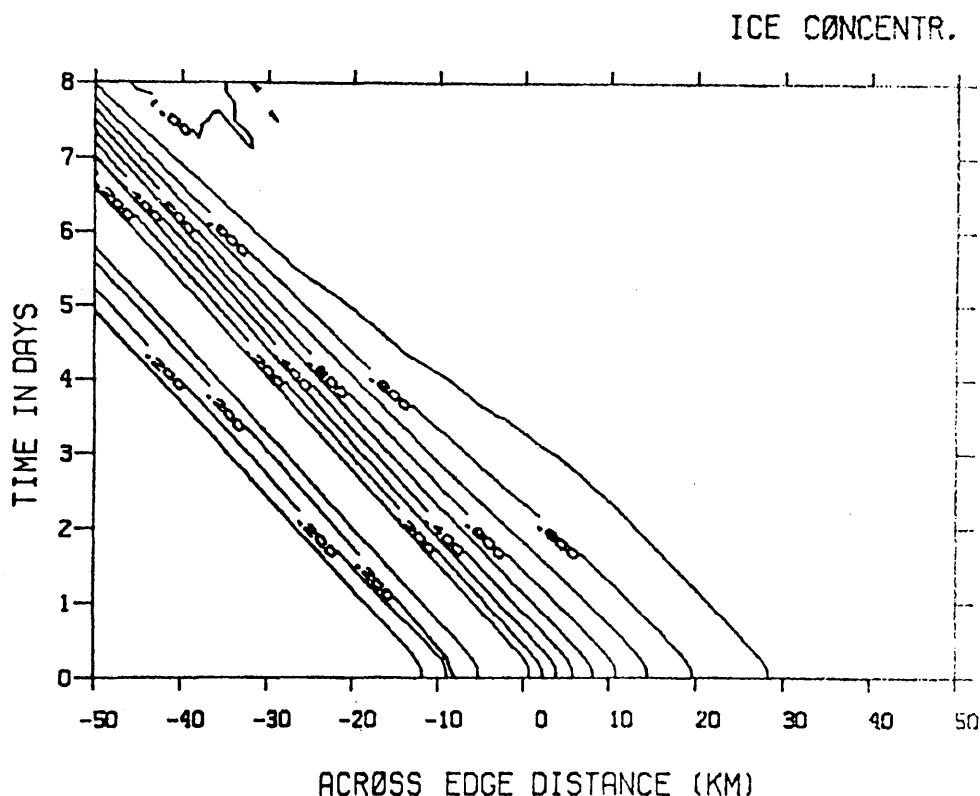
Fig. 1. Solid curves depict the response in time and space of the ice concentration. Numbers on lines refer to fraction of ice cover (0.2 = 20% concentration). Time in days is plotted along the vertical axis, while the across-edge coordinate measured from the initial position of the main edge (in km) is the horizontal axis. Initially the ice band is 3 km ahead of the main edge. The contour interval is 0.1.

form of a hyperbolic tangent. The specified forcing exhibits a front about 100 km wide where the atmospheric temperature drops from 3 °C to -32 °C. In the deep ocean the temperature is uniform equal to 1 °C. The initial mixed-layer temperature (Figure 2b) is specified as a hyperbolic tangent and drops from 2 °C in the south to -1.7 °C in the north on a scale similar to the atmospheric temperature.

We observe that the front in the atmospheric temperature produces a similar front in the ice concentration (Figure 2a) and oceanic temperature (Figure 2b). The most important property of this solution is the growth of a significant ice cover on a time scale short enough to yield interesting interaction with dynamics. For instance, 90 km to the right of the ice edge 90% ice cover is obtained in about 7 days (Figure 2a). To obtain a feeling for the effect this production of ice has on the dynamics, results from two test runs are shown in Figures 3 and 4. To resolve the impact of thermodynamics, the result from a run with no thermodynamics is shown (Figure 3). The applied wind

stress acts along the ice edge with the main pack to its right. Initially the distribution of ice was specified as in Røed and O'Brien (1983). This wind stress moves the ice pack northward (along the positive x-axis in Figure 3a) and produces the expected upwelling at the ice edge. This dynamically produced upwelling is close to 4 m in about 14 days. With thermodynamics coupled to the dynamics this upwelling is enhanced to about 5.5 m (Figure 4b). Note also that maximum upwelling has moved southward and that the width of the upwelling dome has decreased. The impact on the ice concentration is more drastic. The ice edge now becomes almost stationary in time due to the production of ice in the areas left by the main pack because of the wind. Thus, the areas that experience an ice cover are drastically enhanced, but the ice cover's concentration is too low to have the same drastic effect on the oceanic response. The impact of dynamics on the mixed-layer temperature as revealed by Figures 2b and 4c is seen to be negligible.

38

Fig. 2. (a) Same as Figure 1. In this case we have used the thermodynamic model alone. Initially the ice concentration was zero. (b) Dashed curves depict the mixed-layer temperature in °C. The vertical and horizontal axes are the same as in Figure 1. The contour interval is 0.08.
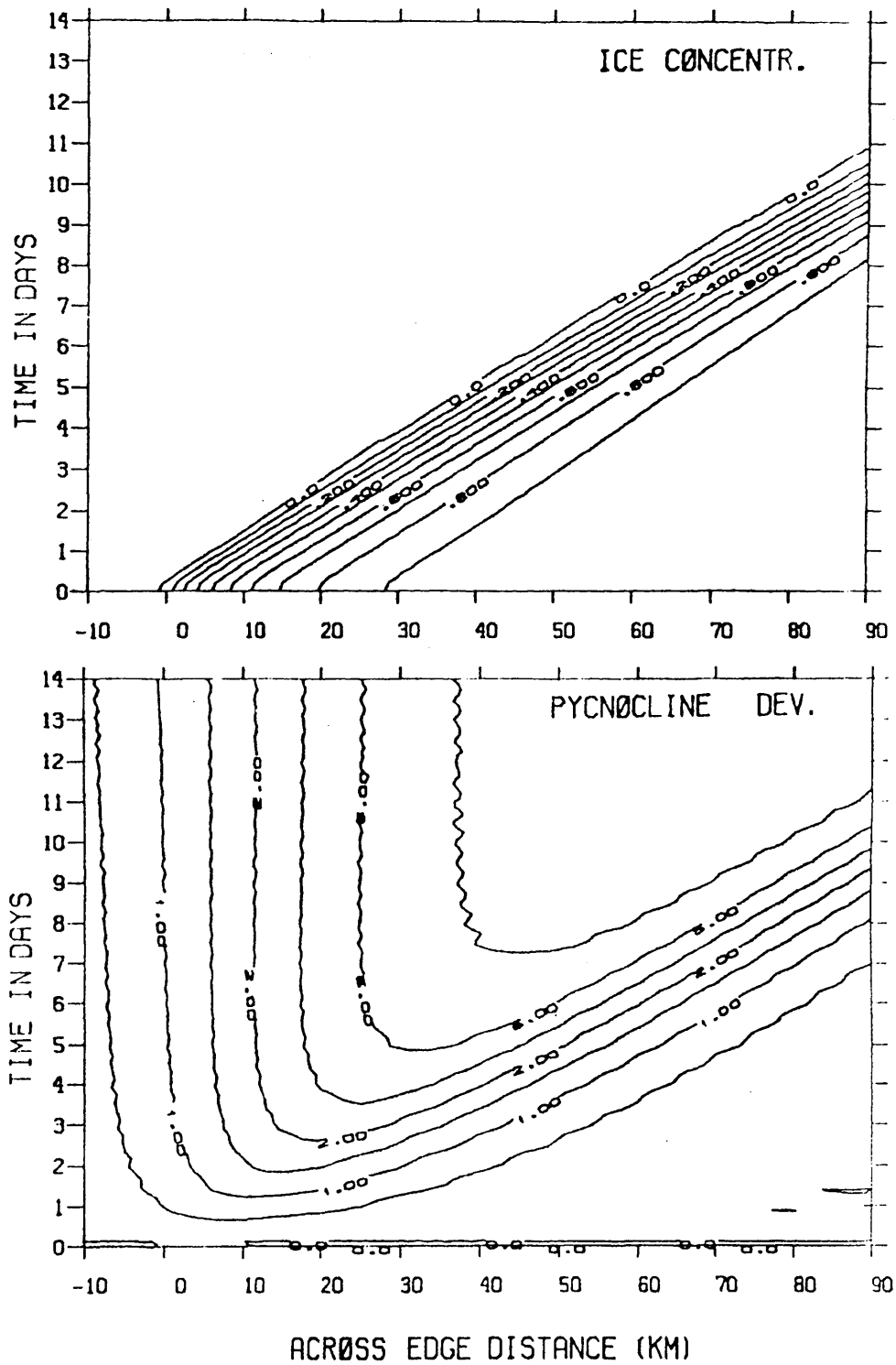
Fig. 3. (a) Same as Figure 2. In this case we have only one ice edge. (b) Solid curves show the time and space dependence of the pycnocline deviation (in m), away from its equilibrium position. Time in days is shown along the vertical axis. The across-edge distance (in km) is measured from the ice edge. The contour interval is 0.5.

Fig. 4. (a) Same as Figure 1. In this case the coupled model has been used. (b) Same as Figure 3b. In this case the coupled model has been used.
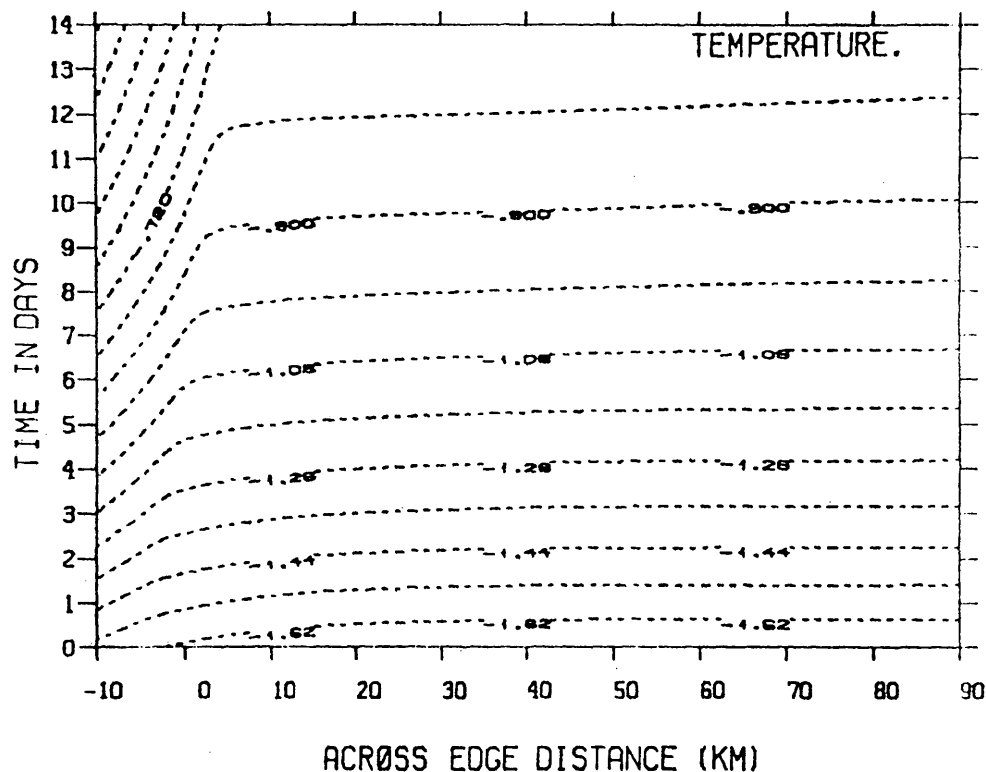
Fig. 4. (cont'd). (c) Same as Figure 2b. In this case the coupled model has been used. The contour interval is 0.09.

Further experiments with coupled thermo-dynamic and dynamic ice/ocean models of the MIZ are now underway and will be reported in the literature.

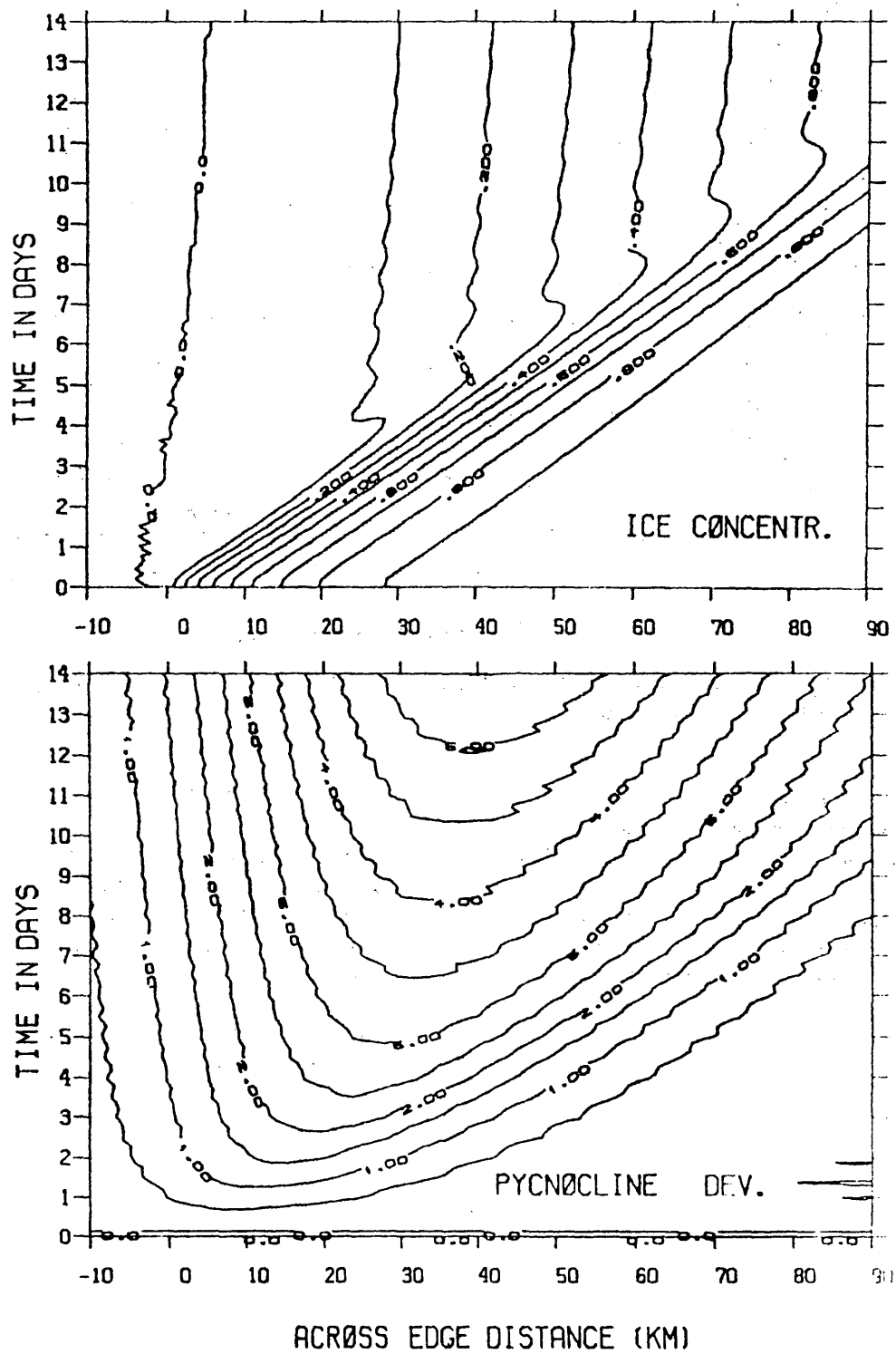This research was supported by the U.S. National Aeronautics and Space Administration through a subcontract with Florida State University.

REFERENCES

Josberger, E.G., Sea ice melting in the marginal ice zone, *J. Geophys. Res., 88*, 2841-2844, 1983.

Røed, L.P., A thermodynamic coupled ice-ocean model of the marginal ice zone, to be submitted, 1983.

Røed, L.P., and J.J. O'Brien, A coupled ice-ocean model of upwelling in the marginal ice zone, *J. Geophys. Res., 88*, 2863-2872, 1983.

Some Simple Concepts on Wind Forcing
Over the Marginal Ice Zone

W.B. TUCKER III
U.S. Army Cold Regions Research and Engineering Laboratory
Hanover, New Hampshire 03755

Recently, considerable attention has been given to a possible ice edge jet, a phenomenon in which there is a large ice velocity shear normal to the ice margin, with the largest velocities occurring at the edge itself. Johannessen et al. (1983) cite an example in which a buoy located on an ice floe at the ice edge drifted faster than others located farther into the ice or outside the edge. In that case, the strong velocity shear occurred under conditions in which the wind had a large along-edge component. Johannessen et al. (1983) also present an excellent review of the potential causative mechanisms. They suggest that the jet is a wind-driven feature caused by increased coupling between the ice and the wind at the edge. Two proposed mechanisms for the increased wind coupling are an increase in wind drag near the edge and a decrease in the internal ice stress at the edge. They concluded that, for their example, even together these effects could not account for the total observed velocity differences but may still be important mechanisms. They also mention that an ocean current, associated with upwelling along the edge, and wave radiation pressure may enhance ice velocities.

Other mechanisms have also been proposed. Vinje (1977) and Paquette (1982) feel that ice edge jets may be associated with oceanic jets caused by strong frontal shears. Røed and O'Brien (1981) obtained an ice jet in an analytical model in which the Coriolis force was balanced only by internal ice pressure. Leppäranta (1984) and Leppäranta and Hibler (1984) show analytical and model simulation results that indicate that various assumed ice interactions can significantly alter the velocity distribution across the MIZ, some resulting in an edge jet.

A combination of some of these proposed mechanisms may be responsible for an ice edge jet. Although Johannessen et al. (1983) showed evidence of increased wind/ice coupling at the edge, variations in the wind field itself across the MIZ have not been proposed as a potential mechanism. Recent studies (Lindsay and Comiskey, 1982; Andreas et al., 1983; Macklin, 1983) have shown significant boundary layer modification in both on-ice and off-ice winds near an ice margin. This modification results from changes in surface roughness and in the rate of atmospheric heating between the ice and the ocean. However, observations that may detect variations in the wind field across the MIZ are lacking. In this paper, I will discuss some basic concepts that may influence the wind field over the East Greenland MIZ.

Sigtryggsson and Stefansson (1969) believe that, under certain conditions, an atmospheric front exists along the ice edge. They cited as observational evidence the many reports of bad weather and increased winds in the ice edge region. The reasoning is that very cold polar air can pass over compact ice without significant warming, but when it crosses the ice edge, it is warmed by the ocean and is forced aloft. These are the requirements for the formation of a shallow front in this region. The frontal region then comprises a pressure-density solenoid with sufficient energy to generate circulation within the solenoid. They further conjecture that this circulation leads to increased winds in the direction of the solenoid or parallel to the ice edge. No explanation of how the circulation is translated into parallel winds is given, only that experience (presumably reports) indicates that this situation is, in fact, realistic. Figure 1 shows their conception of the expected winds along the ice edge and a schematic cross-section of the hypothetical front.

This hypothesis is certainly attractive, because it results in winds blowing parallel to the edge. However, a physical explanation for the generation of
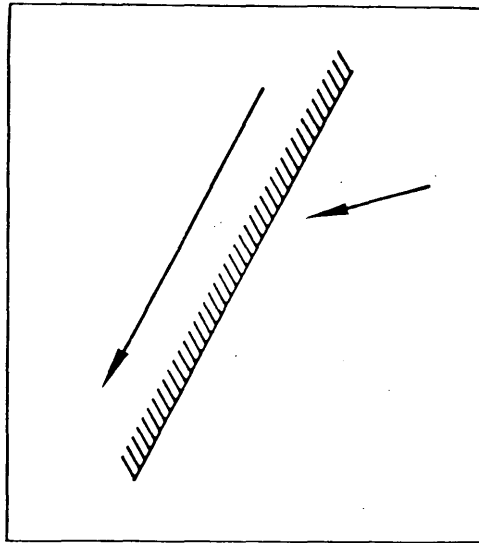
43

Fig. 1a. Expected wind direction in the vicinity of the ice edge (from Sigtryggsson and Stefansson, 1969).
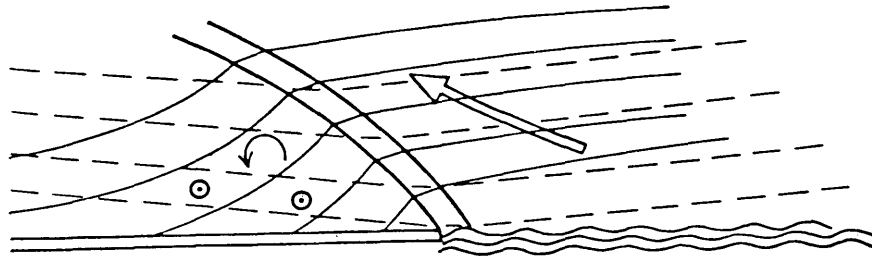

Fig. 1b. A vertical cross-section of the atmosphere above the leading edge of the ice pack viewing to the north. Solid lines are isotherms, dotted lines are isobars. The double line represents the frontal boundary. Currents blowing toward the viewer are indicated by a circle enclosing a point (from Sigtryggsson and Stefansson, 1969).

the circulation and the transition into horizontal currents was not presented. The generation of circulation around a pressure-density solenoid is described by Holton (1972) in application to land and sea breezes. This circulation and means of turning the wind parallel to the ice edge are discussed below with reference to the possibility of an ice breeze. The presence of a front as proposed by Sigtryggsson and Stefansson (1969) is probably analogous to the proposed ice breeze, both being solenoidal cells caused by a large thermal gradient across the ice edge.

The ice breeze (McPhee, 1980) is an ice-margin analogy to the temperate-zone sea or land breeze. Like the ice edge jet, this speculative mechanism would also be dependent upon a large thermal contrast. The atmospheric temperature gradient required is again due to the presence of cold, dense air over the ice and of significantly warmer air over the ocean.

The essence of the ice breeze idea is that there will be a thicker isobaric layer over the ocean than over the ice because of the difference in air densities (Figure 2). A downward-sloping pressure gradient from sea to the ice develops and accelerates the air from sea to ice at shallow upper levels. The resulting flow causes a mass (pressure) increase over the ice and a decrease over the ocean at the surface; an acceleration of air from ice to ocean results. Holton (1972) presents an idealized solution employing the Kelvin circulation theorem to give the acceleration of the wind at the land/sea interface:

$$\frac{d\bar{v}}{dt} = \frac{R(\bar{T_2}-\bar{T_1})}{2(h+L)} \ln \frac{p_0}{p_1} \qquad (1)$$
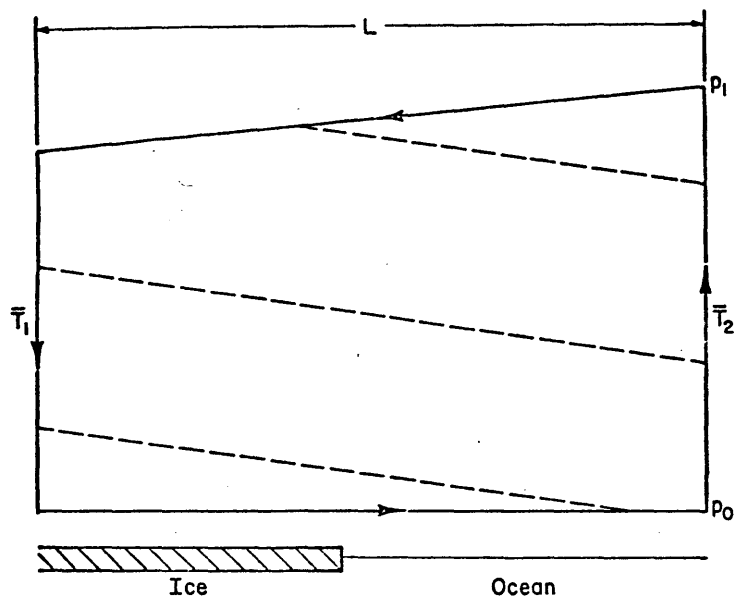
44

Fig. 2. Schematic of proposed ice-breeze circulation cell. Dashed lines indicate isoteric (constant specific volume) surfaces.

where R is the gas constant, $\overline{T_1}$ and $\overline{T_2}$ are the average air temperatures in the layer over land ($\overline{T_2}$) and ocean ($\overline{T_1}$), p_0 is the surface pressure, p_1 is the upper level pressure, h is the height, and L is the cell dimension normal to the land. For an assumed ice breeze, we would consider $\overline{T_1}$ to be over the ice and $\overline{T_2}$ to be over the ocean, as shown in Figure 2. Holton (1972) cites an example giving p_0 as 1000 mb, p_1 as 900 mb, $\overline{T_2}-\overline{T_1} = 10\,°C$, $L = 20$ km, and $h = 1$ km, which results in an acceleration of ≈ 0.68 cm s^{-2}, neglecting frictional effects. Kozo (1982a) points out, in making a case for sea breezes occuring in summer off the Alaskan coast, that the height scale (h) will be about half that in the mid-latitudes because the Arctic typically has a shallower boundary layer capped by an inversion. In addition, he found a length scale (L) of about 40 km. This large length scale and smaller cell height tend to reduce the acceleration given by (1); however Kozo (1982a) reports a temperature contrast ($\overline{T_2}-\overline{T_1}$) of approximately 20 °C. From (1) then, the Arctic wind acceleration values are comparable to those in the mid-latitudes, so an Arctic sea breeze seems possible. For our presumed ice-edge circulation cell we will certainly have the inversion conditions described by Kozo (1982a), with perhaps even a shallower boundary layer. We would also expect a length scale similar to his. However, we have been unable to ascertain what the layer temperatures across the ice edge may be in the East Greenland region during winter or summer. Taking values obtained during winter

across the Bering Sea MIZ (although under off-ice winds) (Lindsay and Comiskey, 1982), we find $\overline{T_2}-\overline{T_1}$ to be about 5 °C. This value is likely to be conservative for the East Greenland MIZ, which contains thicker and more compact ice than does the Bering Sea. However, even with this value an acceleration of 0.1 cm s^{-2} is obtained, enough to justify investigation of this mechanism.

There is another key difference between density-driven winds in high- and mid-latitude regions. During summer and winter and in high latitudes there is no reversal of the phenomenon (sea to land and vice versa) because of the absence of diurnal solar forcing. Moritz (1977) and Kozo (1982a) pointed out that under constant forcing (due to 24-hour irradiance in summer), the wind generated by this process has sufficient time to adjust to the Coriolis force. Moritz (1977) suggested that the Alaskan sea breeze eventually produced an alongshore component because of the larger horizontal extent of the coastline, continuous solar forcing, and a large Coriolis force. Kozo (1982a, b) verified these effects with observations and model predictions. For the case of an off-ice breeze generated by the increased pressure gradient over the ice, the Coriolis force would turn the wind to the right under continuous forcing; but a 360° turning is prohibited because the sea/ice temperature difference remains positive. The result is a wind with an along-ice component.

As mentioned above, solar irradiance is continuous during summer and absent in winter. The
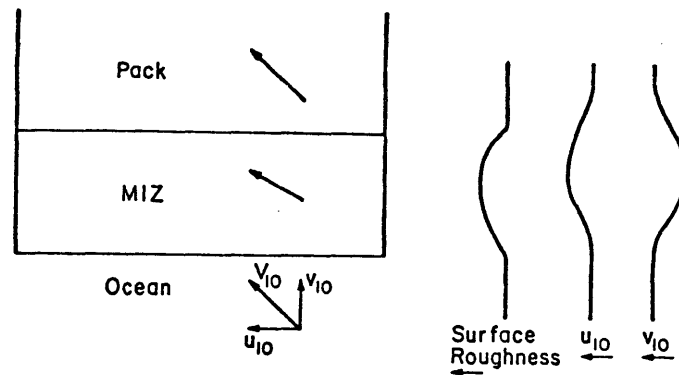
Fig. 3. Schematic of wind vector (V_{10}) *response due to surface roughness over the MIZ. Assumed roughness and along-edge and across-edge wind components* (u_{10}, v_{10}) *across the region are also shown.*

question then is whether the thermal gradient across the ice edge is large enough for the ice breeze to occur during either of these seasons. An additional concern is how the large stabilities and shallow boundary layers limit the vertical development of the circulation cell. The largest thermal gradient occurs in winter, yet the deepest boundary layers are in summer. The effect of synoptic scale winds on the hypothetical ice breeze also needs to be addressed. All of these concerns stress the need for observations.

Aside from winds being generated by the thermal contrast between the ice and the ocean, we must consider the effects of the MIZ on an existing synoptic wind. In particular, varying frictional forces caused by changing surface types and increasing stability over the ice are likely to produce noticeable effects. It is well established that the Ekman turning angle α, between the geostrophic wind and the surface wind, increases with both atmospheric stability and surface roughness. Likewise, the ratio of the surface wind to the geostrophic wind (v_{10}/Vg) decreases with stability and surface roughness.

Figure 3 shows qualitatively the expected effects of surface roughness on the wind profile for an on-ice wind over the MIZ. For this situation, we consider that surface roughness increases from the ocean to the MIZ, then decreases again over the smoother pack ice. This is consistent with recent measurements of drag coefficients in the Antarctic MIZ (Andreas et al., 1983) and the Bering Sea MIZ (Macklin, 1983). The lower roughness over smoother pack ice is consistent with drag coefficients measured over pack ice by Banke et al. (1980), who showed it to be close to the open ocean value. Figure 3 shows schematically the ex-

pected turning and decreasing of the wind vector in the MIZ and the readjustment over the smooth ice. The increasing roughness and the expected profile of the along-ice wind component, u_{10}, are also in the diagram. Notice that the turning gives a larger along-ice component relative to the across-ice component (v_{10}) in the MIZ.

A similar qualitative analysis can be carried out for stability, as shown in Figure 4. Here it is assumed that stability will increase through the MIZ and pack ice, a reasonable assumption since less heat escapes to the atmosphere through the more compact ice. As shown, we expect a turning and decreasing wind vector with an increasing along-ice component (u_{10}) relative to the across-ice component (v_{10}). A linear increase in stability or the wind components, as drawn, is not necessarily anticipated; the sketches simply illustrate the overall effect.

What is not clear for the edge is the relative magnitude of either of these effects. Overland et al. (1983) conducted studies of the Bering Sea MIZ using a numerical boundary layer model. Although their model was for an off-ice wind, the conclusions are somewhat applicable to this scenario. One important effect is that the wind and height of the boundary layer had a larger response to changes in surface roughness than to changes in surface heating. Not only does this imply that the roughness may create more significant effects than stability, but that roughness will also influence the stability in the MIZ. The model does demonstrate decreased windspeeds in the MIZ although the relative u and v components are not shown. One would have to assume that increased turning accompanied the decrease in speed.

Thus, the interaction between stability and sur-

Appl. Meteor., 21, 891-905, 1982a.

Kozo, T.L., A mathematical model of sea breezes along the Alaskan Beaufort Sea coast, Part II, *J. Appl. Meteor., 21,* 906-924, 1982b.

Leppäranta, M., Analysis of linear sea ice models with an ice margin, this issue, 1984.

Leppäranta, M., and W.D. Hibler III, The role of ice interaction in marginal ice zone dynamics, this issue, 1984.

Lindsay, R.W., and A.L. Comiskey, Surface and upper air observations in the eastern Bering Sea, February and March, 1981, *Tech. Memo.,* ERL-PMEL-35, NOAA, Washington, D.C., 90 pp., 1982.

Macklin, S.A., The wind drag coefficient over first-year ice in the Bering Sea, *J.Geophys. Res., 88,* 2845-2852, 1983.

McPhee, M.G., Physical oceanography of the seasonal sea ice zone, *Cold Reg. Sci. and Tech., 2,* 93-118, 1980.

Moritz, R.E., On a possible sea breeze circulation near Barrow, Alaska, *Arctic Appl. Res., 9,* 427-431, 1977.

Overland, J.E., R.M. Reynolds, and C.H. Pease, A model of the atmospheric boundary layer over the marginal ice zone, *J. Geophys. Res., 88,* 2836-2840, 1983.

Parish, T.R., The influence of the Antarctic Peninsula on the wind field over the Western Weddell Sea, *J. Geophys. Res., 88,* 2684-2692, 1983.

Paquette, R.G., Cruise report USCGC *Northwind,* October-November 1981, Naval Postgraduate School, Monterey, Calif., 1982.

Røed, L.P., and J.J. O'Brien, Geostrophic adjustment in highly dispersive media: An application to the marginal ice zone, *J.Geophys. Astrophys. Fluid Dyn., 18,* 263-278, 1981.

Schwerdtfeger, W., Mountain barrier effect on the flow of stable air north of the Brooks Range, in *Proceedings of the 24th Alaskan Science Conference,* 204-208, Geophysical Institute, University of Alaska, Fairbanks, 1974.

Schwerdtfeger, W., Meteorological aspects of the drift of ice from the Weddell Sea toward the mid-latitude westerlies, *J. Geophys. Res., 84,* 6321-6327, 1979.

Sigtryggsson, H., and U. Stefansson, Properties of drift ice: its formation and growth, *Hafisinn,* 207-223, 1969.

Vinje, T.E., Sea ice studies in the Spitzbergen-Greenland area, Landsat Report E77-10206, U.S. Dept. of Commerce, National Technical Information Service, Springfield, Virginia, 1977.
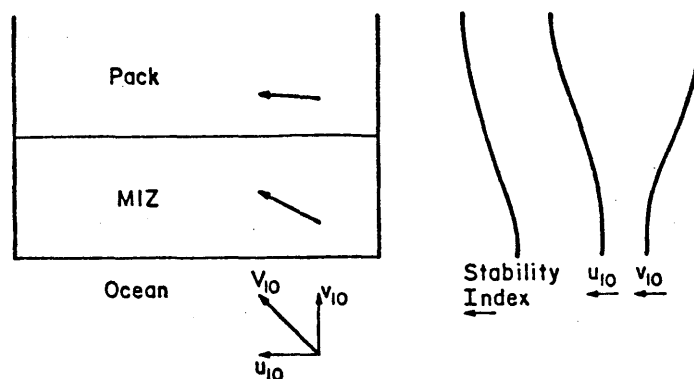
Fig. 4. Schematic of wind vector (V_{10}) *response due to increasing stability across the MIZ. Assumed index of stability and along-edge and across-edge wind components* (u_{10}, v_{10}) *across the region are also shown.*

face roughness and their combined effect on winds in the MIZ is likely to be quite complex. What we can expect for our hypothetical case is an increase in the along-edge component relative to the component normal to the edge. Because the greatest effect is not likely to be at the ice edge, but deeper in the MIZ, it is unlikely that they contribute to an ice edge jet. However, modeling studies should be carried out for various situations to investigate the response of the wind as a function of the roughness and compactness of the ice.

Barrier winds may also affect the East Greenland MIZ. These winds are essentially caused by a surface pressure gradient resulting from an increase of mass at the base of mountain chains that have effectively dammed the cold, dense air. The phenomenon has been observed in the western Weddell Sea along the Antarctic Peninsula (Schwerdtfeger, 1979) and on the north slope of the Alaskan Brooks Range (Schwerdtfeger, 1974). A recent numerical study by Parish (1983) indicates that these winds may be present in the regions several hundred kilometers from the geographic barrier. The close proximity of high-elevation Greenland makes this a distinct possibility in the East Greenland MIZ.

Some simple concepts that may produce variable wind forcing in the MIZ have been presented. Although the ice edge jet is probably the result of several interacting mechanisms, the atmospheric contribution cannot be neglected. With an expected large thermal contrast in the atmosphere across the ice edge, mesoscale features such as fronts or cellular circulations analogous to land breezes may exist. Larger scale features such as the adjustment of the pressure surfaces to the density surfaces, resulting in stronger geostrophic

winds, are also a possibility. The presence of an ice cover of varying thickness and compactness implies that surface roughness and atmospheric stability will also vary. These changes can also be expected to modify the synoptic winds flowing over the MIZ.

These hypotheses need to be carefully examined. Detailed investigations will require many field observations, made during all seasons. Unfortunately, this is one of the more difficult areas of the world from which to obtain observations. Modeling of the lower atmosphere over ice and adjacent oceans can proceed, but the models will require these observations for initialization and testing.

REFERENCES

Andreas, E.L, W.B. Tucker III, and S.A. Ackley, Variation of the drag coefficient across the Antarctic marginal ice zone, this issue, 1984.

Banke, E.G., S.D. Smith, and R.J. Anderson, Drag coefficients at AIDJEX from sonic anemometer measurements, in *Sea Ice Processes and Models*, edited by R.S. Pritchard, University of Washington Press, Seattle, 430-442, 1980.

Holton, J.R., *An Introduction to Dynamic Meteorology*, Academic Press, 319 pp., 1972.

Johannessen, O.M., J.A. Johannessen, J. Morison, B.A. Farrelly, and E.A.S. Svendsen, Oceanographic conditions in the marginal ice zone north of Svalbard in early fall 1979 with an emphasis on mesoscale processes, *J. Geophys. Res.*, *88*, 2755-2769, 1983.

Kozo, T.L., An observational study of sea breezes along the Alaskan Beaufort Sea coast, Part I, *J.*

Wind-Driven Ice Drift in a Shallow Sea*

J.E. OVERLAND, H.O. MOFJELD, AND C.H. PEASE

Pacific Marine Environmental Laboratory/NOAA, Seattle, Washington 98115

The purpose of this paper is to extend the analytic solutions for the coupled ice/ocean free-drift problem to finite depth (Shuleikin, 1938; Reed and Campbell, 1962; Neralla et al., 1981; Pease and Overland, in press). The intent is to examine the role of bathymetry in influencing the wind drift of ice in shallow seas of the seasonal ice zone, such as the Bering, Chukchi, and Barents Seas, which have significant areas with depths less than 50 m. Solutions for ice drift and current velocity in a shallow sea with neutral stratification are obtained as a function of wind stress, ice thickness, and water depth. The ocean is treated using Ekman-Taylor similarity with second-order closure to determine the turbulent intensity; this allows continuous solutions from 5 m total depth to deep water. Examples are shown with drag coefficients for the air/ice, ice/water, and water/bottom interfaces specified from recent surveys from the northern Bering Sea, a region with a broad continental shelf with a significant area of water depth between 30 and 50 m. The solution shows little dependence on water depth for depths greater than 30 m and wind speeds less than 15 m/s, because the level of turbulent mixing decreases with water depth for a given wind speed for depths less than 50 m.

We begin by assuming that the ice is wind-driven and in free drift. The ocean is neutrally stratified, which is valid in the Bering Sea away from the outer marginal ice zone in winter (Kinder and Schumaker, 1981). The ocean is modeled using second-order closure (Mellor and Yamada, 1982; Mofjeld and Lavelle, 1983); expanding the classical, two-layer Ekman-Taylor solution under the ice (McPhee, 1982) with an additional bottom boundary layer proved less than satisfactory in providing a continuous solution from shallow to deep water.

The steady-state, vertically integrated momentum equation for the ice in free drift using complex notation ($i^2 = -1$) is

$$C + \tau_a - \tau_w = 0 \tag{1}$$

with

$$C = -i\varrho_I h_I f \mathbf{V}_I$$

and $\mathbf{V}_I = u_I + iv_I$, where u_I and v_I are the east and north components of the ice velocity, f is the Coriolis parameter, ϱ_I is the ice density, and h_I is ice thickness. Boldface symbols indicate vector quantities, while italic symbols denote scalar magnitude. Air/ice stress is given by a drag law:

$$\tau_a = \varrho_a C_a V_a \mathbf{V}_a \tag{2}$$

where $\mathbf{V}_a$ is the relative air/ice velocity, $\mathbf{V}_a - \mathbf{V}_I$; ϱ_a is the air density; and C_a is the air/ice drag coefficient. The reference level in the air forcilitates comparison with Bering Sea measurements (Macklin, 1983; Pease et al., 1983).

Given ϱ_I, h_I, f, ϱ_a, C_a, and $\mathbf{V}_A$, an additional relation is needed to close the system of equations (Shuleikin, 1938; Reed and Campbell, 1962) between the ice/water stress τ_w and $\mathbf{V}_I$ for finite depth ocean. This relation is obtained by solving the stress-driven flow problem in the ocean. The steady-state momentum equation for the ocean is

$$i\varrho_o f \mathbf{V} = \frac{\partial \tau}{\partial z} \tag{3}$$

where $\mathbf{V}$ is the water velocity, ϱ_o is the water density, and τ is the horizontal component of stress defined as:

$$\frac{\tau}{\varrho_o} = A \frac{\partial \mathbf{V}}{\partial z} \tag{4}$$

with A an eddy coefficient (Neumann, 1968). We will treat (3) and (4) as a coupled system of first-

order differential equations subject to the boundary conditions:

$$\tau = \tau_w \text{ at } z = H - z_w, \text{ and}$$

$$\mathbf{V} = 0 \text{ at } z = z_B \tag{5}$$

where z_w and z_B are the roughness lengths of the ice/water interface and the bottom respectively, and H is the water depth.

One of the simplest differential models (Mofjeld and Lavelle, 1983) of the turbulent mixing has the eddy viscosity proportional to the product:

$$A = S_m q \ell \tag{6}$$

where S_m is a proportionality constant, ℓ is a prescribed mixing length, and q is the turbulent intensity determined by local balance between shear generation and viscous dissipation:

$$\frac{\tau}{\varrho_o} \frac{\partial V}{\partial z} - \frac{q^3}{c\ell} = 0 \tag{7}$$

where c is the dissipation constant. Since the turbulent production represented by the first term in (7) cannot depend upon how the turbulence is dissipated (Mofjeld and Lavelle, 1983), q must be proportional to $c^{1/3}$. Using this fact and substituting the eddy coefficient stress relations (4) and (6) into (7) gives

$$q = c^{1/3} \ell \frac{\partial \mathbf{V}}{\partial z}, \tag{8}$$

and thus

$$A = \ell^2 \frac{\partial \mathbf{V}}{\partial z}. \tag{9}$$

The mixing length decreases toward both boundaries, and in deep water approaches an asymptotic mixing length, ℓ_o, sufficiently far from the boundaries:

$$\ell = kz(H-z) [1 + kz(H-z)/(\ell_o H)]^{-1} H^{-1}, \tag{10}$$

with k the Von Karman constant and ℓ_o determined by the vertical distribution of turbulent intensity (Weatherly and Martin, 1978; Mellor and Yamada, 1982) below the ice:

$$\ell_o \equiv \gamma L = \gamma \int_{z_B}^{H-z_w} (H-z) q \, dz \left[\int_{z_B}^{H-z_w} q \, dz \right]^{-1} \tag{11}$$

where L is the scale height of the turbulent intensity and γ is an empirical mixing length parameter. Implicit in (11) is the assumption that the turbulence generated in the surface layer under the ice dominates the viscosity.

The solution for the steady Ekman problem,

$$\mathbf{V} = \mathbf{A}\phi_1 + \mathbf{B}\phi_2, \tag{12}$$

was obtained by integrating (3) and (4) using a fourth-order Runge–Kutta scheme to determine the vertical structure functions, ϕ_1 and ϕ_2, and matching the boundary conditions to find $\mathbf{A}$ and $\mathbf{B}$. The vertical spacing, S, of the solution is decreased near the boundaries and scaled by the local roughness lengths to provide better resolution in regions of large shear:

$$S = \frac{\ln(z/z_B)}{\ln[(H-z_w)/z_B]} - \frac{\ln[(H-z)/z_w]}{\ln[(H-z_B)/z_w]} \tag{13}$$

For these calculations, 1001 vertical points were used. The initial profile of viscosity increased linearly away from both boundaries and thereafter (9) was used. The ocean was coupled to the ice by iteration on (1), initially setting $\tau_w = \tau_a$, and solv-
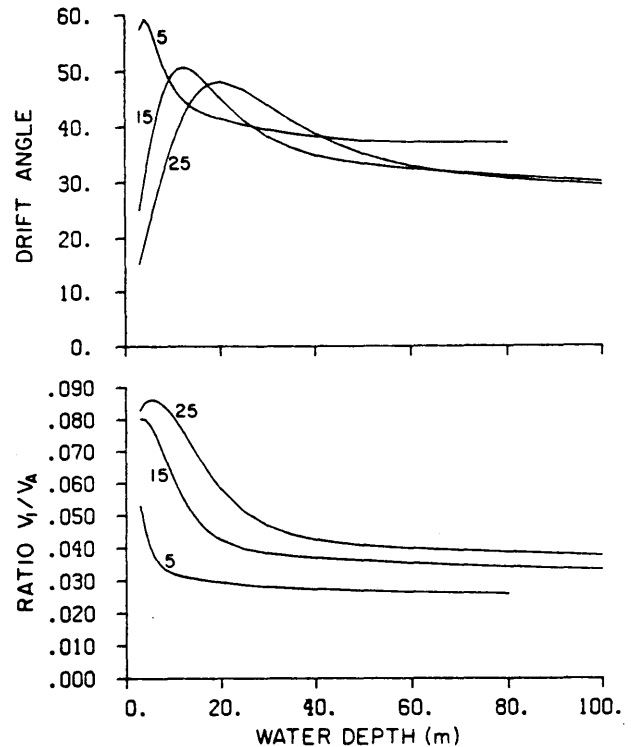

Fig. 1. The speed ratio and turning angle as a function of water depth for wind speeds of 5, 15, and 25 m/s.
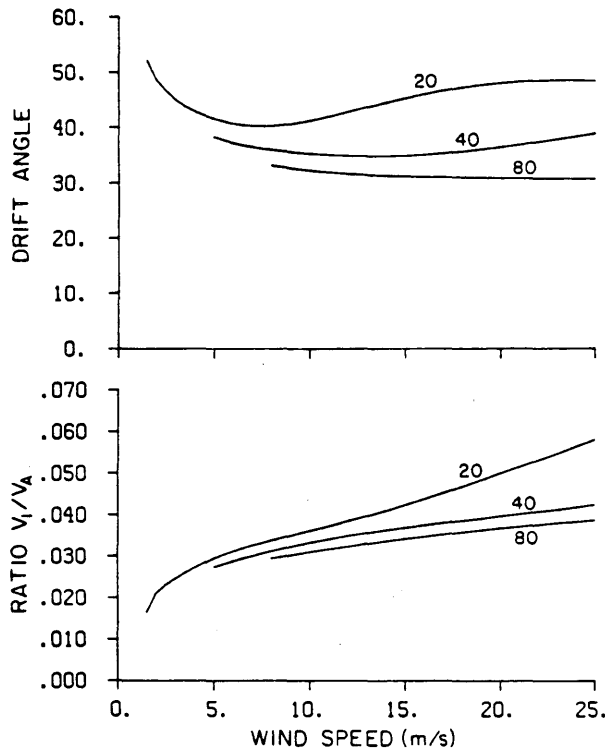
Fig. 2 The speed ratio and turning angles as function of wind speed for water depths of 20, 40, and 80 m.

ing for $\mathbf{V}_I = \mathbf{V}(z = H - z_w)$ until τ_w converged to within 0.1%. This typically took four to seven iterations.

Figures 1 and 2 plot the wind factor, V_I/V_A, and the drift angle α between $\mathbf{V}_I$ and $\mathbf{V}_A$ as a funtion of depth and wind speed for the constants given in Table 1. The value of C_a is representative of the inner marginal ice zone (MIZ) of the Bering Sea (Macklin, 1983). The ice/water roughness z_w is calculated from a value of C_w obtained from a

measured ratio of C_a to C_w. The ocean bottom roughness was inferred from observed tidal current profiles in the central Bering Sea shelf (Mofjeld and Lavelle, 1983).

Our solution approaches the dependence of wind factor V_I/V_A on wind speed for the deepwater limit (Reed and Campbell, 1962, Neralla et al., 1981; Pease and Overland, in prep.) and adds credibility to the boundary layer parameterizations used in those studies. The solution in Figure 1 shows little dependence on water depth for depths greater than 30 m. This is at first surprising since the Ekman solution (Ekman, 1905) has a local maximum of surface velocity for a value of $H/D = 0.3$, where D is the depth of frictional influence. If D, and thus the maximum eddy coefficient, is specified explicitly as a function of the ice/water shear stress:

$$D = 0.4(u_{*w}/f), \quad u_{*w}^2 \equiv (\tau_w/\varrho_o) \tag{14}$$

our solution will also give the behavior of an Ekman-type solution. However, in the second-order closure solution for a given τ_w, the magnitude of the mixing length and hence the eddy viscosity also decrease with decreasing water depth. This has the effect of keeping the H/D ratio large as the water depth decreases from 50 m to 20 m for wind speeds greater than 10 m/s.

The main coefficients in the model are the various drag coefficients and γ, which determines the maximum value of the mixing length in deep water (Table 2). The ratio of the air/ice drag coefficient to the ice/water drag coefficient, C_a/C_w, is a major parameter of the model rather than the individual coefficient values because the ice/water stress and air/ice stress are in approximate balance. There is significantly less scatter in obser-

Table 1. Values for a sample calculation typical of the Bering Sea in winter.

Air density	$\varrho_a = 1.30$ kg/m³
Ice density	$\varrho_I = 0.95 \times 10^3$ kg/m³
Water density	$\varrho_o = 1.026 \times 10^3$ kg/m³
Ice thickness	$h_I = 1$ m
Drag coefficient (air/ice)	$C_a = 3 \times 10^{-3}$ (at 10 m)
Drag coefficient (ice/water)	$C_w = 17.6 \times 10^{-3}$ (at -2 m)
Surface roughness computed from C_w	$z_w = 9.8 \times 10^{-2}$ m
Surface roughness (water/bottom)	$z_B = 1 \times 10^{-4}$ m
Coriolis parameter	$f = 1.26 \times 10^{-4}$ s⁻¹ (60° latitude)
Von Karman's constant	$k = 0.4$
Mixing length parameter*	$\gamma = 0.2$
Dissipation constant*	$c = 15$

* Mofjeld and Lavelle (1983).

51

Table 2. Sensitivity of model speed ratio (V_i/V_A) and veering angle (α) to the C_a/C_w ratio, γ, tidal mixing, and ice thickness. Standard case is for an ice thickness of 1 m and a wind velocity of 15 m/s.

	H = 20 m		H = 100 m	
	V_i/V_A	α (deg.)	V_i/V_A	α (deg.)
STD	0.042	45.2	0.033	30.1
$C_a/C_w \times 1.5$	0.045	43.0	0.036	28.4
$C_a/C_w \times 0.5$	0.040	48.4	0.030	32.73
$\gamma = 0.3$	0.040	45.6	0.032	28.2
$\gamma = 0.1$	0.049	44.8	0.038	34.8
W/Tides	0.041	45.1	0.034	30.2
$H_i = 0.5$ m	0.043	43.6	0.034	28.4
$H_i = 3.0$ m	0.039	50.9	0.032	36.7

vations of this ratio than in observations of either coefficients (Pease et al., 1983). The range of C_a/C_w ratio in Table 2 is greater than ± 2 standard deviations of the ratios given by Pease et al. (1983) for the Bering Sea and is within the range for Arctic Ocean values (McPhee, personal communication).

Another factor that may influence the results is that on most continental shelves there can be enhanced vertical mixing from tidal currents. This background turbulence may influence how the wind-driven solution couples to the bottom. The second-order closure model was run with specifying the bottom stress from the tidal velocity as 10^{-1} N m^{-2} and calculating the vertical profile of eddy viscosity; this value of tidal stress is typical of the rotary tide over the central Bering Sea Shelf near 60 °N and 168 °W. This profile of eddy viscosity was added to the viscosity calculated from the turbulent energy equation for the wind-driven case. The composite results in Table 2 show no significant tidal influence on the steady drift for the parameters given; there is some effect, particularly on angle, for water depths less than 20 m.

We have presented a solution for wind-driven ice drift in a shallow sea. The ocean is treated using second-order closure, and the ocean solution is directly coupled with the ice through the ice/water stress (Reed and Campbell, 1962). The second-order closure solution is an ideal way to resolve the ice/water boundary layer, bottom boundary layer, and the Ekman dynamics for a continuous range of water depths and wind speeds. Water depth has little influence on the solution for water depths greater than 30 m because the level of tur-

bulent mixing is a decreasing funtion of the total water depth.

This paper is a contribution to the Marine Services Project at PMEL and was supported in part by the Arctic Program of the Office of Naval Research.

REFERENCES

Ekman, V.W., On the influence of the earth's rotation on ocean currents, *Ark. f. Mat., Astron. och Fysik*, 2, 1-53, 1905.

Kinder, T.H., and J.D. Schumacher, Hydrographic structure over the continental shelf of the southeastern Bering Sea, in *The Eastern Bering Sea Shelf: Oceanography and Resources*, edited by D.W. Hood and J.A. Calder, *1*, pp. 31-52, Univ. of Wash. Press, Seattle, 1981.

Macklin, S.A., The wind drag coefficient over first-year sea ice in the Bering Sea, *J. Geophys. Res.*, 88, 2845-2852, 1983.

McPhee, M.G., Sea ice drag laws and simple boundary layer concepts, including application to rapid melting, USA Cold Regions Research and Engineering Laboratory, Hanover, boundary layer concepts, including application to rapid melting, USA Cold Regions Research and Engineering Laboratory, Hanover, N.H., CRREL Report 82-4, 1982.

Mellor, G.L., and T. Yamada, Development of a turbulent closure model for geophysical fluid problems, *Rev. Geophys. and Space Phys.*, 20, 851-875, 1982.

Mofjeld, H.O., and J.W. Lavelle, Setting the length scale in a second-order closure model of the bottom boundary layer, *J. Phys. Oceanogr.* in review, 1983.

Neralla, V.R., W.D. Liu, S. Venkatesh, and M.B. Danard, Techniques for predicting sea ice motion, in *Sea Ice Processes and Models*, edited by R.S. Pritchard, pp. 197-206, Univ. of Wash. Press, Seattle, 1981.

Neumann, G., *Ocean Currents*, Elsevier Publishing, Amsterdam, The Netherlands, 1968.

Pease, C.H., S.A. Salo, and J.E. Overland, Drag measurements for first-year sea ice over a shallow sea, *J. Geophys. Res.*, 88, 2853-2863, 1983.

Pease, C.H., and J.E. Overland, An atmospherically driven sea ice drift model for the Bering Sea, *Annals Glaciol.*, 5, in press, 1984.

Reed, R.J., and W.J. Campbell, The equilibrium drift of ice station Alpha, *J. Geophys. Res.*, 67, 281-297, 1962.

Shuleikin, V.V., The drift of ice-fields, *Compt.*

Rend. (Doklady) Acad. Sci. USSR, 19, 589–594, 1938.

Weatherly, G.L., and P.J. Martin, On the structure and dynamics of the oceanic bottom boundary layer, *J. Phys. Oceanogr. 8,* 557–570, 1978.

Marginal Ice Zone Modeling: Bering Sea Viewpoint

H.J. NIEBAUER AND V. ALEXANDER

Institute of Marine Science, University of Alaska, Fairbanks, Alaska 99701

High-latitude seas are often partially or season-ally covered with sea ice, either fixed to land mass-es (fast ice) or floating unattached (pack ice). The associated sea-ice edges are intensive oceanic frontal systems, since there are large horizontal density gradients in the surface layers caused by the change in phase of water from liquid to solid. Melting, freezing, and wind-driven water and ice in the marginal ice zone (MIZ) generate additional vertical and horizontal density gradients in sea-water (i.e. fronts). The purpose of this paper is to review briefly the modeling work on mesoscale (ca. kilometers and days) oceanographic processes in the MIZ and to compare the modeling results with the results of field studies. The observed and modeled physical features are also discussed rela-tive to observed ice-edge biological processes. Finally, some recent results of field studies in the Bering Sea are presented to motivate additional MIZ modeling work.

Efforts to model the mesoscale MIZ processes have only recently been initiated and reported. Gammelsrod et al. (1975) considered analytic linear, homogeneous, time-dependent and steady-state models of wind-driven upwelling near an ice edge. They found that in the steady-state mode the ice-covered region was similar to a coast. In time-dependent mode, friction (which was proportional to the velocity) determined a time scale of about 10 days for the onset of ice-edge upwelling.

Clarke (1978) considered an analytic linear model of quasi-geostrophic water motion near the sea ice edges. The ocean was stratified in 2 layers, with the sea ice thinner than the surface Ekman layer. Clarke found that the stationary ice sheet prevented the water beneath it from 'feeling' wind stress so that the boundary layer currents and up-welling were due to local forcing functions (i.e. the curl of the wind stress at the ice edge). He found the time and length scales for these phenomena to be on the order of 1 day and 10 km (the latter is the baroclinic Rossby radius of deformation).

Niebauer (1982) applied a cross-sectional, multilayer, time-dependent model to the MIZ in the eastern Bering Sea. The model results included ice-edge upwelling, baroclinic geostrophic flow, and inertial oscillations, with the emphasis placed on the driving forces of wind and low-density melt water. The time scales of all these phenomena were $1/f$ to 2 pi/f (2–12 hrs), where f = the Cor-iolis parameter. The space scale was the Rossby radius of deformation. Examples of the model output are shown in Figure 1. Figure 2 illustrates the phenomena of increased vertical density gra-dients due to less dense ice melt water at and under the ice edge in the upper 30 m and the associated frontal structure within 10 km of the ice edge (Alexander and Niebauer, 1981). The model hydrographic structure showing the melted ice water in the MIZ (Figure 1) is in at least qualitative agreement with these cross sections.

The oceanographic structure at the ice edge due to ice melt has marked effects on the biological regime in the MIZ. Marshall (1957) hypothesized that observed high primary productivity near the retreating Bering Sea MIZ in spring was due in part to low-salinity melt water increasing the stability of the water column, thus keeping phytoplankton from being vertically mixed out of the photic zone. Subsequent observations by McRoy and Goering (1974), Alexander and Cooney (1978), Niebauer et al. (1981), and Alexander and Niebauer (1981) support this hypothesis. Similar observations have been made in Antarctic waters (Hart, 1942; Ivanov, 1964; El Sayed and Taguchi, 1981).

The ice-edge frontal structure is also produced by ice-edge upwelling due to wind-driven Ekman transport (Buckley et al., 1979; Alexander and Niebauer, 1981; Johannessen et al., 1982). Alex-ander and Niebauer (1981), in reporting multiple occurrences of wind-driven ice-edge upwelling in the Bering Sea (Figure 2), suggested that the sur-facing of the isopleths that form the frontal struc-ture seaward of the ice edge is due, at least in part, to melting ice, but it is also due to surface diver-
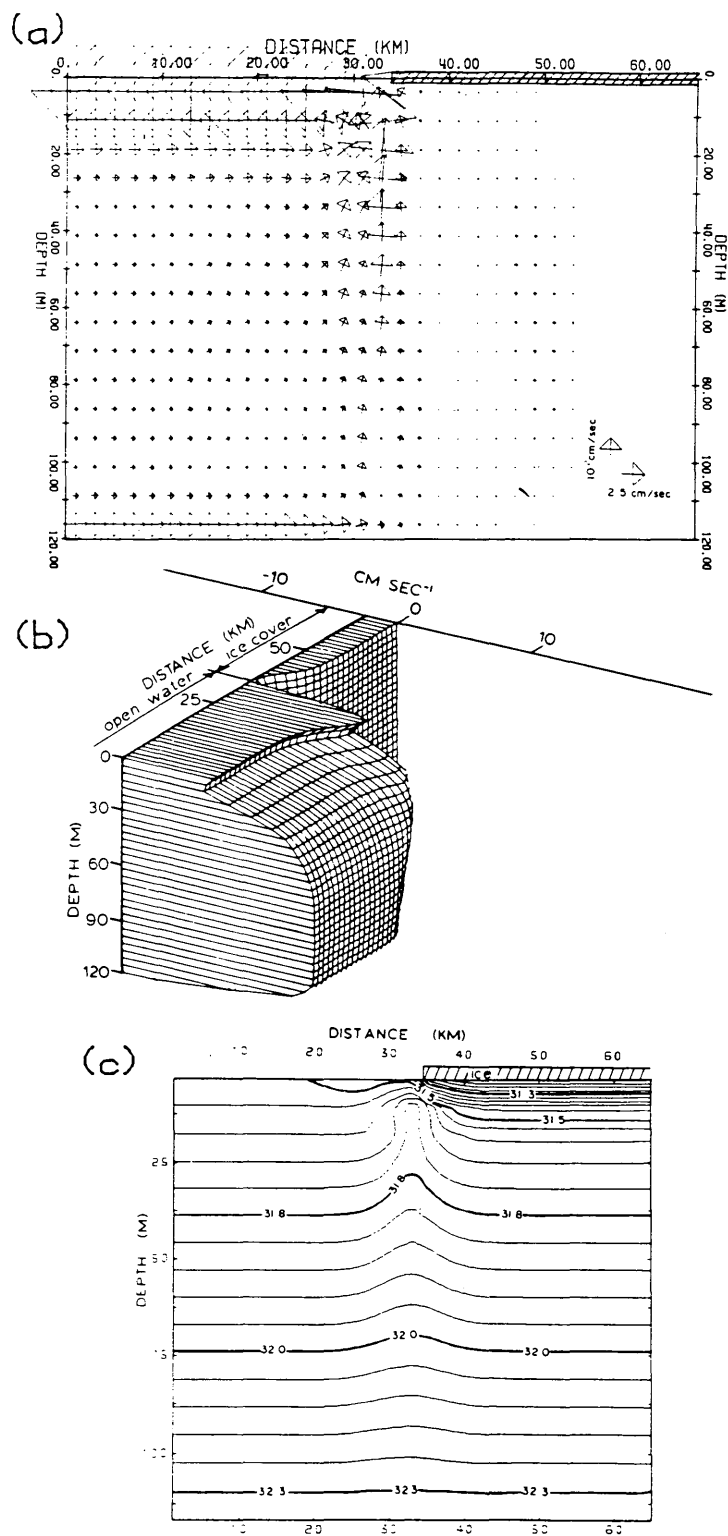
Fig. 1. Vertical and horizontal circulation perpendicular (a) and horizontal circulation parallel (b) to ice cover, and associated salinity structure (c) for a 1-dyne cm^{-2} wind stress applied to open water next to the ice edge. The wind is parallel to the ice edge. Data are shown 36 hours after wind stress is applied. (After Niebauer, 1982.)
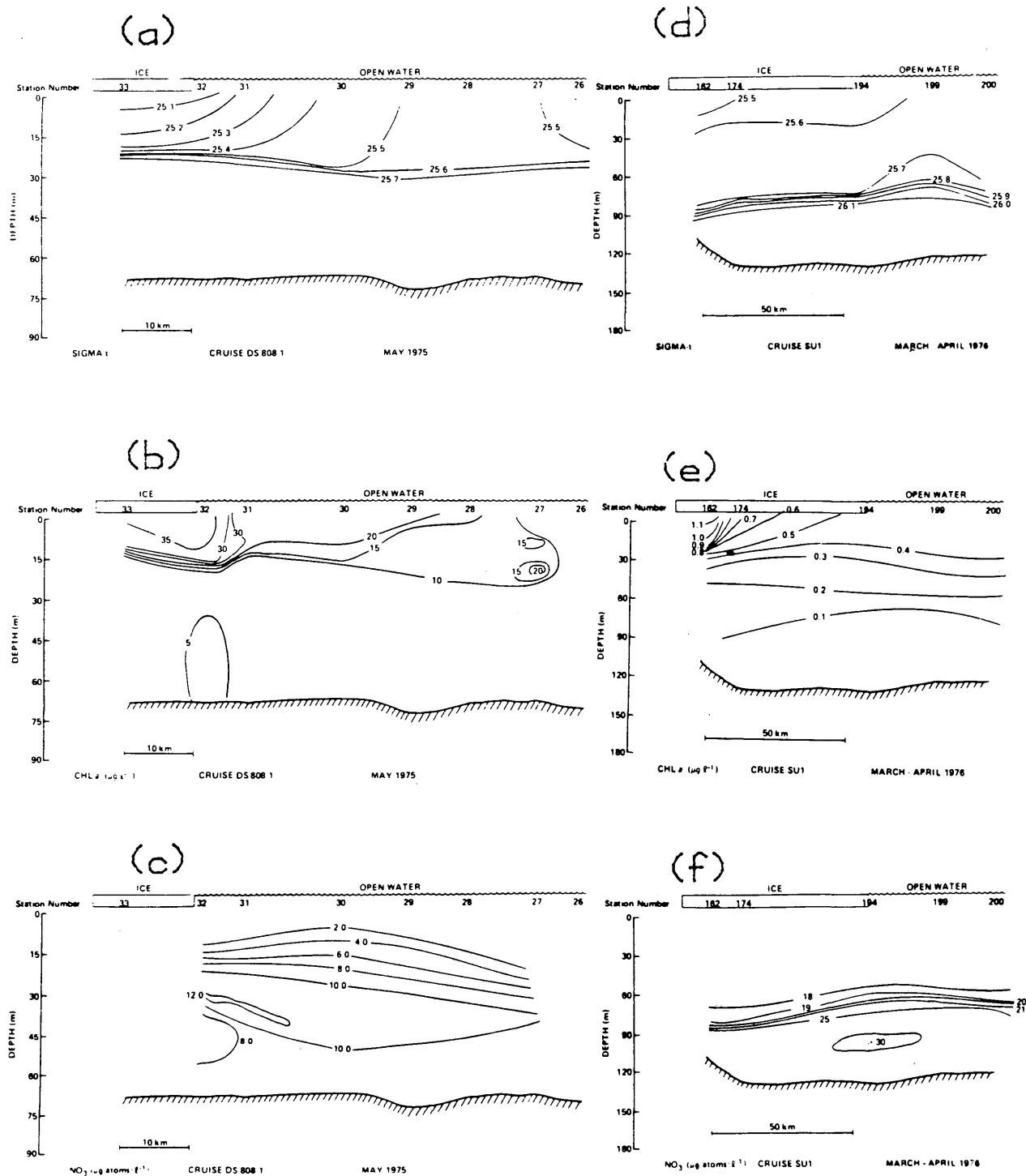
56

Fig. 2. Sigma-t (a, d), chlorophyll a (b, e), and nitrate (c, f) sections across the Bering Sea marginal ice zone in May 1975 and April 1976. Note difference in scales. (After Alexander and Niebauer, 1981.)

gence and upwelling at the ice edge caused by wind-driven off-ice Ekman transport. They further suggest that the hydrographic structure farther off-ice (i.e. doming of the isopleths from the surface to 30 to 80 m about 25 km seaward of the ice and, still farther off-ice, the decrease in water density with distance offshore) support the concept of ice-edge upwelling. Again, there is a qualitative agreement between the hypothesized wind-driven upwelling in the vicinity of Stations 27 to 30 in Figure 2a, Stations 194 to 200 in Figure 2d, and the model results in Figure 1.

57

Johannessen et al. (1982), in reporting ice-edge upwelling in the North Atlantic, suggested that it resulted from surface Ekman divergence at the lee edge of the pack ice as the pack ice was being driven into the main ice field. That is, the wind was blowing parallel to the ice edge with the ice to the *right* of the wind. The divergence was attributed to stronger coupling of wind to water via ice as compared with wind acting directly on water. Røed and O'Brien (1983) presented a MIZ model with a movable ice sheet. They found that, for winds blowing parallel to the ice edge with the main ice pack to the *right* of the wind, Ekman transport could cause convergence of the loose ice in the MIZ, with upwelling along the trailing edge of the moving loose ice similar to that observed by Johannessen et al. (1982). More recently, Røed (1983) has shown that the models are sensitive to parameters consisting of combinations of the drag coefficients used in the three air/ice/sea interfaces, such that upwelling or downwelling may occur, depending on the choice of parameters.

Regardless of the mode, ice-edge upwelling may increase the supply of nutrients to the ice-edge zone, resulting in an increase in primary production. For example, Alexander and Niebauer (1981) showed maxima in chlorophyll (Figure 2b) associated with the denser upwelling water (Figure 2a) 25 to 50 km off the ice edge. But Niebauer (1982) suggested that ice-edge upwelling is only half as effective in bringing deeper, nutrient-rich water into the photic zone as is upwelling along a solid coast. This conclusion resulted from a model study with a stationary ice cover, however, whereas McNutt (1981), for example, has shown that the pack ice over large portions of the eastern Bering Sea shelf can be moved about at speeds up to at least 0.5 m/s. On the other hand, results from Røed and O'Brien's (1983) model with movable ice also suggested that ice-edge upwelling is not nearly as efficient as coastal upwelling.

This less efficient upwelling process may be important in places like the Bering Sea shelf where the more nutrient-rich Bering Sea source water, which is warmer and more saline than the shelf water, is found at depths greater than 90 m (compare, for example, Figures 2c and 2f). Ice-edge upwelling may not be able to draw this water high enough in the water column to aid the primary production, given the observed duration of wind. In addition, Niebauer (1980) has shown large-scale fluctuations in the southern ice edge extent in the eastern Bering Sea that may have an important impact on ice edge productivity. In spring 1976, the ice extended to the shelf break out over the nutrient-rich water (e.g. Figure 3), while by spring 1979, the seasonal ice extent had retreated some 400–500 km northward so that the MIZ was over much shallower water. Upwelling over this shallow water may be less effective in increasing primary production because of decreased nutrients at depth.

Recently, Niebauer and Alexander (1983) have presented evidence of the interaction of frontal systems on the Bering Sea shelf. The frontal structure and stratification associated with the MIZ are not fixed in space because the MIZ is not fixed in space. In spring, as the ice melts, the MIZ as well as the associated melt-water-generated front and phytoplankton bloom move into shallower water. On the Bering Sea shelf, as on other of the world's shelves, there is a tidally driven front that forms on and is roughly fixed in space at about the 50-m isobath. We suggest that the front and the stratification associated with the melting ice collides with the hydrographic structure associated with the 50-m tidally driven front and closes the structure to form the dish-shaped hydrographic feature (stations 56–60 in Figure 4). This process generally has the result of stabilizing or maintaining the phytoplankton (chlorophyll) in the ice edge photic zone in the presence of a nutrient (nitrate) supply. But this process, which encourages the bloom, also limits it as the nitrate trapped in the stratification structure is used up and additional nitrate that could sustain the production is sealed off from the bloom at depth.

Cross-section observations taken several days apart showed some decrease in the amount of nitrate in the "dish" in Figure 4, but not enough to account for the much more widespread chlorophyll. The bloom seems to have tapped a nitrate source. We suggest that upwelling is occurring in the region of the 50-m front as a part of the frontal circulation, and nitrate-rich water is being forced laterally through the front into the "dish," supplying the bloom with additional nitrate and thus extending its life.

This leads to a discussion concerning the relation of ice-edge blooms to open-water spring blooms, and their relation to the overall primary production of the Bering Sea as well as other seasonally ice-covered, high-latitude seas. It must be pointed out that an ice-edge bloom is a spring bloom. Ice-edge blooms can usually be distinguished from the open-water shelf spring blooms by the physical method by which surface stratification (resulting in a reduction of surface mixing) occurs. In ice-edge blooms, low-salinity melt water accounts for the stratification (Alex-
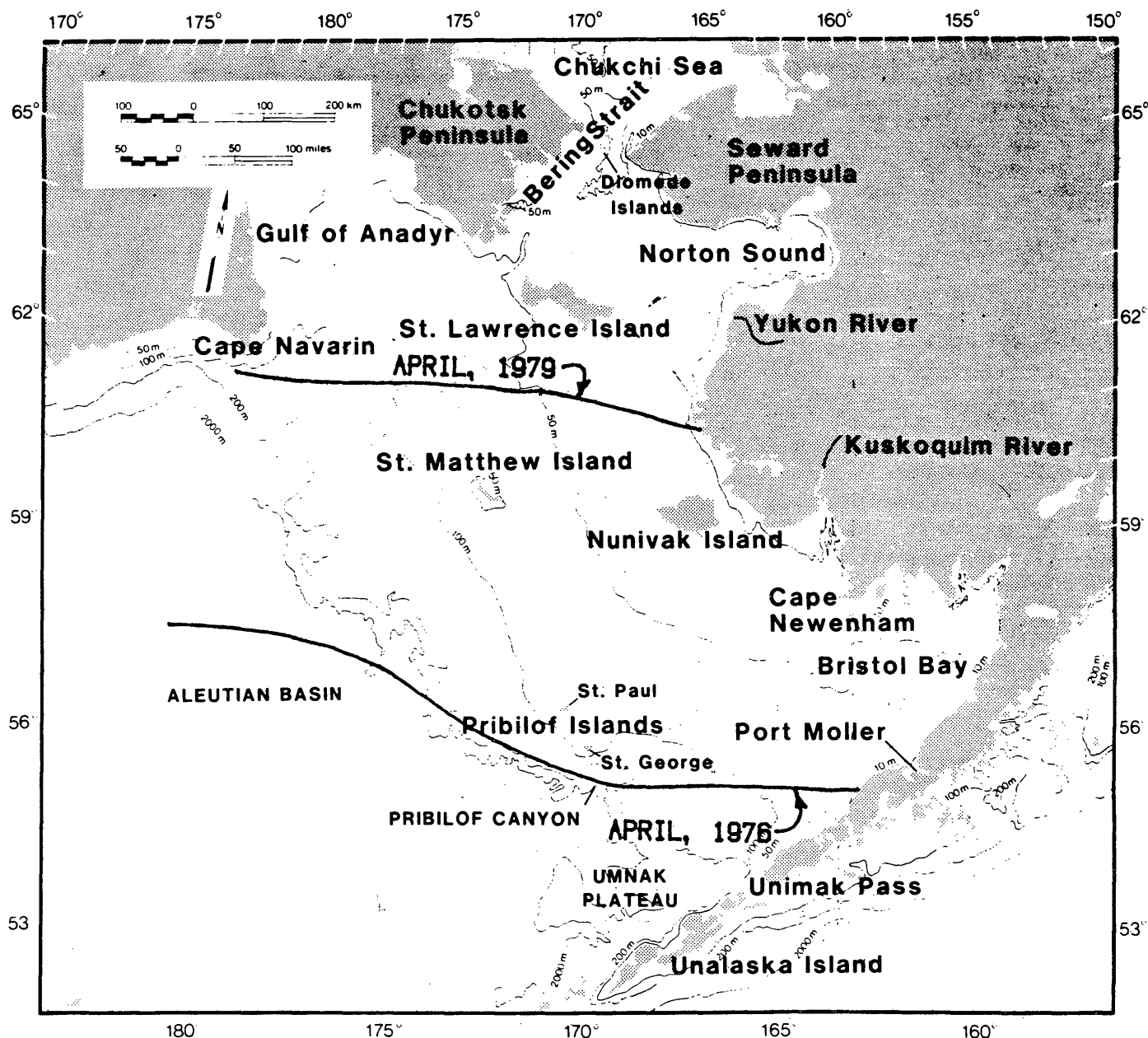
Fig. 3. The eastern Bering Sea showing the mean April ice edge position for 1976 and 1979.

ander and Niebauer, 1981), while in most open-water shelf blooms, surface heating accounts for the stratification (e.g. Sambrotto et al., 1983). Differences in assemblages of phytoplankton also allow differentiation (Schandelmeier and Alexander, 1981).

We know that both of these spring blooms occur and are important in the Bering Sea and certainly in other high-latitude seas. However, we do not know their relationship to one another in time, space, or magnitude in these areas, which are seasonally ice-covered; that is, in regions where the ice retreats in spring, the critical period in the

primary production cycle. For example, we speculate that an ice-edge bloom may at times preclude an open-water spring bloom because, as mentioned above, the melt-water stratification may prevent the vertical replenishment of nutrients to the photic zone. If increased spring insolation during and following the ice retreat reinforces the stratification, then the nutrients may be sealed off at depth until fall and winter, when storms and cooling break down the stratification. However, if, after the ice-edge bloom, there is some mechanism, such as wind mixing or upwelling in a shelf frontal system, that allows mixing of
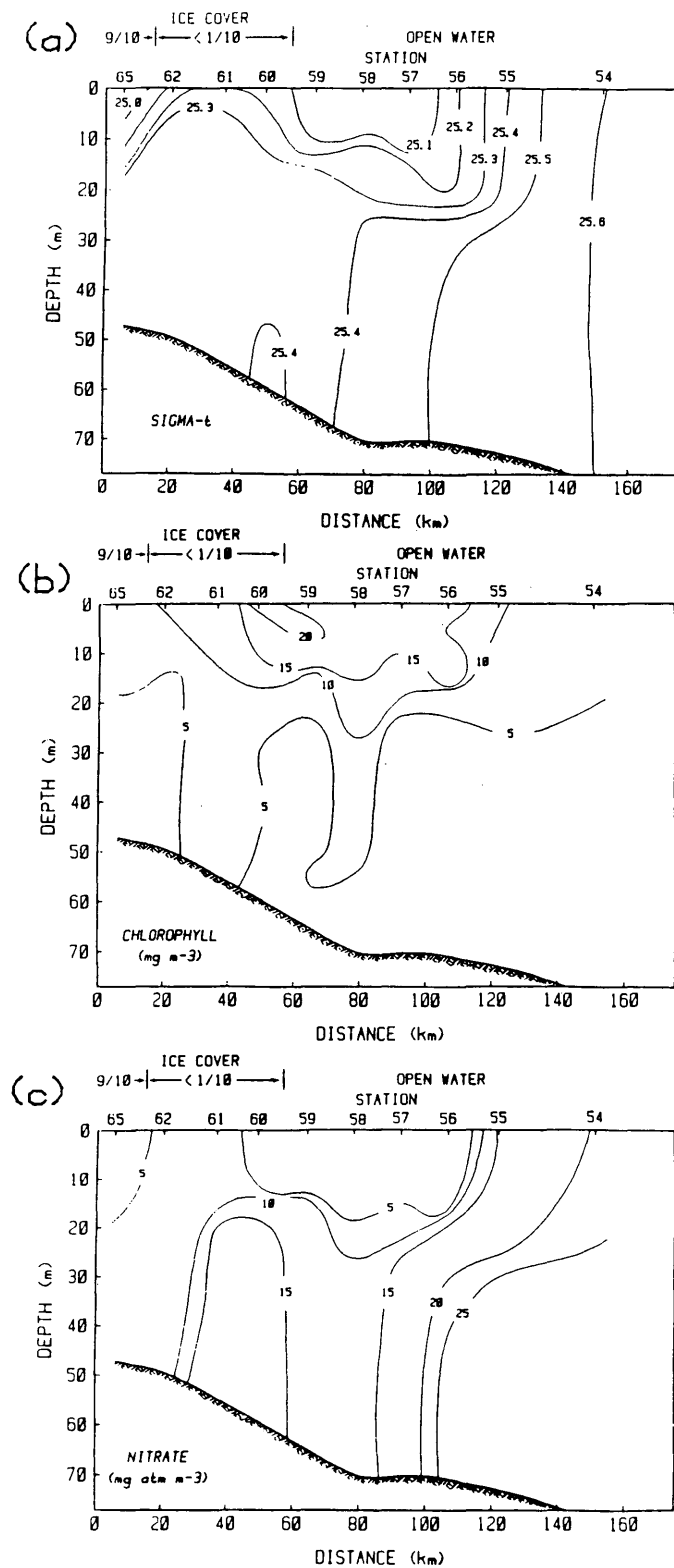
Fig. 4. Sigma-t (a), chlorophyll a (b), and nitrate (c) sections across the Bering Sea marginal ice zone in May 1982. (After Niebauer and Alexander, 1983.)

60

nutrients back into the photic zone followed by insolation-driven stratificatioin (or additional melt-water stratification), there can be an additional open-water spring bloom and an increase in the primary production. There appears to be enough nutrients at depth on the Bering Sea shelf to fuel blooms. The problem is to get the nutrients into the photic zone, above the stratification, where the phytoplankton can take it up.

To document this interaction in the field would and does take an enormous amount of resources due to the time and space scale of the phenomena, the variability of the high-latitude seas, and the required logistic support. Modeling provides a partial alternative to allow rapid and inexpensive testing of hypotheses that in turn should lead to more efficient field programs. Furthermore, to quote Walsh (1975), "The marine habitat is a geophysical fluid, and any attempts to understand biological processes therein must be firmly based in a matrix of relevant physical oceanography." The recent MIZ observations in the Bering Sea (Niebauer and Alexander, 1983) require an understanding of the open-shelf physical processes, the meteorological processes, the MIZ circulation processes, the biological processes, and, most importantly, their interaction. It is in this interactive mode, in trying to short out the role of the various physical and nonphysical processes, that models prove invaluable as research tools.

REFERENCES

Alexander, V., and R.T. Cooney, Bering Sea ice edge ecosystem study: Nutrient cycling and organic matter transfer, in *Annual Reports,* Environmental Assessment of the Alaskan Continental Shelf (OCS), 1978.

Alexander, V., and H.J. Niebauer, Oceanography of the eastern Bering Sea ice-edge in spring, *Limnol. Oceanogr., 26,* 1111-1125, 1981.

Buckley, J.R., T. Gammelsrod, J.A. Johannessen, O.M. Johannessen, and L.P. Røed, Upwelling: Oceanic structure at the edge of the Arctic pack ice in winter, *Science, 203,* 165-167, 1979.

Clarke, A.J., On wind-driven quasi-geostrophic water movements near fast ice edges, *Deep-Sea Res., 25,* 41-51, 1978.

El Sayed, S.Z., and S. Taguchi, Primary production and standing crop of phytoplankton along the ice edge in the Weddell Sea, *Deep-Sea Res.,*

28A, 1017-1032, 1981.

Gammelsrod, T., M. Mork, and L.P. Røed, Upwelling possibilities at an ice edge, homogeneous model, *Marine Sci. Comm., 1,* 115-145, 1975.

Hart, T.J., Phytoplankton periodicity in Antarctic surface waters, *Discovery Reports, 21,* 261-356, 1942.

Ivanov, A.I., Characteristics of the phytoplankton in Antarctic waters at the whaling grounds of the flotilla *Slava* in 1957-58, *Sov. Antarct. Exped. Inform. Bull., 1,* 394-396, 1964.

Johannessen, O.M., J.A. Johannessen, J. Morison, B.A. Farrelly, and E.A.S. Svendsen, NORSEX III: The mesoscale oceanographic conditions in the marginal ice zone north of Svalbard in early fall 1979, MS, 1982.

Marshall, P.T., Primary production in the Arctic, *J. Conseil, 23,* 173-177, 1957.

McNutt, S.L., Ice conditions in the eastern Bering Sea from NOAA and LANDSAT imagery: Winter conditions 1974, 1976, 1977, 1979, *Tech. Memo ERL PMEL-24,* NOAA, PMEL, Seattle, Wash., 1981.

McRoy, C.P., and J.J. Goering, The influence of ice on the primary productivity of the Bering Sea, in *Oceanography of the Bering Sea,* edited by D.W. Hood and E.J. Kelley, Univ. Alaska Inst. Mar. Sci., Occas. Publ. 2, 1974.

Niebauer, H.J., Sea ice and temperature fluctuations in the eastern Bering Sea and the relationship to meteorological fluctuations, *J. Geophys. Res., 85,* 7507-7515, 1980.

Niebauer, H.J., Wind- and melt-driven circulation in a marginal sea ice edge frontal system: A numerical model, *Cont. Shelf Res., 1,* 49-98, 1982.

Niebauer, H.J., and V. Alexander, On the influence of physical oceanographic processes on biological production in a marginal ice edge zone, submitted to *Cont. Shelf Res.,* 1983.

Niebauer, H.J., V. Alexander, and R.T. Cooney, Primary production at the eastern Bering Sea ice edge: The physical and biological regimes, in *The Eastern Bering Sea Shelf: Oceanography and Resources,* edited by D.W. Hood and J.A. Calder, 2, pp. 763-772, U.S. Dept. Commerce, 1981.

Røed, L.P., Sensitivity studies with a coupled ice-ocean model of the marginal ice zone, *J. Geophys. Res., 88,* 6039-6042, 1983.

Røed, L.P., and J.J. O'Brien, A coupled ice-ocean model of upwelling in the marginal zone, *J. Geophys. Res., 88,* 2863-2872, 1983.

Sambrotto, R.N., H.J. Niebauer, J.J. Goering, and R.L. Iverson, Vertical mixing and the development of the spring phytoplankton bloom of the

southeast Bering Sea middle shelf, to be submitted to *Cont. Shelf Res.*, 1983.

Schandelmeier, L., and V. Alexander, An analysis of the influence of ice on spring phytoplankton population structure in the southeast Bering Sea, *Limnol. Oceanogr., 26,* 935-943, 1981.

Walsh, J.J., A biological interface for numerical models and the real world—An elegy for E.J. Ferguson Wood, in *Numerical Models of Ocean Circulation,* pp. 5-8, National Academy of Sciences, 1975.

Variation of the Drag Coefficient
Across the Antarctic Marginal Ice Zone

E.L ANDREAS, W.B. TUCKER III AND S.F. ACKLEY
U.S. Army Cold Regions Research and Engineering Laboratory
Hanover, New Hampshire 03755

In October of 1981 the U.S.-U.S.S.R. Weddell Polynya Expedition (Gordon and Sarukhanyan, 1982) crossed the Antarctic marginal ice zone (MIZ) near the Greenwich Meridian on the Soviet icebreaker *Mikhail Somov*. During the traverse we launched a series of five radiosondes along a 150-km track starting at the ice edge. The wind was from the north, off the ocean, and these radiosonde profiles showed profound modification of the atmospheric boundary layer (ABL) as increasing surface roughness decelerated the flow. The primary manifestation was a lifting of the inversion layer by the induced vertical velocity as the distance from the ice edge increased. Using this raising of the inversion we were able to estimate the change in the neutral-stability drag coefficient, C_D, across the MIZ. C_D increased from its open ocean value, 1.2×10^{-3}, at the ice edge to 4×10^{-3} at 80-90% ice concentration. We present an equation for this dependence of the drag coefficient on ice concentration that should be useful for modeling the surface stress in marginal ice zones.

The juxtaposition of ice and water in polar seas can have dramatic effects on the ABL. Vowinckel and Taylor (1965) and Badgley (1966) first predicted the magnitude of the turbulent winter heat flux from open water to the atmosphere, but the ABL can also respond to a change in surface roughness. Although the changes in roughness may not be as obvious over the polar seas as they are over land or at coastlines (Panofsky and Petersen, 1972; Beljaars, 1982), the ice edge especially can present a significant roughness change. The drag coefficient—a measure of surface roughness—is very similar for the ocean (Large and Pond, 1981) and for smooth sea ice (Banke et al., 1980). But, based on measurements by Smith et al. (1970), Macklin (1983), and Banke et al. (1976, 1980), and on theoretical work by Arya (1975), a picture is emerging of how strongly the drag coefficient depends on surface topography. In the MIZ (Wadhams, 1981), where the ice is broken and dispersed by wave activity, the drag coefficient is probably larger than anywhere else over the ocean, since the surface is essentially a continuous field of step functions—ice to water, then back up to ice. The drag coefficient here may thus be as much as three times greater than it is over the ocean; this corresponds to a two-order-of-magnitude difference in the roughness length, z_0. An atmospheric flow crossing the ice edge consequently encounters a change in surface temperature as well as a change in surface roughness that is large enough to alter the ABL (Taylor, 1969; Peterson, 1969; Panofsky and Petersen, 1972; Vager and Nadezhina, 1975).

During our series of radiosonde launches, the wind was from the northwest, it had been steady in direction for the 12 hours before we encountered the ice edge (Figure 1). The sounding profiles (Figure 2) and our shipboard meteorological data thus provide the first comprehensive look at how surface roughness and temperature changes in the MIZ can affect the ABL.

With the on-ice winds, the atmospheric flow encountered an increase in surface roughness at the ice edge and consequently slowed (e.g., Taylor, 1959; Vager and Nadezhina, 1975). By virtue of two-dimensional continuity,

$$\partial U/\partial x + \partial W/\partial z = 0 \qquad (1)$$

where U is the mean horizontal wind velocity and so defines the x-axis, W is the mean vertical velocity, and z is positive upward, there must thus have been a positive vertical velocity over the ice. In other words, the entire ABL can be expected to rise downwind of the roughness change. This lifting is obvious in Figure 2, where the potential temperature profiles above the inversion remain virtu-
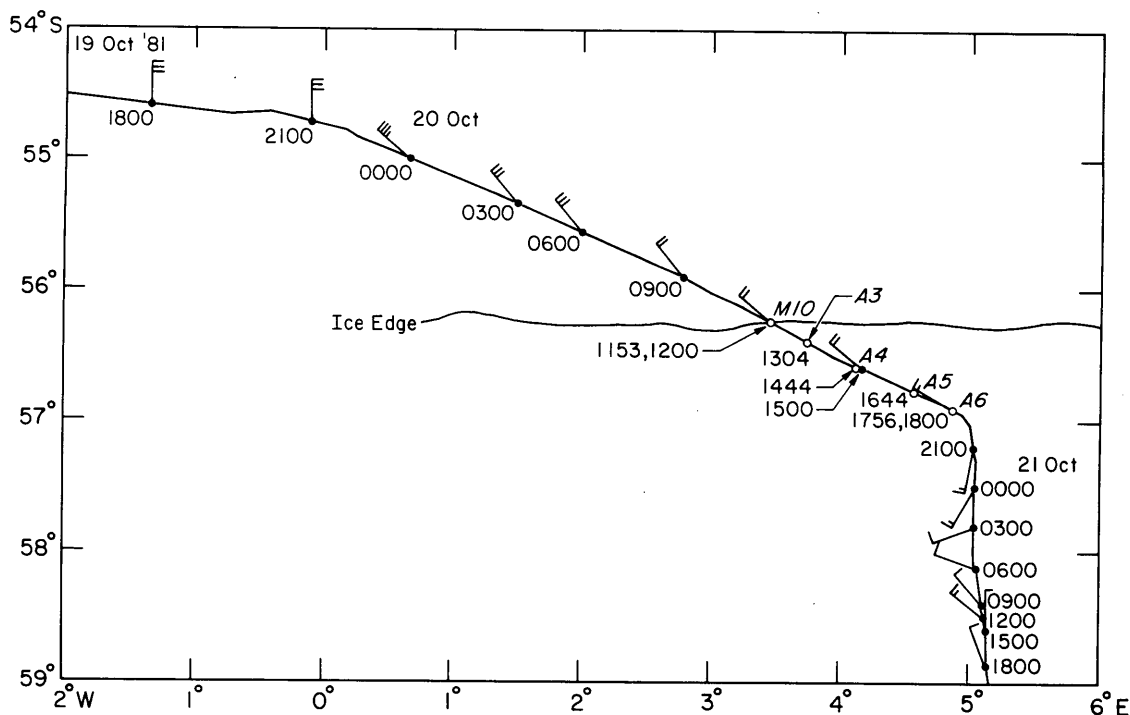
Fig. 1. The cruise track. The flags show observations of the surface wind vector, which were made every 3 hours as indicated. The open circles show locations of the upper-air soundings with the time noted.

ally unchanged from sounding to sounding, but rise with distance downwind from the ice edge. We will use this raising of the ABL to estimate the change in drag coefficient across the MIZ.

Table 1 summarizes the upper-air soundings that we made while crossing the MIZ. In the table the fetch is the actual distance the wind blew over the ice, not the distance perpendicular to the ice edge. The ice concentration c is the fraction of ice cover estimated from our visual observations (Ackley and Smith, 1983); T_s is the surface temperature; T_{11} is the air temperature at a height of 11 m measured by a sensor on the bow of the ship; U_{10} is the wind speed 10 m above the surface, measured on the ship's mast; and ϕ is the relative humidity.

We used two different radiosonde systems for the soundings. The M10 sounding was made with a MicroCORA system manufactured by Vaisala of Helsinki, Finland, and the other four with a Airsonde system manufactured by A.I.R. of Boulder, Colorado. Both systems measure pressure, temperature, and humidity. In addition, the MicroCORA measures the wind profile by using the Omega Navaid signals to track the radiosonde (Beukers, 1979). Andreas and Richter (1982) evaluated the performance of the two radiosonde systems that we used on the *Somov* and found that

they made comparable measurements of pressure and temperature. The interchangeability of temperature and pressure sensors between different sondes was pretty much as the manufacturers specify, ±0.2 °C for temperature and ±1 mb for pressure (Call and Morris, 1980). The accuracy of the Omega-derived winds in this part of the Antarctic is, nominally, 1 m/s (Olson, 1979).

As is evident from the wind flags in Figure 1, the wind direction was very steady during our radiosonde transect and for the 12 hours preceding it. At the ice edge at noon on 20 October the geostrophic wind was from 300°, and there was very little Ekman turning of the wind vector: only 11° between the surface and 2000 m. Andreas et al. (1984) discuss this wind profile and other evidence of the two-dimensional nature of the flow.

Ackley and Smith (1983) describe in detail the ice conditions that we encountered during our transect on 20 October. In brief, we saw the first small chunks of ice at 1115 GMT and crossed very diffuse plumes of small broken floes until the M10 sounding at 1153, when ice concentration was judged to be 10%. We continued to alternately cross open water and low-concentration plumes of brash ice and small broken floes until the A3 sounding at 1304. Now the plumes and bands became more concentrated and contained some
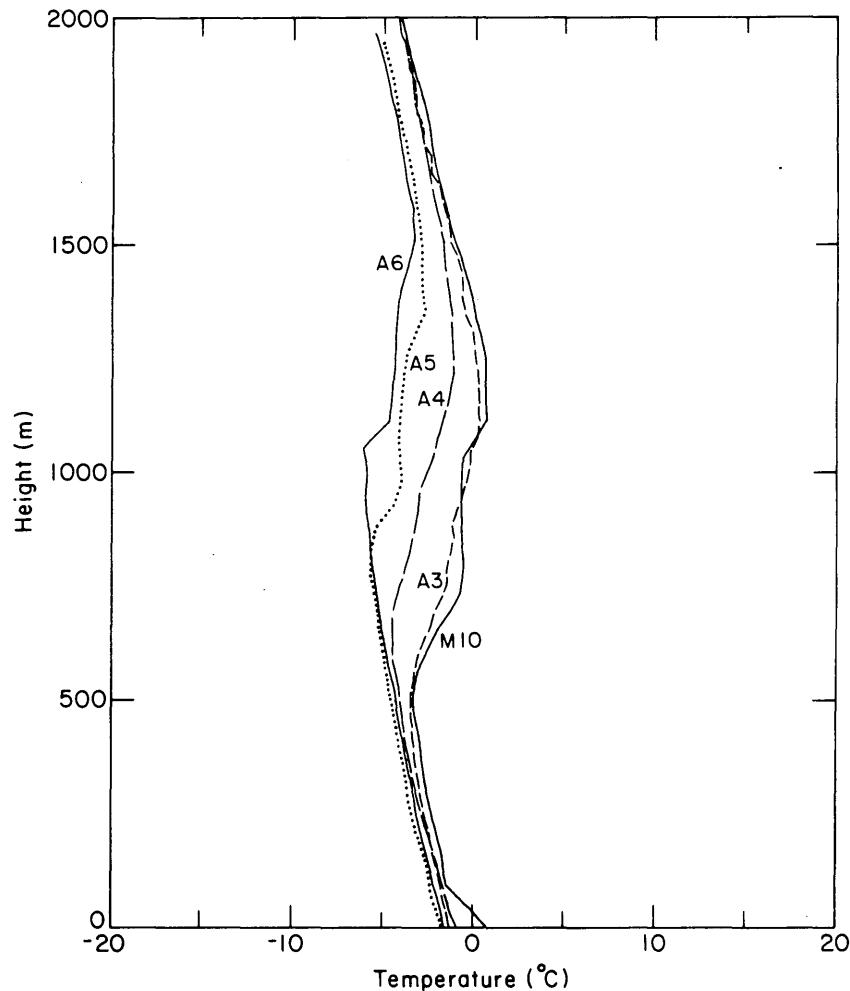
Fig. 2. Potential temperature profiles from the five soundings.

older ice with evidence of ridging; but there was still a lot of open water. Ice concentration for the A4 radiosonde at 1444 was 15%, and the floe size was approximately 5 m. Between the A4 and A5 soundings we evidently crossed a more stable ice edge; by the time of the A5 sounding at 1644 the concentration was 30%, the floes were older and sometimes ridged, and some were snow-covered. The banding of the floes continued as we penetrated the MIZ; at 1717 we crossed an extensive band of 5-m floes, and the ice coverage had increased to 40-60%. For the A6 soundings at 1756 we were in first-year ice of 80% concentration, floe diameters were 8-10 m, and there was brash ice between the floes. By 1815 the ice concentration was 90%, a value typical of the interior pack, but the floes were still only about 10 m in diameter. Compare this description of the Antarctic MIZ to that by Bauer and Martin (1980) of the Bering Sea MIZ, which seems to be much narrower and to be a result of somewhat different processes.

In Figure 3 we have contoured the potential temperature data shown in the profiles in Figure 2. We also plot in the figure and list in Table 1 the inversion height Z_i, the potential temperature at Z_i, θ_i, the height of the top of the inversion layer Z_{it} (where the potential temperature profiles in Figure 2 change slope a second time), and the potential temperature there θ_{it}.

Figure 3 gives a fairly complete picture of the modification of the ABL. The Z_{it} level rose with distance downwind but remained essentially coincident with the 14 °C potential temperature surface. The Z_i level also rose but, in contrast to Z_{it}, crossed isentropic surfaces: the inversion base was being eroded by mixing processes. Nevertheless, the slope of the inversion layer, $(\theta_{it} - \theta_i)/(Z_{it} - Z_i)$, remained constant at 0.017 °C/m from the ice edge to 150 km. That is, above the inversion base the structure of the air mass did not change over the 150-km path; potential temperature is a conservative tracer.
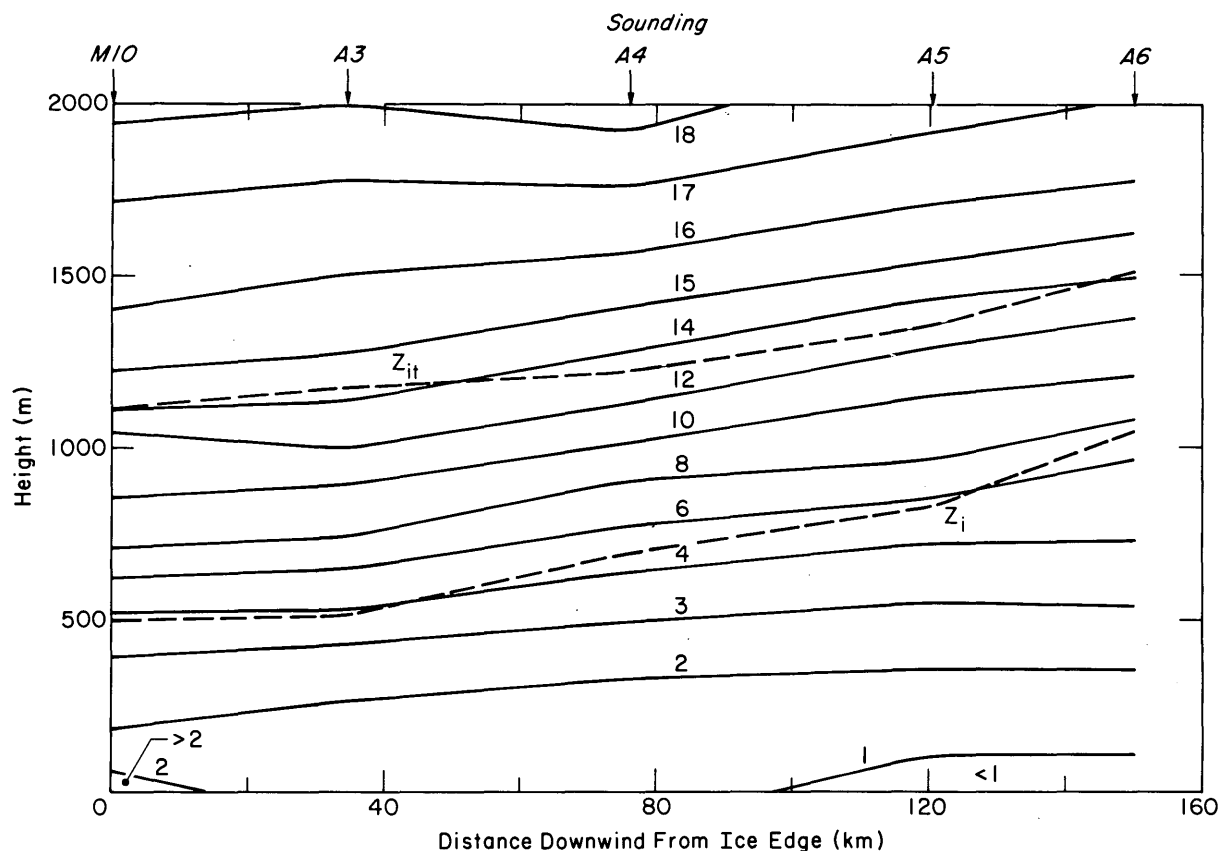
65

Fig. 3. Contours of potential temperature in °C along the ship track. Z_i indicates the height of the inversion, and Z_{it} shows the top of the inversion layer.

Our interpretation of Figure 3 necessarily means that the entire air column rose in response to the increased surface roughness. From the entries in Table 1 we can approximate the vertical velocity as (1513–1113 m)/6 h ≈ 2 cm/s. As we have already explained, this vertical velocity was merely a consequence of mass continuity; as the horizontal flow was decelerated by the increased roughness of the ice, there must have been a compensating increase in vertical velocity. We can therefore also approximate the vertical velocity from (1) and the wind speeds listed in Table 1:

$$\Delta W \approx -\Delta z (\Delta U / \Delta x). \tag{2}$$

With $\Delta U = -2$ m/s, $\Delta x = 150$ km, and $\Delta z = 1500$ m, again $W \approx 2$ cm/s at Z_{it}. We conclude that our data are consistent and that our conceptual picture of the ABL modification is accurate.

Since the lifting of the inversion layer results from the flow deceleration due to the increased roughness and surface stress, it seems conceivable that we can estimate the drag coefficient in the MIZ from the rate of increase of Z_i.

Taylor (1969) and Vager and Nadezhina (1975) have made numerical studies of an ABL perturbed by a change in surface roughness, but there is no analytical framework specifically for the study of ABL modification. We therefore base our evaluation of the MIZ drag coefficient on ABL similarity theory such as that developed by Zilitinkevich (1972, 1975). A fundamental assumption of the theory is horizontal homogeneity, which is certainly absent in the MIZ, but the precedent for using such a procedure is well established: early analytic studies of horizontal nonhomogeneity in the atmospheric surface layer have yielded useful results despite being based on relations derived for horizontally homogeneous conditions (e.g, Calder, 1949; Sutton, 1953; Elliot, 1958; Philip, 1959; Panofsky and Townsend, 1964; Townsend, 1965; Taylor, 1970).

Fortunately, for the scales with which we are concerned, the ABL over the MIZ seems to have been in quasi-equilibrium with the surface, so similarity theory may be more valid than it at first appears. Consider a horizontal scale characterizing the rate at which the ABL responds to a new sur-

66

Table 1. Summary of the marginal ice zone upper-air soundings. All were made on 20 October 1981.

	Sounding				
	M10	A3	A4	A5	A6
Time*	1153	1304	1444	1644	1756
Lat. (°S)	56.2	56.4	56.6	56.8	56.9
Long. (°E)	3.3	3.7	4.1	4.6	4.9
Fetch (km)	0	35	76	120	150
c	0.10†	0.10	0.15	0.30	0.80
T_s (°C)	-1.3	-1.4	-1.4	-1.6	-1.7
T_{11} (°C)	0.8	-1.3	-0.9	-1.7	-1.6
U_{10} (m/s)	9.5	8.9	8.4	7.9	7.4
ϕ (%)	91	90	88	93	98
Z_i (m)	491	511	694	827	1050
θ_i (°C)	3.5	3.7	4.6	4.9	6.4
Z_{ii} (m)	1113	1169	1219	1351	1513
θ_{ii} (°C)	14.1	14.3	13.4	13.4	14.3

* Since we were near the 0° meridian, all times are both Greenwich Mean Time (GMT) and local time.

† Although we specify c as 0.1 for this sounding, that value is really not appropriate for the radiosonde profile. We made this sounding virtually at the ice edge; with on-ice winds the air mass was, thus, representative of open ocean conditions—i.e., of $c = 0$.

face, such as $D_{mod} = Z_i/(\partial Z_i/\partial x)$, which is roughly (800 m)/(560 m/150 km) = 210 km. On the other hand, we can form a distance scale representative of the turbulent processes in the ABL from the boundary-layer time scale Z_i/u_*, and the mean wind speed $\bar{U}$, $D_{turb} = \bar{U}Z_i/u_*$, where u_* is the friction velocity. This scale is interpreted simply as the distance an eddy is advected downwind while making one cycle of the boundary layer. We approximate D_{turb} as (15 m/s)(800 m/0.32 m/s) = 38 km. Thus, there is a much shorter distance scale for turbulence, which similarity theory models, than there is for characterizing the gross changes in the ABL. Evidently, turbulence parameters in the MIZ can respond rapidly enough to be in quasi-equilibrium with the surface despite its non-homogeneity.

Zilitinkevich (1975) predicted the height of a fully developed ABL in stable stratification (see Figure 2):

$$h_i = \alpha \left| \frac{u_*^2}{\frac{g}{\bar{T}} \frac{H_s f}{\varrho_0 c_p}} \right|^{1/2} \tag{3}$$

where α is a constant, which Zilitinkevich (1975) took as one; $\bar{T}$ is a temperature typical of the layer; f is the Coriolis parameter; g is the acceleration of gravity; H_s is the surface sensible heat flux; ϱ_0 is the air density; and c_p is the specific heat of air at constant pressure.

Equation (3) has been verified with different values of α: Businger and Arya (1974) found $\alpha = 1.1$; Brost and Wyngaard (1978), $\alpha = 0.63$; and Brown (1981), $\alpha = 2.0$. Businger and Arya (1974) found that (3) is true for $u_*/|f|L > 20$: that is, for the Obukhov length $L < 130$ m in our study. Because of the surface inhomogeneity in the MIZ, however, it is hard to know whether the Obukhov length L has any physical significance. But Irwin and Binkowski (1981) showed how L is related to the local gradient Richardson number, Ri, which we can easily compute from our data. Converting L to Ri using their method, we find that (3) is true for our data when $Ri > 0.1$, a criterion that all of our soundings meet for heights above 200 m. Equation (3) therefore seems applicable here.

We will assume that h_i corresponds to the inversion height Z_i and will use (3) to relate the expected increase in surface stress u_*^2 to the increase in Z_i. Andreas et al. (1984) have shown that H_s was fairly constant during our radiosonde transect; consequently, (3) simplifies to

$$Z_i(x) \propto u_*(x)^2. \tag{4}$$

The 10-m drag coefficient is defined by

$$C_D = (u_*/U_{10})^2, \tag{5}$$

where the wind speed at 10 m, U_{10}, is listed in Table 1. We know fairly well the value of the drag

coefficient for neutral stability at the ice edge, $C_D(x=0) \equiv C_{DO} = [u_*(0)/U_{10}(0)]^2$; it was the open ocean value 1.2×10^{-3} (Large and Pond, 1981). The relative change in the drag coefficient across the MIZ is thus

$$C_D(x)/C_{DO} = [u_*(x)/u_*(0)]^2 \cdot [U_{10}(0)/U_{10}(x)]^2. \qquad (6)$$

With our measurements of U_{10}, and evaluating $u_*(x)/u_*(0)$ from (4),

$$C_D(x)/C_{DO} = [Z_i(x)/Z_i(0)] \cdot [U_{10}(0)/U_{10}(x)]^2, \qquad (7)$$

where $Z_i(0)$ is the inversion height from the M10 sounding, a value that should represent the horizontally homogeneous conditions of the upwind ocean. The beauty of (7) is that it involves only ratios of the measured quantities. Hence, uncertainty over the value of the constant in (3) does not affect it, and possible fetch-dependent stability effects or systematic errors in our determination of U_{10} are of minor consequence. C_D/C_{DO} is thus, in essence, the ratio of drag coefficients for neutral stability.

Figure 4 shows a plot of C_D/C_{DO} as a function of fetch for our data. The line, obtained from a least-squares fitting of $\ln(C_D/C_{DO})$ vs X, is

$$C_D/C_{DO} = e^{0.008X}. \qquad (8)$$

Remember that X is not the perpendicular distance into the MIZ. The equation

$$C_D/C_{DO} = e^{0.004d}, \qquad (9)$$

with d in kilometers describes the behavior of C_D/C_{DO} as a function of actual distance from the ice edge.

Figure 4 suggests that values of C_D in the MIZ can be more than three times larger than open ocean values: with $C_{DO} = 1.2 \times 10^{-3}$, C_D can be 4×10^{-3}. Such values are not without corroboration. Macklin (1983) reported an average C_D value of $3.09 \pm 0.49 \times 10^{-3}$ in the Bering Sea MIZ for close but heavily fractured and ridged ice. Smith et al. (1970) measured C_D values as large as 4×10^{-3} in 80-90% ice cover in the Gulf of St. Lawrence. In contrast, the roughest ice that Banke et al. (1980) sampled in the close Arctic pack had a drag coefficient of 2×10^{-3}.

Equation (8) [or (9)] is not a very useful predictive tool, however, because the composition of the MIZ—its compactness and the distribution of ice types within it—can undergo significant temporal changes (Bauer and Martin, 1980). The distance from the ice edge may thus not be a very meaningful model parameter. Ice concentration c is more useful. Equation (8) does help us smooth out some of the variability in our particular data set, however. In Figure 5 we plot our raw C_D/C_{DO} data and the corresponding points obtained from
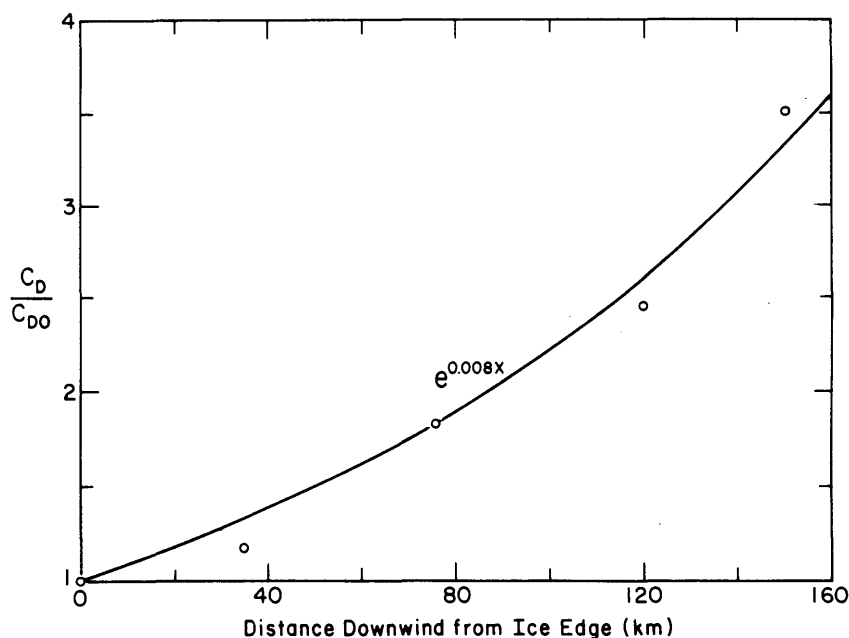

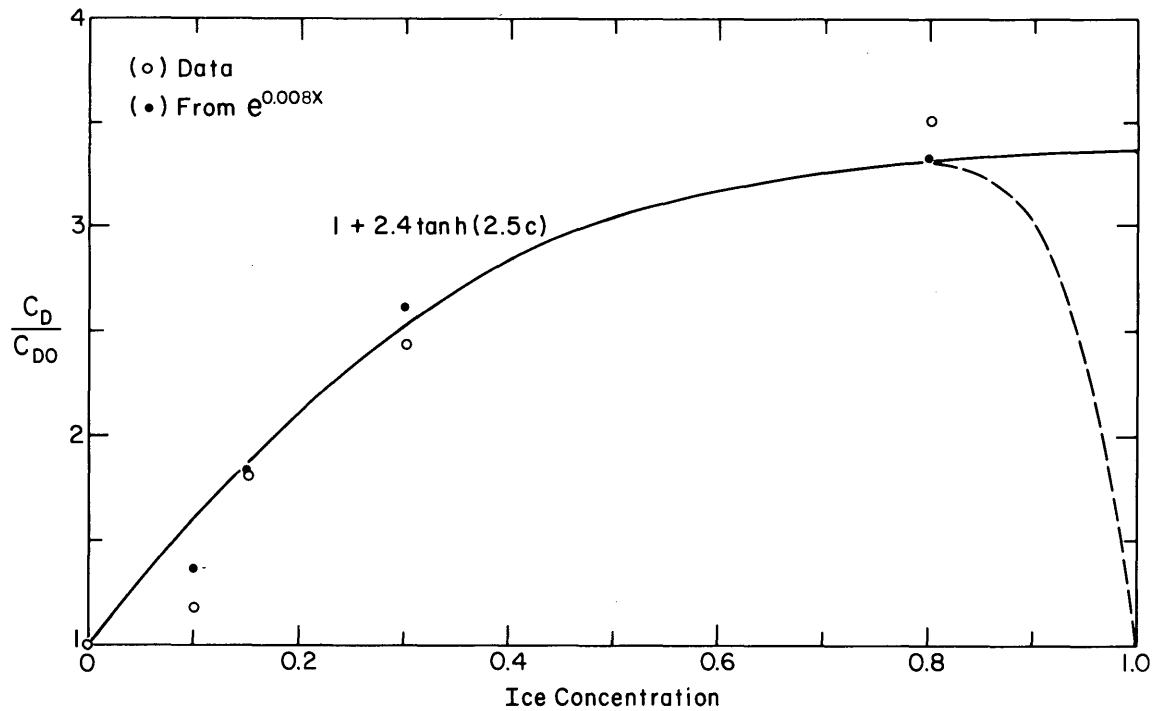Fig. 4. The relative change in drag coefficient across the MIZ.

68

Fig. 5. Raw and smoothed C_D/C_{DO} *ratios as a function of ice concentration. The dashed line suggests how we believe the ratio behaves for nearly complete ice cover.*

(8) vs c. The line, which we fitted by trial-and-error and intuition, is

$$C_D/C_{DO} = 1 + 2.4\tanh(2.5c),\ 0 \le c \le 1. \quad (10)$$

The values this predicts correspond well with the C_D values measured by Smith et al. (1970) in 80-90% ice concentration.

The tan$h$ function increases monotonically with its argument, so (10) predicts that $C_D = 3.4C_{DO}$ ($= 4.1 \times 10^{-3}$ if $C_{DO} = 1.2 \times 10^{-3}$) for total ice cover. Such a large value is incompatible with the measurements of Banke et al. (1980); they showed that over smooth, continuous sea ice C_D has virtually the same value that it has over the ocean, 1.1–1.2×10^{-3}. As the surface roughness of the interior pack increases, C_D also increases, but evidently not to values as large as 4×10^{-3}. Consequently, we suggest with the dashed line in Figure 5 that C_D/C_{DO} must rapidly return to the smooth ice value—one—as the ice concentration increases from 80% to 100%. Wind tunnel studies summarized by Rouse (1965) showed essentially this same effect; the aerodynamic surface roughness goes through a midrange maximum as the concentration of roughness elements increases from 0.0 to 1.0. For nearly complete ice cover, we therefore hypothesize that the relations parameterizing C_D as a function of surface roughness presented by Banke et al. (1980) replace (10).

Bauer and Martin (1980) speculated that the banding of ice that is common near ice edges (Muench and Charnell, 1977) is a result of the variation in drag coefficient across the MIZ. More recently, Wadhams (1983) suggested that the change in drag coefficient merely leads to divergence of the ice in the MIZ; then other processes, such as wave radiation pressure (Wadhams, 1983; Martin et al., 1983) or the reduction in water drag caused by melting (McPhee, 1983), act to form and accelerate the bands. By showing just how much the drag coefficient can change across the MIZ, our results explain the ice divergence due to off-ice winds that is the first step in band formation.

The data that we have presented give a fairly complete picture of how a stably stratified atmospheric boundary layer (ABL) is modified by an increase in surface roughness. The essential process in the modification is a deceleration of the air flow because of increased surface stress. The induced vertical velocity then lifts the entire ABL. The mixed layer below the inversion cools by losing heat to the surface, but temperature changes above the inversion are purely adiabatic.

Our radiosonde observations of the height of the inversion let us make the first determination ever of the drag coefficient over the broken floes that are characteristic of the Antarctic MIZ. We found that C_D for neutral stability can be as great as 4×10^{-3}, but depends strongly on ice concen-

tration. We have thus presented the first parameterization of the drag coefficient in terms of ice concentration (eq 10), an important relation for use in modeling surface stress in marginal ice zones.

REFERENCES

Ackley, S.F., and S.J. Smith, Reports of the U.S.-U.S.S.R. Weddell Polynya Expedition, October–November 1981: Volume 5, Sea ice observations, Special Report 83-2, U.S. Army Cold Regions Research and Engineering Laboratory, Hanover, N.H., 1983.

Andreas, E.L., and W.A. Richter, An evaluation of Vaisala's MicroCORA Automatic Sounding System, CRREL Report 82-28, U.S. Army Cold Regions Research and Engineering Laboratory, Hanover, N.H., 1982.

Andreas, E.L., W.B. Tucker, III, and S.F. Ackley, Atmospheric boundary-layer modification, drag coefficient, and surface heat flux in the Antarctic marginal ice zone, J. Geophys. Res., 89, 649–661, 1984.

Arya, S.P.S., A drag partition theory for determining the large-scale roughness parameter and wind stress on the Arctic pack ice. J. Geophys. Res., 80, 3447–3454, 1975.

Badgley, F.I., Heat budget at the surface of the Arctic Ocean, in Proceedings of the Symposium on the Arctic Heat Budget and Atmospheric Circulation, edited by J.O. Fletcher, pp. 267–277, Rand Corporation, Santa Monica, Calif., Rep. RM-5233-NSF, 1966.

Banke, E.G., S.D. Smith, and R.J. Anderson, Recent measurements of wind stress on Arctic sea ice, J. Fish. Res. Board Canada, 33, 2307–2317, 1976.

Banke, E.G., S.D. Smith, and R.J. Anderson, Drag coefficients at AIDJEX from sonic anemometer measurements, in Sea Ice Processes and Models, edited by R.S. Pritchard, pp. 430–442, Univ. of Wash. Press, Seattle, 1980.

Bauer, J., and S. Martin, Field observations of the Bering Sea ice edge properties during March 1979, Mon. Weather Rev., 108, 2045–2056, 1980.

Beljaars, A.C.M., The derivation of fluxes from profiles in perturbed areas, Bound. Layer Meteorol., 24, 35–55, 1982.

Beukers, J.M., The use of Loran and VLF navaids for windfinding, Atmos. Technol., 10, 3–13, 1979.

Brost, R.A., and J.C. Wyngaard, A model study of the stably stratified planetary boundary layer, J. Atmos. Sci., 35, 1427–1440, 1978.

Brown, R.A., Modeling the geostrophic drag coefficient for AIDJEX, J. Geophys. Res., 86, 1989–1994, 1981.

Businger, J.A., and S.P.S. Arya, Height of the mixed layer in the stably stratified planetary boundary layer, in Advances in Geophysics, edited by F.N. Frenkiel and R.E. Munn, vol. 18A, pp. 73–92, Academic Press, New York, 1974.

Calder, K.L., Eddy diffusion and evaporation in flow over aerodynamically smooth and rough surfaces: a treatment based on laboratory laws of turbulent flow with special reference to conditions in the lower atmosphere, Quart. J. Mech. Appl. Math., 2, 153–176, 1949.

Call, D.B., and A.L. Morris, The Airsonde System, in The Boulder Low-Level Intercomparison Experiment, edited by J.C. Kaimal, H.W. Baynton, and J.E. Gaynor, Rep. 2, pp.108–116, NOAA/ERL Wave Propagation Laboratory, Boulder, Colo., 1980.

Elliott, W.P., The growth of the atmospheric internal boundary layer, Trans. Am. Geophys. Union, 39, 1048–1054, 1958.

Gordon, A.L., and E.I. Sarukhanyan, American and Soviet expedition into the Southern Ocean sea ice in October and November 1981, Eos Trans. Am Geophys. Union, 63, 2, 1982.

Irwin, J.S., and F.S. Binkowski, Estimation of the Monin–Obukhov scaling length using on-site instrumentation, Atmos. Environ., 15, 1091–1094, 1981.

Large, W.G., and S. Pond, Open ocean momentum flux measurements in moderate to strong winds, J. Phys. Oceanogr., 11, 324–336, 1981.

Macklin, S.A., Wind drag coefficient over first-year sea ice in the Bering Sea, J. Geophys. Res., 88, 2845–2852, 1983.

Martin, S., P. Kauffman, and C. Parkinson, The movement and decay of ice edge bands in the winter Bering Sea, J. Geophys. Res., 88, 2803–2812, 1983.

McPhee, M.G., Turbulent heat and momentum transfer in the oceanic boundary layer under melt-

ing pack ice, *J. Geophys. Res., 88,* 2827–2835, 1983.

Muench, R.D., and R.L. Charnell, Observations of the medium-scale features along the seasonal ice edge in the Bering Sea, *J. Phys. Oceanogr., 7,* 602–606, 1977.

Olson, M.L., Global accuracy of Omega-derived winds, *Atmos. Technol., 10,* 14–23, 1979.

Panofsky, H.A., and E.L. Petersen, Wind profiles and change of terrain roughness at Risø, *Quart. J. Roy. Meteorol. Soc., 98,* 845–854, 1972.

Panofsky, H.A., and A.A. Townsend, Change of terrain roughness and the wind profile, *Quart. J. Roy. Meteorol. Soc., 90,* 147–155, 1964.

Peterson, E.W., Modification of mean flow and turbulent energy by a change in surface roughness under conditions of neutral stability, *Quart. J. Roy. Meteorol. Soc., 95,* 561–575, 1969.

Philip, J.R., The theory of local advection: I, *J. Meteorol., 16,* 535–547, 1959.

Rouse, H., Critical analysis of open-channel resistance, *J. Hydraul. Div., Am. Soc. Civ. Engrs., 91,* 1–25, 1965.

Smith, S.D., E.G. Banke, and O.M. Johannessen, Wind stress and turbulence in the Gulf of St. Lawrence, *J. Geophys. Res., 75,* 2803–2812, 1970.

Sutton, O.G., *Micrometeorology,* 333 pp., McGraw-Hill, New York, 1953.

Taylor, P.A., The planetary boundary layer above a change in surface roughness, *J. Atmos. Sci., 26,* 432–440, 1969.

Taylor, P.A., A model of airflow above changes in surface heat flux, temperature and roughness for neutral and unstable conditions, *Bound. Layer Meteorol., 1,* 18–39, 1970.

Townsend, A.A., Self-preserving flow inside a turbulent boundary layer, *J. Fluid Mech., 22,* 773–797, 1965.

Vager, B.G., and Ye.D. Nadezhina, The structure of the atmospheric boundary layer under horizontally inhomogeneous conditions, *Izv., Atmos. Oceanic Phys., 11,* 349–353, 1975.

Vowinckel, E., and B. Taylor, Energy balance of the Arctic: IV. Evaporation and sensible heat flux over the Arctic Ocean, *Arch. Meteorol. Geophys. Bioklimatol., B14,* 36–52, 1965.

Wadhams, P., The ice cover in the Greenland and Norwegian Seas, *Rev. Geophys. Space Phys., 19,* 345–393, 1981.

Wadhams, P., A mechanism for the formation of ice edge bands, *J. Geophys. Res., 88,* 2813–2818, 1983.

Zilitinkevich, S.S., On the determination of the height of the Ekman boundary layer, *Bound. Layer Meteorol., 3,* 141–145, 1972.

Zilitinkevich, S.S., Resistance laws and prediction equations for the depth of the planetary boundary layer, *J. Atmos. Sci., 32,* 741–752, 1975.

A Mechanism for Floe Clustering
in the Marginal Ice Zone

M. LEPPARANTA* AND W.D. HIBLER III

*U.S. Army Cold Regions Research and Engineering Laboratory
Hanover, New Hampshire 03755*

On leave from the Institute of Marine Research, Helsinki, Finland

During the MIZEX 83 Greenland Sea pilot study, clustering of ice floes was noted as a typical feature in the marginal ice zone (MIZ). One dominant manifestation of this clustering is the presence of thicker ice near the ice edge. Evidently, differential motion among the floes is due to the variability of the characteristics of the floes themselves. It is suggested here that free-drift variations due to floe thickness differences is a key characteristic in this clustering phenomenon. These variations are reflected in the dependence of the inertial and Coriolis forces on ice thickness. The basic idea dates back to Zubov (1945) but has not been touched on recently in connection with MIZ floe characteristics.

The Greenland Sea MIZ is a mixture of first-year and multiyear ice floes with thicknesses ranging from 1 to 4 m. Due to the Coriolis force, heavy floes tend to drift more slowly and more to the right of the wind than light floes. This is an efficient mixing mechanism and produces clusters, as light floes catch up with heavy floes in some places and drift apart from them in others.

To examine this process theoretically we will consider the movement of floes on the basis of the free-drift balance. In addition, Monte Carlo numerical calculations with free drift assumed are carried out. This approach is reasonable in the marginal ice zone, since mixing of floes is most efficient when internal stresses within the MIZ are small, i.e. when the ice is diverging or ice compactness is less than 0.8–0.9. We consider the effect of the Coriolis force only and ignore possible modifications due to the inertia of the ice.

The steady-state, free-drift balance, considering the wind and water stresses and the Coriolis force, is written as (Hibler, 1984)

$$\varrho_a C_a U_a (\cos\phi + \sin\phi \mathbf{k} x) \bar{U}_a -$$

$$\varrho_w C_w u (\cos\theta + \sin\theta \, \mathbf{k} x) \bar{u} - \varrho_i h f \mathbf{k} x \bar{u} = 0, \quad (1)$$

where ϱ_a, ϱ_w, and ϱ_i are the air, water, and ice densities, respectively, C_a and C_w are the air and water drag coefficients, ϕ and θ are the air and water turning angles, $\bar{U}_a$ is the wind velocity, $\mathbf{k}$ is the unit vector vertically upward, $\bar{u}$ is the ice velocity, h is the ice thickness, and f is the Coriolis parameter. The solution depends on the boundary layer angles and two additional independent dimensionless products. Choosing (Lepparanta, 1981)

$$Na = \left(\frac{\varrho_a C_a}{\varrho_w C_w}\right)^{1/2}, \qquad R = \frac{\varrho_i h f}{U_a \sqrt{\varrho_a C_a \varrho_w C_w}}, \quad (2)$$

the solution can be written

$$u/U_a = Na \cdot F(R, \theta),$$

$$\cos(\beta + \phi) = \cos\theta \cdot F^2(R, \theta). \quad (3)$$

Here β is the deviation of ice drift direction to the right of the wind direction. The function F is given by

$$F^4 + 2\sin\theta R F^3 + R^2 F^2 - 1 = 0. \quad (4)$$

For a fixed oceanic boundary layer angle θ, F decreases monotonically from 1 to 0 as R goes from 0 to infinity (Fig. 1). Note that F is only weakly dependent on θ.

Ice thickness affects the free-drift solution through R being proportional to h. Hence, as h increases, the wind factor u/U_a decreases and deviation angle β increases. Note also that R is inversely
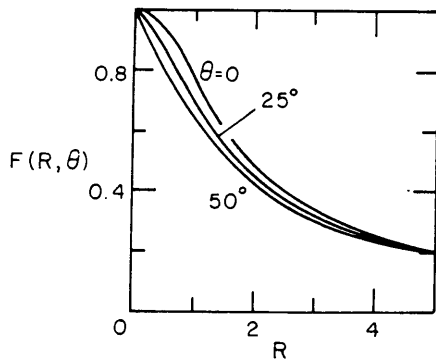
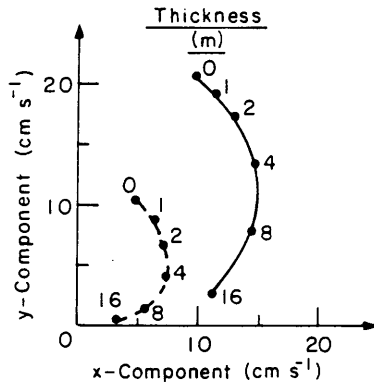*Fig. 1. The function* F *in the free-drift solution.*

Fig. 2. Free-drift cases: wind stress is aligned with the y-axis and the dots mark the tips of the ice drift vectors; ice thickness = 0, 1, 2, 4, and 16 m and wind speed = 5 and 10 m/s.

proportional to the wind speed. Some solutions are shown in Figure 2 in vector form for two different wind speeds. Since 1 cm/s approximately equals 1 km/day it is seen that neighboring first-year and multiyear ice floes can drift apart several kilometers in one day due to the thickness difference only. Such a phenomenon was in fact observed in MIZEX 83. In particular, after several days of off-ice winds, two originally adjacent floes that had been marked were relocated and found to be more than 1 mile apart.

It is also worth noting that floe clustering due to differential drift of floes is a substantial conceptual change from the thickness distribution concepts used in most sea-ice models (see e.g. Hibler, 1984). In conventional sea-ice models, one velocity is normally used for a variety of ice thicknesses in a region, and statistical ice thickness variations are then deduced from the gradients of this velocity field. Taking into account differential drift of different floes would require a conceptual reformulation of such theories.

To examine whether in fact such drift variations could create clusters, a Monte Carlo simulation was carried out. The results clearly support our reasoning above (Fig. 3). Initially, ice floes were randomly distributed in space with random thicknesses up to 5 m. Only one drift component

was simulated. The system works so that when a light floe catches a heavy floe, they stick together and drift as a group; their mean thickness then determines the drift velocity. Floe clustering is seen for all our ice compactness values. Very similar results were obtained when the floes were initially equally rather than randomly spaced.

There is not yet sufficient data on the drift of various floes to test our theory. It is consequently recommended that field measurements relevant to this problem be made during the MIZEX 84 main experiment. One might think that differential drift among floes is caused also by form drag variations. From field data on the drift vectors of floes of different thicknesses it should be possible to resolve the role of form drag and thickness variations in the drift of ice floes.

Ice thickness variability is suggested to be an important factor in floe mixing since it implies differential drift among floes through the Coriolis force. Further, this mechanism also causes floe clustering. It is believed that the abundance of floe clustering in the Greenland Sea MIZ in the summer of 1983 was due to thickness variations; the range was typically 1 to 4 m.

Zubov (1945) suggested that thickness variations cause ice bands. This may not be exactly true, but we think that, at least in the initialization

INITIAL COMPACTNESS 1%, SPACING RANDOM.

TIME STEP = 10, COMPACTNESS = 5.0 %.

INITIAL COMPACTNESS 50.0 %, SPACING RANDOM.

TIME STEP = 100, COMPACTNESS = 47.1 %.

INITIAL COMPACTNESS 80.0 %, SPACING RANDOM.

TIME STEP = 100, COMPACTNESS = 71.7 %.

INITIAL COMPACTNESS 90.0 %, SPACING RANDOM.

TIME STEP = 100, COMPACTNESS = 64.3 %.

Fig. 3. Monte Carlo simulation of floe clustering. In each case the lines follow each other, forming a single long line. Each digit gives the thickness of an ice floe rounded in meters. The total time is 100 minutes times the floe size in meters. A uniform wind of 10 ms⁻¹ was assumed.

of band formation, thickness variations are important.

REFERENCES

Hibler, W.D., III, Ice dynamics, in *Air–Sea–Ice Interaction, NATO Institute Proceedings,* edited by N. Untersteiner, Plenum Press (in press), 1984.

Lepparanta, M., On the structure and mechanics of pack ice in the Bothnian Bay, *Finn. Mar. Res., 248,* 3–86, 1981.

Zubov, N.N., *L'dy Arktiki,* Izdatel'stvo Glavsevmorputi, 360 p. Moscow, 1945.

A Markov Model for Sea Ice Trajectories

R. COLONY

Polar Science Center, University of Washington, Seattle, Washington 98195

This paper outlines a stochastic/kinematic model of sea ice motion in which the trajectories of ice floes in the Arctic Ocean are modeled as a random process. Such a model is considered for two reasons: first, because of the intrinsic unpredictability of atmospheric and oceanic circulation, uncertainty of historical records, and incomplete knowledge of the governing equations of motion; second, because it may be a way of quantifying the interannual variability of sea ice motion. The central idea is to make use of observations of ice motion to construct a statistical description of the field of motion during a small time interval. Building on this it is possible to predict the long-term statistical properties of the trajectories in such a field. The random ice particle trajectories are modeled as a discrete time, finite state, Markov process in which the state of the ice particle is defined by its location. Varia-

tions of the question: *If a marked particle occupies region Ω at time t, what is the probability that it will be (or could have been) in region Ω' at time t'?* are addressed.

The random motion of a marked particle in the time interval τ is characterized by the conditional probability density function $f(y|x)$. This function gives the probability that the particle occupies location y at time $t + \tau$ given that it was at location x at time τ. In the present model we assume $f(y|x)$ to be the bivariate Gaussian distribution

$$G(y; x + \bar{u}, \sigma^2) = (2\pi\sigma^2)^{-1} \exp[-|y - x - \bar{u}|^2/2\sigma^2]$$

where $\bar{u} = \bar{u}(x, \tau)$ is the mean motion in the time interval τ, and σ^2 is the variance of the single component departure from the mean. Figure 1 shows the field of mean motion and Figure 2 shows the variance of the departure as a function of τ. If τ is
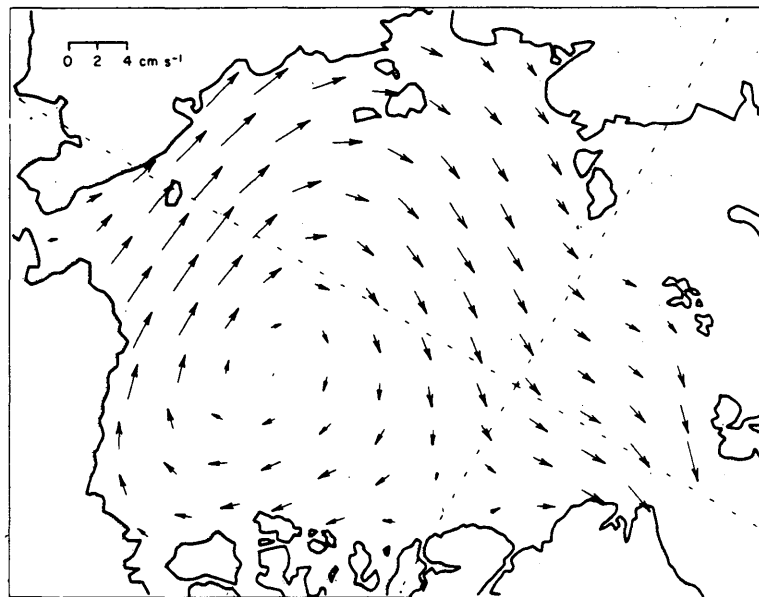

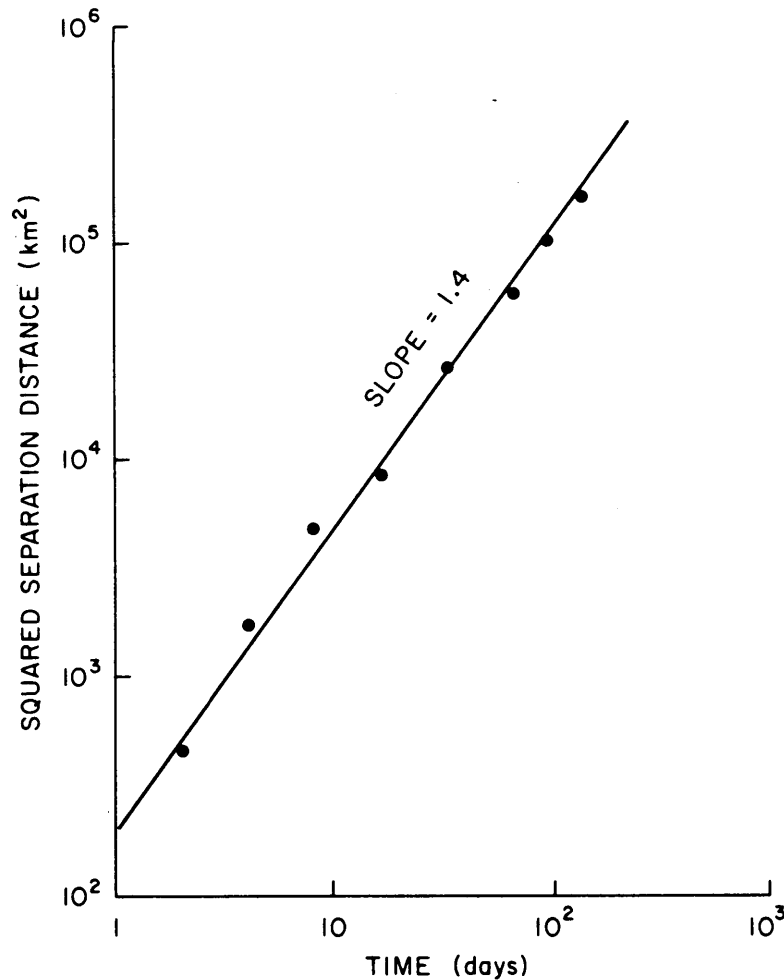Fig. 1. The mean velocity field as analyzed from observed motion (Colony and Thorndike, 1983).

77

Fig. 2. Pairs of intersecting trajectories have been analyzed. These trajectories share a common location, say x_c, *but at different times, e.g.,* X(t) = Y(t') = x_c. *The variance of their subsequent separation* |X(t + τ) − Y(t' + τ)| *is shown as a function of* τ. *Then* σ^2 = ¼ *variance* |X(t + τ) − Y(t' + τ)| *(Colony and Thorndike, in progress).*

chosen as 90 days, then $|\bar{u}| \approx 200$ km and $(2\sigma^2)^{\frac{1}{2}} \approx 225$ km. A typical situation is shown in Figure 3.

Thermodynamics also plays a role in modeling random trajectories. A marked ice particle may melt in the marginal seas and thus terminate its trajectory. Similarly the marginal seas are a source of surface ice cover and thus trajectories may be initiated in these regions. Figure 4 shows the average summertime ice-free regions.

The Arctic Basin is partitioned into a number of cells having the labels {1,2,...,N}. Figure 4 shows the situation for N = 111. A trajectory is said to be in state *i* at time *t*, [X(t) = *i*], if the marked particle occupies cell *i* at that time. Furthermore a trajectory is said to be in state * at time *t* if the trajectory has been terminated at or before time *t*. The stochastic process describing probable future tra-

jectories of a particle having present position, x_0, is given in terms of the conditional probabilities:

$$p_{ij} = Pr[X(t_{k+1}) = j | X(t_k) = i]$$
particle in cell *i* moves to cell *j*

$$r_i = Pr[X(t_{k+1}) = * | X(t_k) = i]$$
trajectory is terminated in the interval (t_k, t_{k+1})

$$1 = Pr[X(t_{k+1}) = * | X(t_k) = *]$$
the trajectory remains terminated

Similarly the backward process describing the probable paths a particle could have taken to arrive at the present location is given by
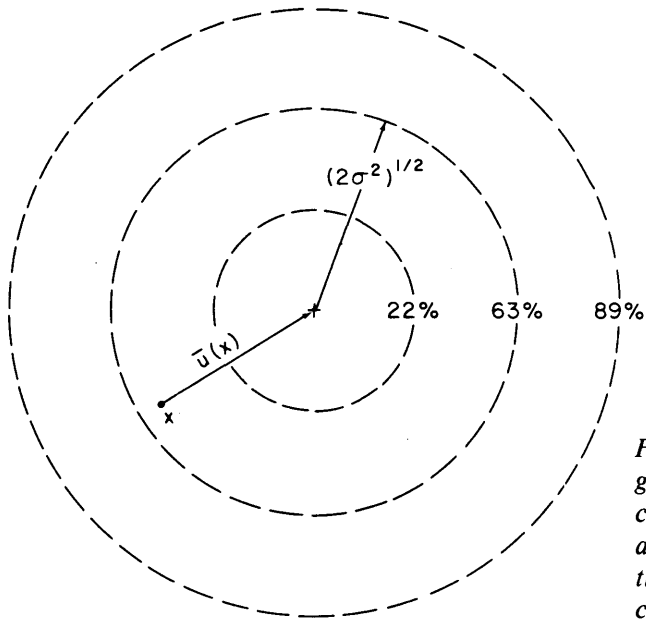
Fig. 3. The distribution of particle position at time $t + \tau$ given that it had position x at time t is illustrated. The circles are shown with radius of $r = 0.707\sigma$, 1.414σ, and 2.121σ and are centered about the expected position $\bar{y} = x + \bar{u}$. The probability that y is inside the circles is 22%, 63%, and 89% respectively.
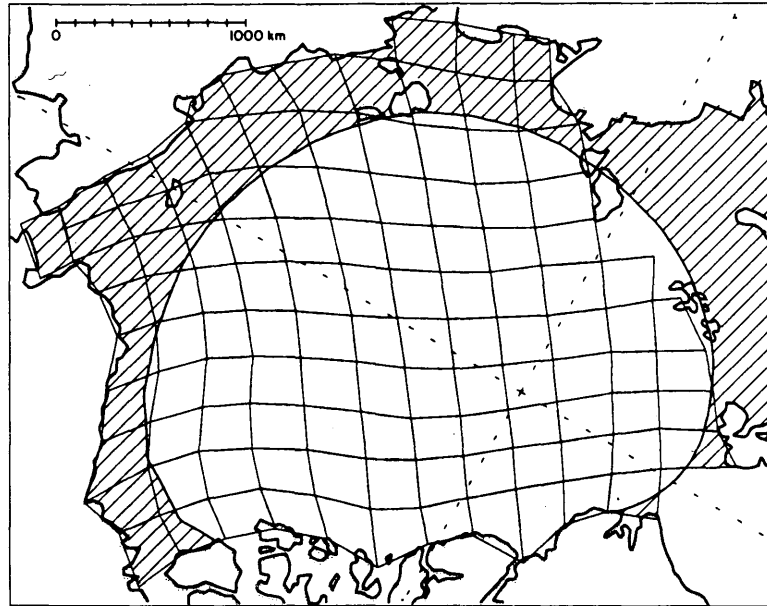

Fig. 4. The average summertime ice-free regions as analyzed from observations (Lemke et al., 1980).

$q_{ij} = Pr[X(t_{k-1}) = j | X(t_k) = i]$
particle in cell i came from cell j

$s_i = Pr[X(t_{k-1}) = * | X(t_k) = i]$
trajectory was initiated in the interval (t_{k-1}, t_k)

$1 = Pr[X(t_{k-1}) = * | X(t_k) = *]$
trajectory did not exist before it was initiated.

Trajectories are terminated when the marked particle melts or moves out of the region of interest. Similarly, a trajectory is initiated with the formation of a surface ice cover or when a particle moves into the region of interest. The forward and backward transition probability matrices

$$\vec{A} = \begin{bmatrix} P & R \\ 0 & 1 \end{bmatrix} \text{ and } \overleftarrow{A} = \begin{bmatrix} Q & S \\ 0 & 1 \end{bmatrix}$$

organize these conditional probabilities.

The forward and backward processes are related by the unconditional probabilities

$$r_i^* = Pr \text{ (trajectory terminated from state } i)$$

$$s_i^* = Pr \text{ (trajectory initiated in state } i).$$

These are the probabilities that a particle melts or leaves the region from (forms or enters the region into) cell i. The forward and backward recurrent transition probability matrices are

$$\vec{B} = \begin{bmatrix} P & R \\ S^* & 0 \end{bmatrix} \text{ and } \overleftarrow{B} = \begin{bmatrix} Q & S \\ R^* & 0 \end{bmatrix} \text{ where } S^* = \{S_i^*\}, \ R^* = \{r_i^*\}.$$

It can be shown that the row vector $\Pi = (\pi_1, \pi_2, ..., \pi_N, \pi^*)$ satisfies

$$\Pi = \Pi\vec{B}, \ \Pi = \Pi\overleftarrow{B}, \ \pi_j > 0, \ \sum_{j=1}^{N} \pi_j = 1,$$

$$\pi_j = \lim_{n \to \infty} Pr[X(t_n) = j | x(t_0) = i].$$

The π_j are the stationary distribution of the processes $\vec{B}$ and $\overleftarrow{B}$. Note that after a very long time the process is at a random position on a trajectory that was initiated by the rule S^*, therefore we have the interpretation

$$\pi_j = Pr \text{ (ice particle is in cell } j).$$

Using the identity $Pr(X|Y) \cdot Pr(Y) = Pr(X \text{ and } Y)$, the forward and backward transition probabilities are related,

$$\pi_i q_{ij} = \pi_j p_{ji}, \ \pi^* r_i^* = \pi_i r_i, \ \pi^* s_i^* = \pi_i s_i.$$

Numerical values of the transition probabilities p_{ij} and r_i are obtained by appropriate integration of $f(y|x)$ over various regions. The elements of S^* are obtained by integration over the source regions of surface ice cover, assumed here to be the summertime ice-free region shown in Figure 4. After evaluation of P, R, and S^*, the above formulas are used to calculate Q, R^*, S, and Π.

Having established the symmetry of the forward and backward processes, it is sufficient to consider only the forward process characterized by $\vec{A}$. The n step probabilities

$$p_{ij}^{(n)} = Pr[X(t_{k+n}) = j | X(t_k) = i]$$

are simply the ij^{th} element of the nth power of P. The n step transition probability matrix for the process $\vec{A}$ is

$$\vec{A}^n = \begin{bmatrix} P^n & R_n \\ 0 & 1 \end{bmatrix}, \ R_n = \sum_{v=1}^{n} P^{v-1} R.$$

The elements of R_n are the probabilities that the trajectory has terminated after n steps, given that the marked particle had initial location in cell i.

The calculus of Markov chains is replete with formulas for the statistics of the process. Conditional on the marked particle having present position, x_0, the random model gives the following statistics for the forward process:

- the distribution of time until trajectory termination
- the distribution of time until trajectory termination, conditional on the way the trajectory is terminated
- the probable locations in a fixed drift time
- the probability of melting in a particular region
- the probability of exiting the Fram Strait
- the probability of visiting a particular region
- the mean time the particle resides in a particular region
- the variance of the residency time in a particular region.

Similar statistics are available for the backward process.

This paper has described a stochastic kinematic model that predicts a number of important properties of the ensemble of trajectories in terms of a small number of physically meaningful and experimentally accessible parameters. The preliminary finding from the model is that the random trajectories are rich in that many different things are likely to happen to an ice particle and that the events occur on very different time scales.

The paper "Sea Ice Motion as a Drunkard's Walk," by R. Colony and A.S. Thorndike is being prepared and will be submitted to the *Journal of Geophysical Research*. Application of this model for describing oil spill trajectories is being sponsored by OCSEAP. The work reported here was supported by the National Oceanic and Atmospheric Administration Grant NA80-AA-D-00015.

REFERENCES

Colony, R., and A.S. Thorndike, An estimate of the mean field of arctic sea ice motion, paper presented at Eighth Conference on Probability and Statistics in Atmospheric Sciences, Hot Springs, Ark., 1983.

Colony, R., and A.S. Thorndike, Sea ice motion as a drunkard's walk, *J. Geophys. Res.,* in progress.

Lemke, P., E.W. Trinkle, and K. Hasselmann, Stochastic dynamic analysis of polar sea ice variability, *J. Geophys. Ocean., 10:* 2100–2120, 1980.

Internal Wave Forces on Ice Keels in the Marginal Ice Zone: Some Preliminary Laboratory Results

R.D. MUENCH AND L.E. HACHMEISTER

Science Applications, Inc., 13400B Northrup Way, No. 36, Bellevue, Washington 98005

Forces that exert an influence over the motion of sea ice in the marginal ice zones (MIZ's) include wind and current drag, surface wave radiation stress, and internal ice stress. Internal waves may also be present in the density-stratified water that underlies the MIZ, typically a region of active ice melting; these internal waves can exert forces on under-ice features that are of the same magnitudes as those due to water drag. A series of laboratory experiments has been carried out to investigate the internal wave drag on ice features and to estimate the conditions under which such forces can be appreciable when compared to other drag forces. Results obtained using model scaling for the summer Beaufort Sea MIZ indicated maximum values for internal wave drag of about 30% more than the combined skin and form water drag for a single-keel case and about 80% more for a double-keel case. Modeled ice speeds were in the 10–70 cm/s range, typical of the MIZ. The observed dependence of internal wave drag on keel speed and, for the double-keel case, on spacing appears to be complex and nonlinear. Because the magnitude of the drag relative to the combined form and skin drags is appreciable over most of the realizable ice speed ranges, such internal wave effects need to be considered in modeling ice dynamics in the MIZ where the ice overlies density-stratified water.

Sea ice moves over the surface of the ocean under the influence of both internal stresses in the ice and forces exerted by the wind and upper layers of the ocean. The ice/ocean coupling affects both the ice motion and the dynamics of the upper ocean layers. These coupling mechanisms have several forms. In the absence of oceanic stratification, drag forces between the ice and the water result from a combination of skin friction (applied over the entire underside of the ice) and form drag exerted by the irregularities (keels) on the lower side of the ice cover. In a stratified fluid an additional coupling mechanism exists: as demonstrated by Ekman (1904), internal waves generated by an irregularity or obstacle can contribute a significant wave-induced resistance to the motion. Hachmeister and Rigby (1980) modeled this mechanism in a laboratory towing tank and detected drag increases, due to interactions between a simulated ice keel and first- and second-mode interfacial drag theory (Wadhams 1983). Their work suggested that "wave drag" forces can be comparable under certain conditions to the frictional drag forces exerted on the ice by winds and currents, and can therefore affect the ice response to wind forcing.

While definitive observations of internal waves in the MIZ are not available, theoretical considerations and several short data records suggest that they may in fact be widespread. Muench et al. (1983) have presented a simple theoretical development that utilizes wind shear across an ice edge to generate internal waves. In the same paper, they present field data that suggest that internal waves of the sort predicted by the theory were present in the winter Bering Sea MIZ. Although internal waves were detected again in the Bering Sea MIZ in February 1983 (unpublished data), the records were too short to allow rigorous analyses of the wave fields. Unpublished 1981 data (J. Newton, Science Applications, Inc., La Jolla, Calif.) showed the presence of internal waves in the Beaufort Sea MIZ during the summer period of high-density stratification. All these records were too short and/or crude to allow comparison with theory, but they nevertheless revealed fluctuations consistent with the presence of internal waves.

This paper presents and discusses some preliminary results from a series of towing tank experiments, and represents an extension of those originally reported upon by Hachmeister and Rigby (1980). While their results concentrated primarily on second-mode interfacial waves, the present work addresses problems associated with
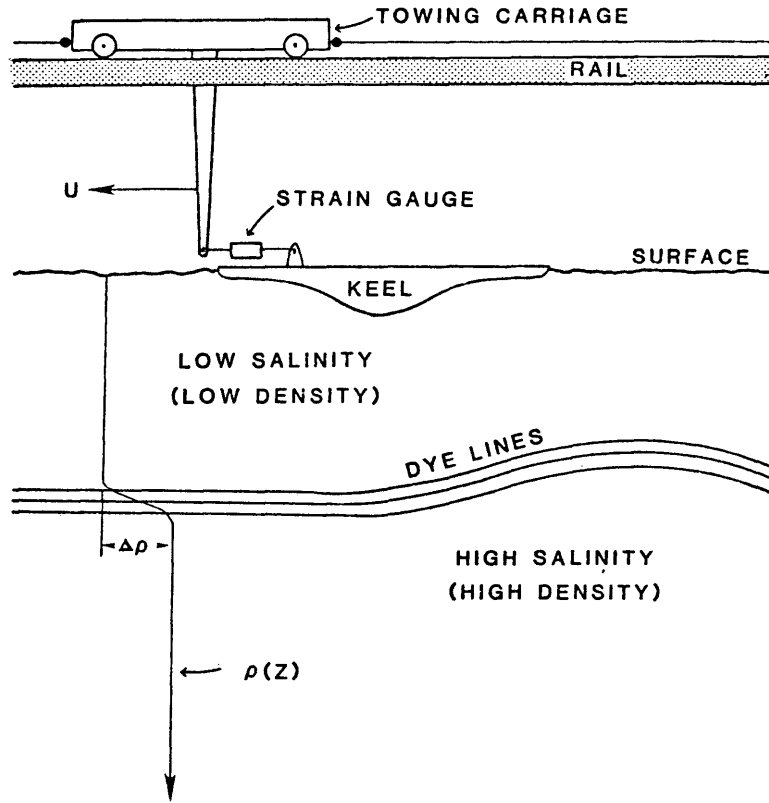
Fig. 1. Schematic of experimental setup used to observe internal wave stress acting on a simulated ice keel. Stratification is expressed as $\Delta\varrho$, keel motion is in direction indicated by arrow "U."

the faster-moving first-mode waves. In addition, it has been possible to investigate a wider range of stratification conditions than was studied during the initial series of experiments, which focused on conditions in the central Arctic Ocean rather than at the MIZ. A greater recent availability of temperature and salinity—hence, density—data from the MIZ has allowed more realistic scaling of the towing tank parameters. The results presented below represent conditions in the summer Beaufort Sea MIZ and utilize model parameters scaled to the observed summer conditions in the Beaufort Sea.

The experiments were conducted at Science Applications, Inc., in Bellevue, Washington, in a stratifiable towing tank that is 15 m long, 0.5 m wide, and 1 m deep (Figure 1). Density stratification was achieved by layering water of varying densities (salinities). Froude number scaling was used to scale the tank stratifications to correspond to summer Beaufort Sea conditions. This stratification consisted of a two-layered system with a sharp interface separating the upper and lower layers (Figure 2). First-mode interfacial wave speeds C_1 were derived from a two-layered fluid model given in Turner (1973). The basic

equation for the phase speed C_1 is

$$C_1^2 = (g\Delta\varrho/k) (\varrho_1 \coth kh_1 + \varrho_2 \coth kh_2)^{-1}$$

where h_1 is the upper layer thickness, h_2 is the lower layer thickness, ϱ_1 is the upper layer density, ϱ_2 is the lower layer density, and $\Delta\varrho$ is the density difference between layers. In the shallow-water, long-wave case represented by the experimental wave tank and in the Beaufort Sea, kh_1 and kh_2 both approach zero, and the above equation reduces to

$$C_1^2 = \frac{g\Delta\varrho}{\varrho_2} \frac{h_1 h_2}{(h_1 + h_2)}.$$

This last form was then used to compute C_1.

Once the tank was filled and stratified, single and double simulated ice keels, with cross-sections as shown in Figure 1, were towed lengthwise along the tank over the water surface. The keel(s) were coupled to a variable-speed towing carriage directly through a voltage-generating force gauge/dashpot. The voltage from this gauge was directly proportional to the force acting on the

84

DENSITY (SIGMA-t)   DENSITY

23   25   27   (AS ARBITRARY
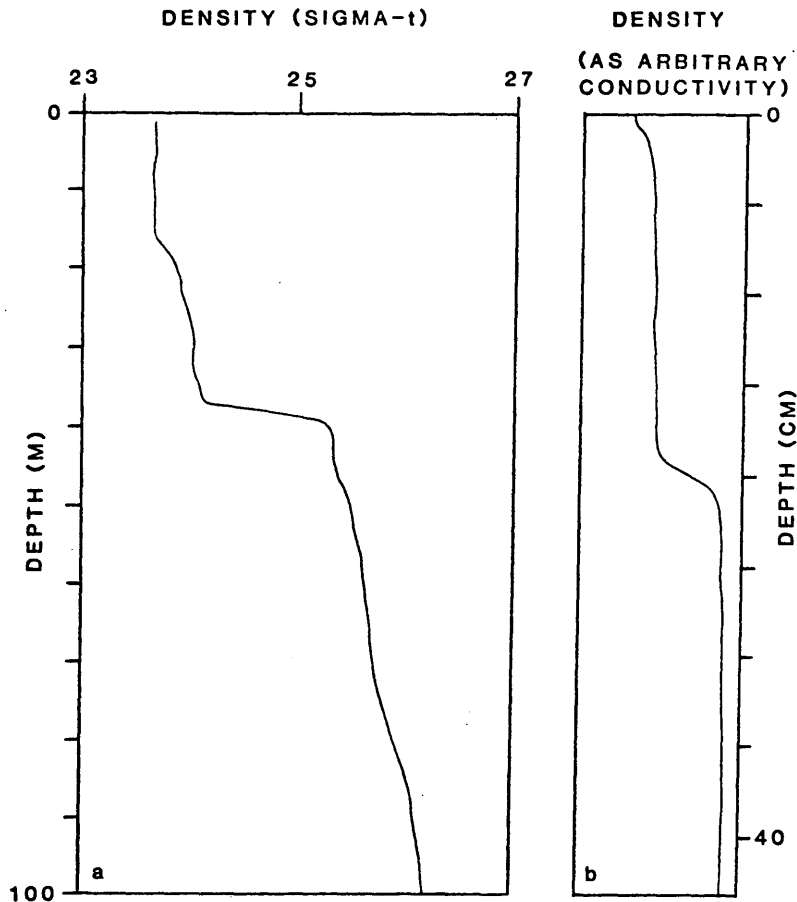   CONDUCTIVITY)

Fig. 2. Vertical profiles showing (a) the vertical distribution of density in the summer Beaufort Sea MIZ, and (b) the vertical distribution of density (saliity expressed here as conductivity) used in the actual laboratory experiment.

gauge, so it provided a measure of the stress being exerted on the towed keel(s). During each experimental tow, internal wave formation was monitored in two ways. Dye layers placed along the interface between upper and lower water layers were photographed using still and movie cameras during wave generation and passage. In addition, conductivity microprobes were used to monitor vertical displacements of the interface during passage of internal waves. It was thus possible to observe such wave characteristics as the number of waves in a given train, wave amplitudes, wave length, phase speed, lag of the wave behind the keel, and the interactions between waves and the second keel (for the double-keel cases).

The density stratification used for the results described below represents summer conditions along the Beaufort Sea MIZ. Modeled ice speeds for the keels were varied over the 10 to 70 cm/s range to simulate typical MIZ speeds. In the double-keel cases, spacing between the two keels

was varied. Keel spacings in the tank correspond typically to in situ spacings of 200 to 400 m.

The results of the Beaufort Sea MIZ runs are shown on Figures 3 to 5. Several different runs were required to arrive at these results. First, a series of runs was made for the single-and double-keel cases at varying tow speeds in unstratified conditions to measure the combined form and skin friction drag D_f in the absence of wave forces. Second, a duplicate series of runs was made for the stratified case, which yielded measurements of the combined wave drag D_w and form and skin friction drag D_f. The wave drag D_w was obtained by simply taking the differences between the two data sets.

In the specific case modeled, the model keel depth corresponded to a 7-m-deep keel. Speed ratios U/C_1, where U was the relative field ice/water speed difference and C_1 was the computed linear first-mode interfacial internal wave speed, were varied from about 0.1 to 1.1. These
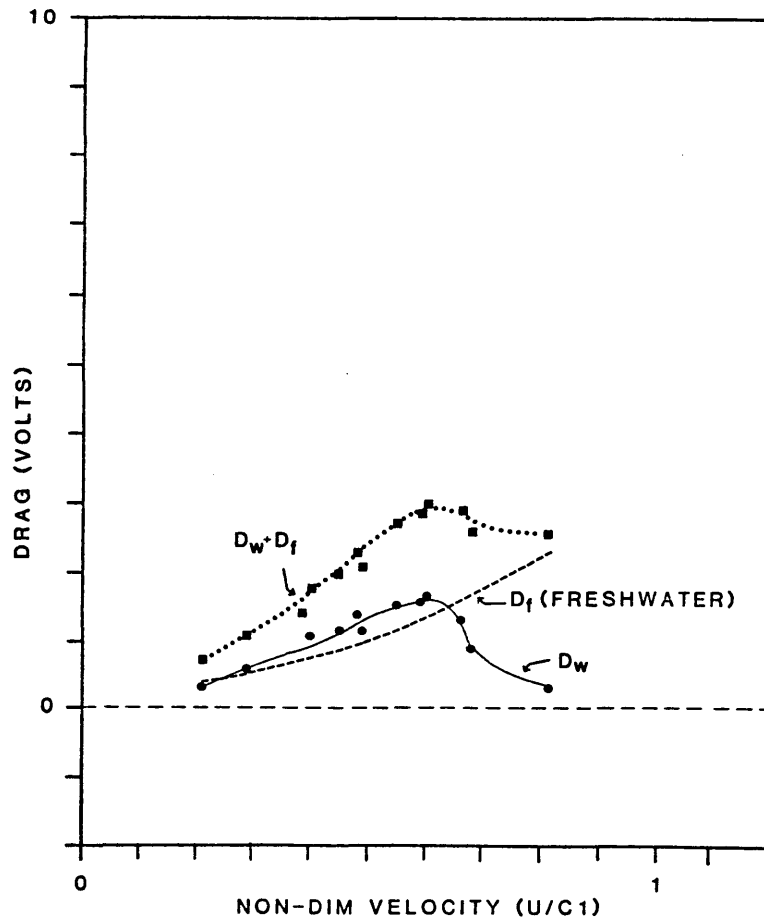
Fig. 3. Drag (expressed as voltage output from the strain gauge) exerted on a single towed keel as a function of nondimensional speed U/C₁.

corresponded to field values of $U \cong 10\text{-}70$ cm/s and $C_1 \cong 70$ cm/s. The combined form and skin drag D_f increased for the freshwater case, as was expected, monotonically with increasing speed (Figure 3). Introduction of stratification resulted in the formation of from 1 to 6 or more first-mode interfacial waves, with the number of waves in the train depending on the towing speed, and radically altered the relation between total drag and towing speed. In the stratified case, the total drag $D_f + D_w$ increased far more sharply with increasing speed than did D_f alone. This rapid increase occurred as U/C_1 approached 0.5, a value corresponding to field keel speeds of 30–40 cm/s. As U/C_1 was increased above about 0.6, i.e. as keel speeds were increased above about 40 cm/s, total drag $D_f + D_w$ dropped off sharply as U/C_1 approached 0.7. At this point, $D_f + D_w$ approached D_f. The difference between drag for the homogeneous and the stratified cases was due to the internal wave drag D_w. This wave drag reached a maximum when the keel speed was about half the first-mode inter-

facial wave speed and decreased sharply at speeds slower or faster than this value. The maximum observed value of the ratio D_w/D_f (wave drag to combined form and skin drag) was approximately 1.3.

A second set of experiments was run using the same stratification and keel speeds as above, but with a double rather than a single keel. Keel spacing in the experiment was scaled to correspond to a field spacing of about 200 m. The results are shown in Figure 4, and the single- and double-keel results are compared in Figure 5. The effects of the internal wave drag D_w were far greater for the double keels than for the single keels. The maximum observed value of D_w/D_f for the double-keel case, which occurred at $U/C_1 \cong 0.5$, was approximately 1.8. Values of both D_f and D_w for the double-keel case were highly dependent upon the spacing between the two keels.

The values reported above were derived for stratification conditions corresponding to the summer Beaufort Sea MIZ. The first-mode internal interfacial wave speed C_1, derived from the
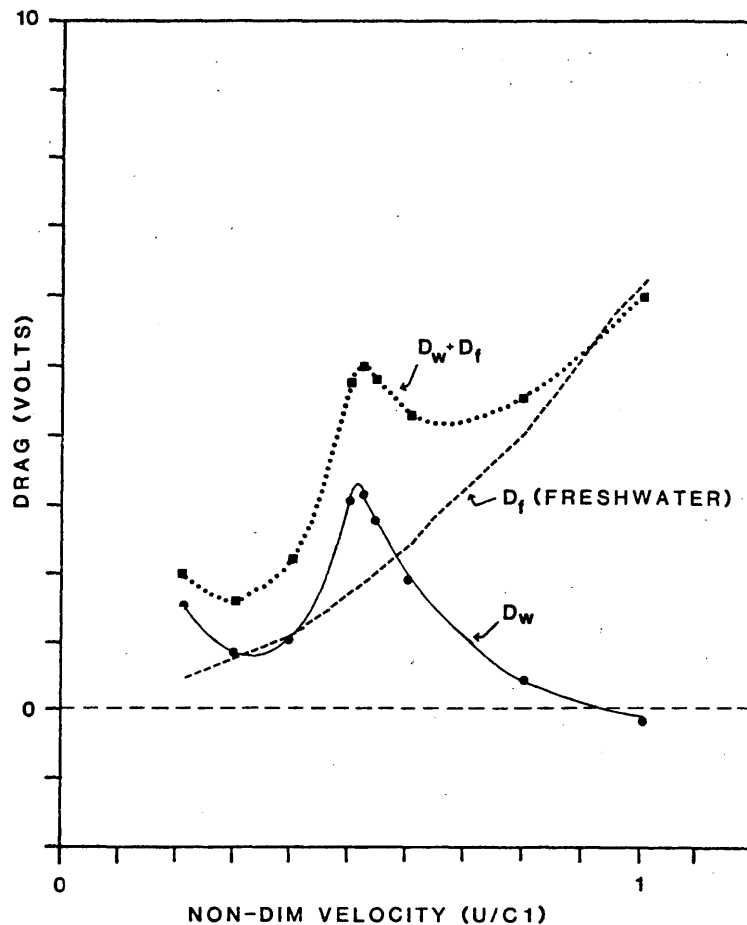
86

Fig. 4. Drag (expressed as voltage output from the strain gauge)
exerted on a double towed keel as a function of nondimensional
speed U/C_1. Spacing between the two keels was 100 cm, corre-
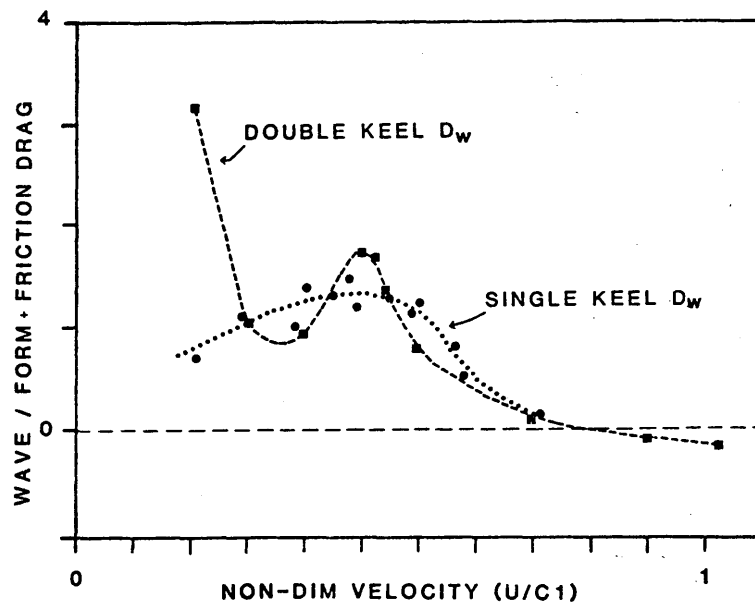sponding to a field spacing between keels of 200 m.

Fig. 5. Comparison of nondimensionalized drag D_w/D_f for the
single- and double-keel cases over a range of nondimensionalized
speeds U/C_1.

Table 1. Computed first-mode internal wave speed C_1 in cm/s for the Bering and East Greenland Sea cases (from Muench et al., 1983).

		C_1 (cm/s)				
Case	h	$\Delta\varrho$ 0.00010	$\Delta\varrho$ 0.00025	$\Delta\varrho$ 0.00050	$\Delta\varrho$ 0.00100	$\Delta\varrho$ 0.00500
Bering Sea: bottom	25	14	22	30	42	96
depth ~ 100 m	50	16	26	36	51	114
	75	15	24	34	48	107
East Greenland Sea:	25	15	24	35	49	109
bottom depth > 1000 m	50	22	35	49	69	155
	75	27	42	60	85	189

$\Delta\varrho$ is the density difference in q/cm³ across the interface between the upper and lower layers; h is the depth of the interface in meters.

stratification, is a critical parameter in analyzing internal wave stresses on ice keels. Therefore, a comparison of C_1 computed for some different MIZ regions would give an indication of how widespread the importance of these stresses might be. To this end a tabulation of computed C_1 for the Bering and East Greenland Sea MIZ's is reproduced here as Table 1. It is seen that the value $C_1 = 70$ cm/s, which was selected as typical for the Beaufort Sea case, is also typical of the higher stratifications $\Delta\varrho$ and/or the greater upper-layer thicknesses h for both the Bering and East Greenland Sea cases. There are to date few observations of the ice speed U relative to the underlying water. It would be expected, however, based both upon physical reasoning and the available observational information, that a range of U would be encountered in the MIZ that would encompass the values of C_1 presented in Table 1. This is supported by as yet unpublished observations (R.M. Reynolds, PMEL/NOAA, Seattle, Wash.) of relative ice/water motion that were obtained from the Bering Sea MIZ during the winter 1983 MIZEX West field program there. The most commonly observed speeds were in the 10 to 20 cm/s range, or well within the range of C_1 values given in Table 1 for the Bering Sea. Physical reasoning dictates that, for U/C_1 interrelations such as discussed above, some interactions occur. It is hoped that planned rigorous analyses of the Bering Sea data will reveal how significant such interactions were in their effects on the ice motion. It is anticipated that similar data for U will be obtained during the summer 1984 MIZEX East program in the Greenland Sea, and will be available for comparson with the above values for C_1 or with values computed directly from the stratification data obtained during the field program.

It is obviously of interest to examine the possible impact of internal wave forces on modeling of ice motion in the MIZ. Some useful numbers have been provided by Wadhams (1983), who used a case study of ice band motion in the Bering Sea by Bauer and Martin (1980) to derive relative magnitudes of the wind and water drag and wave radiation stress acting on ice. He used the force balance on a 20-m-diameter ice floe to derive values for comparison. Since the ice was along the Bering Sea MIZ it was not heavily ridged; although ice in either the East Greenland or Beaufort Sea MIZ would be expected to be ridged, the derived values are nevertheless instructive. The water drag on the floe was computed to be about three times the wind drag, and about half the surface wave radiation stress (expressed as drag) exerted on the floe by a locally wind-driven sea. The internal wave force values presented above suggest that in some cases these forces could approach those due to the surface wave radiation stress. This would be in the cases of double keels having critical spacing relative to the stratification. Single keels and double keels with varying spacing would yield lower internal wave forces. In many cases, however, these could be of the same order as the wind drag.

The force vs speed curves presented in Figures 3 and 4 suggest yet another possibility. The sharp rise in internal wave force at U/C_1 values approaching 0.5 to 0.6 might cause ice to "pile up" behind these waves. At some point the external forcing due to winds and surface wave radiation stress might become great enough to overcome the internal wave forces, at which time the ice would rapidly accelerate because its speed would place it on that portion of the force vs speed curve where internal wave forcing decreases with increasing speed. In other words, at some critical value the

ice becomes decoupled from the internal wave field. The result of this would be a grouping of ice speeds around $U/C_1 \leq 0.5$–0.6. Data from the winter 1983 (Bering Sea) and summer 1983 (East Greenland Sea) MIZEX field programs should be adequate to test this hypothesis.

The results presented and discussed above are preliminary and represent the first of a series of several experiments dealing with internal wave/ice interactions. The results, taken in conjunction with the previous referenced work, suggest that internal wave interactions will need to be considered when modeling ice dynamics in the MIZ under highly stratified oceanic conditions. Additional experiments will be carried out using conditions scaled for the Bering and East Greenland Sea MIZ's in addition to the Beaufort. Actual field data on water stratification and relative ice/water motion for these regions will, where possible, be compared.

REFERENCES

Bauer, J., and S. Martin, Field observations of the Bering sea ice edge properties during March 1979, *Mon. Weather Rev., 108,* 2045-2056, 1980.

Ekman, V.W., *The Norwegian North-Polar Expedition, 1893-96, Scientific Results, 5,* edited by F. Nansen, pp. 1-152, Longmans, Green and Co., London, 1904.

Hachmeister, L.E., and F.A. Rigby, Laboratory studies of stratified flow interactions with topography, in *Proceedings, Second IAHR Symposium on Stratified Flows,* vol. 2, pp. 623-635, Tapir Press, Trondheim, Norway, 1980.

Muench, R.D., P.H. LeBlond, and L.E. Hachmeister, On some possible interactions between internal waves and sea ice in the Marginal Ice Zone, *J. Geophys. Res., 88,* 2819-2826, 1983.

Turner, J.S., *Buoyancy Effects in Fluids,* Cambridge Univ. Press, New York, 1973.

Wadhams, P., A mechanism for the formation of ice edge bands, *J. Geophys. Res., 88,* 2813-2818, 1983.

Mean Ice Motion in the Arctic Ocean

R. COLONY

Polar Science Center, University of Washington, Seattle, Washington 98195

The observational basis of our understanding of sea ice motion comes from the trajectories of particular ice floes. These floes may have been marked by a manned research station or, more recently, by an automatic data buoy. In this note the mean field of motion is estimated from a number of trajectories dating back to 1893. Figure 1 shows most of the trajectories used in the analysis.

The basin is partitioned into a number of boxes. At the center of each box the sample mean velocity and the variance of the sampling error is obtained from the trajectory data. Figure 2 shows these statistics. The theory of optimal estimation is then used to average the sample means spatially. The resulting estimate, shown in Figure 3, is optimal in the sense that the variance of the estimation error is minimized.

The estimated mean field is rather different from the qualitative description offered by Gordienko. Furthermore it is substantially different from various mathematical models of sea ice circulation. The estimate shown here must be regarded with caution in that the analysis has assumed certain statistical properties of the spatial structure of the mean field. However, the estimated field is smooth and is fully consistent with the sample data.

A more complete description of the data and analysis procedure was presented in "An Estimate of the Mean Field of Arctic Sea ice Motion," by R. Colony and A.S. Thorndike, Eighth Conference on Probability and Statistics in Atmospheric Sciences, and Third Conference on Applied Climatology, sponsored by the American Meteorological Society, November 16-18, 1983, Hot Springs, Arkansas. Tabular data of the mean field, spatial gradients, and error estimates will be printed in the Arctic Ocean Buoy Program Data
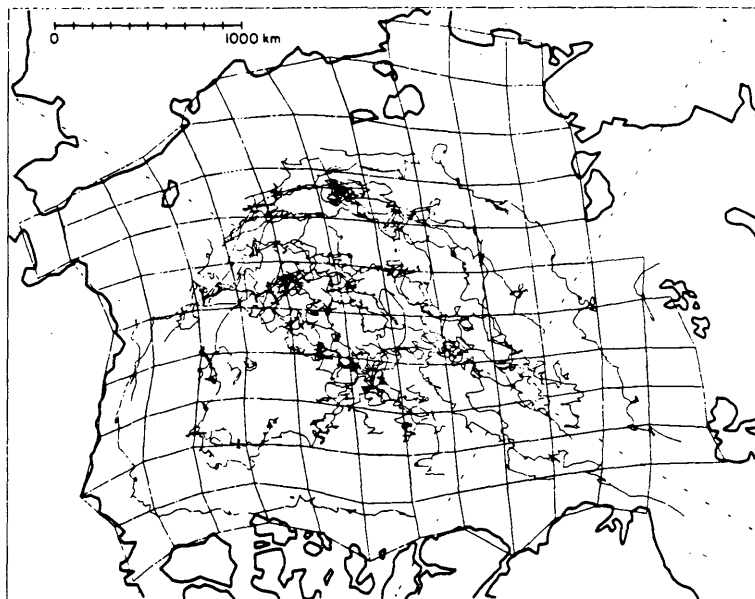

Fig. 1a. Trajectories of various research stations (1893–1972) (Hastings, 1971).
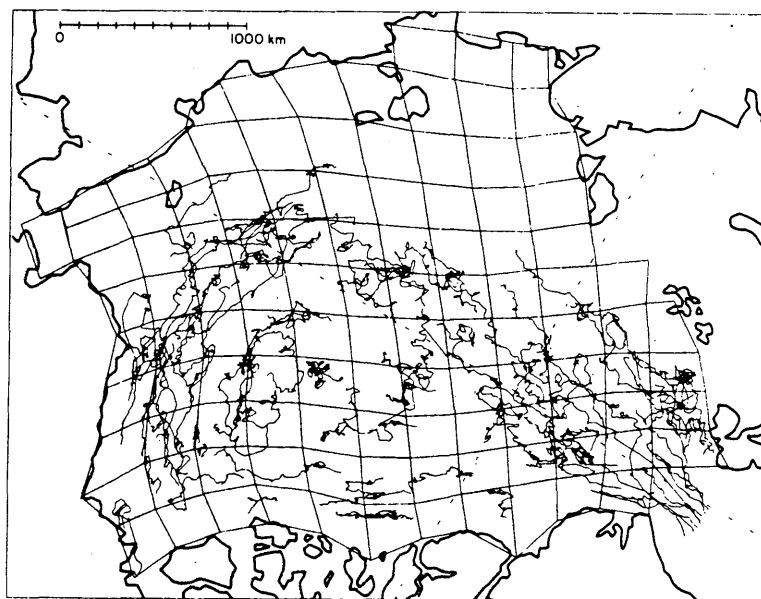
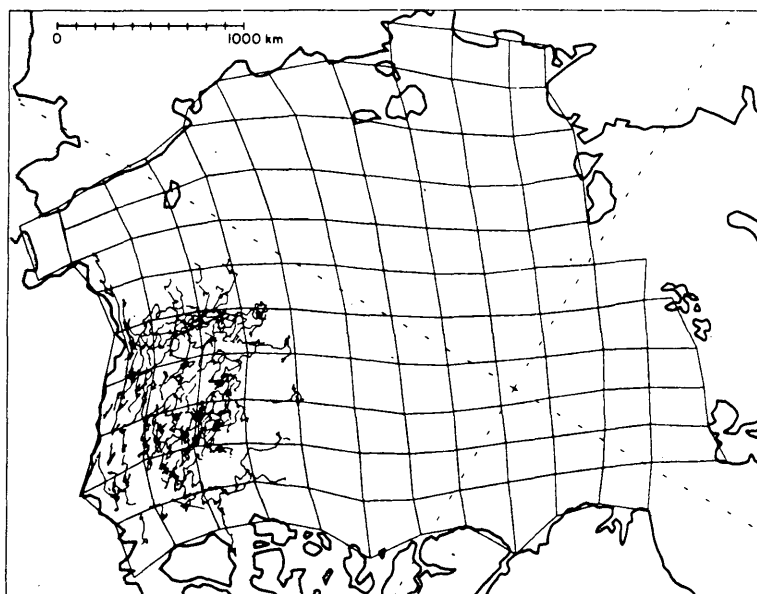*Fig. 1b. Trajectories of automatic data buoys (1979-1982) (Untersteiner and Thorndike, 1982).*

Fig. 1c. Trajectories of research stations and automatic data buoys during AIDJEX (1975-1976) (Thorndike and Cheung, 1977).
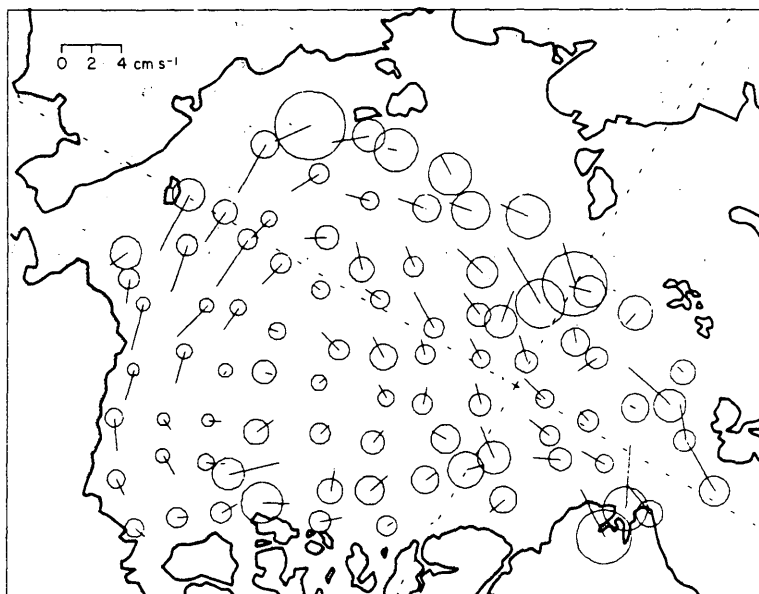
92

Fig. 2. Sample mean ice motion for the boxes shown in Figure 1. The vector originates from the center of the box and terminates with a circle of radius σ. The variance of the sample error is $\sigma^2 = q \pm (\delta/\Delta)$, where the daily sample error variance is $q^2 = 50\ cm^2\ s^{-2}$, the integral time scale is $\delta = 5$ days and Δ is the number of days the trajectory was inside the box.
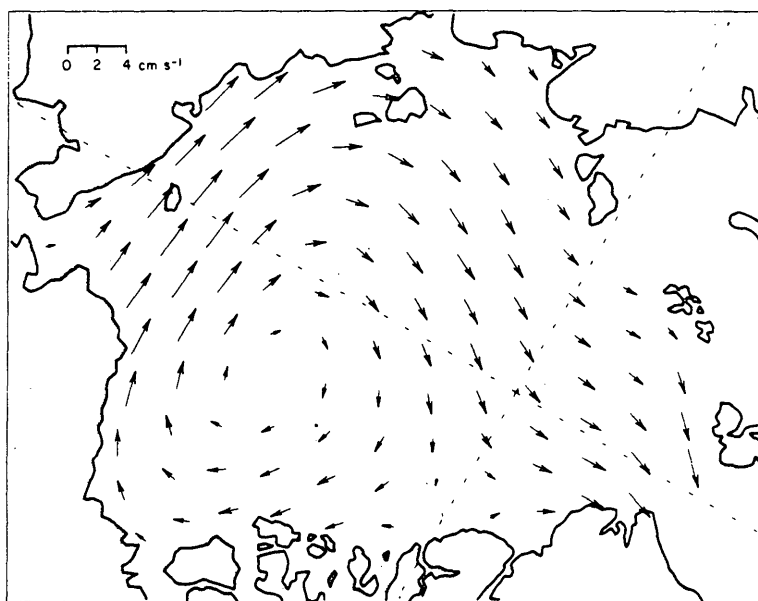

Fig. 3. Field of interpolated mean ice motion. The vectors originate at the center of the boxes. The interpolated motion in data-sparse regions should be regarded with caution.

93

REFERENCES

Hastings, A.D., Jr., Surface climate of the Arctic Basin, U.S. Army Engineer Topographic Laboratories Report ETL-TR-71-5, Ft. Belvoir, Va., 1971.

Thorndike, A.S., and J.Y Cheung, AIDJEX measurements of sea ice motion, 11 April 1975 to May 1976, AIDJEX Bulletin, 35, 1–149, 1977.

Thorndike, A.S., R. Colony, and E.A. Munoz, Arctic Ocean buoy program, Data report, 1 Jan 1981–31 Dec 1981, Univ. of Wash., Seattle, 1983.

Untersteiner, N., and A.S. Thorndike, Arctic basin buoy program, Polar Record, 21, 127–135, 1982.

Discussions of Ocean, Ice, and Atmospheric Modeling Subgroups

At the end of the workshop disciplinary discussions were held on status, approaches, and future needs of marginal ice zone modeling.

The following summaries represent some of the main views gained from the ocean, ice, and atmospheric subgroups. The ocean summary was written by Paul Budgell, the ice summary by Gary Maykut, and the atmospheric summary by Ed Andreas. Most of the registrants (see list of attendees) contributed to at least one of these disciplinary groups.

OCEAN SUBGROUP DISCUSSIONS

W.P. BUDGELL

To date, the MIZ ocean modeling efforts appear to be focused on scales of 10 to 100s of kilometers. Given this mesoscale focus, the ocean group is intermediate in length scales between the larger atmospheric-forced GCM ice modeling efforts and the smaller ice floe distribution studies. Given the ice-edge deformation at scales of 10s–20s of kilometers it appears that ocean motion at similar length scales may be important.

Pertinent scientific questions on mesoscale eddies that should be addressed include the topographic steering and trapping of eddies, formation mechanisms, and the nature of the eddy field. Do eddies occur as isolated features, in pairs, or as a multiple (2-D turbulent)-eddy field? Are the eddies evident in ice edge deformation, observable farther off edge or under ice? Answers to these questions can be obtained by sampling the background field adjacent to eddies as well as the eddies themselves. This background mean flow information is also necessary input in numerical model initialization.

An additional necessary component of two-layer model initialization is knowledge of the barotropic component of flow. Direct deep measurements in various locations in the East Greenland current could identify this component.

Observational information pertaining to ice coupling with ocean models was discussed. Among these are ice-water stress, wind stress on ice and water, and the ice mass and velocity field. The concensus seems to be that multilevel models are more appropriate for these problems.

The following observational parameter needs were suggested for a mixed-layer type of model:

1. Temperature and salinity as functions of depth.

2. Latent and sensible heat flux available from temperature at 10 m.

3. Sea surface temperature of open water.

4. Incoming solar and back radiation measurements.

5. Ice thickness, compactness, snow cover, and albedo.

For mechanistic modeling efforts it seems that parameter ranges and means may be more important than the actual detailed fields.

It was agreed that the observationalists can provide the modelers with valuable input in the form of hypotheses to test in the mechanistic models.

ICE MODELING DISCUSSIONS

G. MAYKUT

Problems in modeling ice movement, decay, and breakup in the MIZ were discussed. The conversations focused on the types of data needed in formulating and testing mesoscale ice models. Of basic concern in dynamic modeling was the rheological behavior of the ice. What is an appropriate rheological model for the MIZ? Does the rheology vary across the region? How is it affected by the state (thickness, concentration, etc.) of the ice?

To answer such questions we need to observe the response of the ice to mechanical forcing under a range of environmental conditions. The data set should include: (1) ice velocity field on a variety of scales, both near the edge and in the interior, (2) surface stress obtained from the wind field and ice state, (3) water drag and its variations across the MIZ, (4) current field below the boundary layer, and (5) ice concentrations and thicknesses as a function of time and position.

While these quantities will be measured during MIZEX 84, there was some concern that data on floe rotation was being overlooked. Hayley Shen pointed out that grain rotations were a significant energy sink in models of granular media, and Ian Bratchie felt that floe rotation might be a contributing factor in floe breakup. There was considerable discussion regarding what would constitute an adequate data set and how it might be obtained. The conclusion was that it would be difficult to obtain a detailed view of rotation across the MIZ in 1984, but that it should still be possible to gather some useful information. It was recommended that efforts be made to obtain compass readings wherever possible. Such data would provide information as to whether rotations are random or organized on some scale. Sequential aerial photography in the vicinity of drifting ships could also be used to look at the details of rotation within relatively small regions as a function of compactness and floe size.

Modeling floe size distribution appears to be a particularly difficult problem, as the mechanisms that are responsible for floe breakup are not well understood, except near the ice edge. We discussed how these mechanisms might be identified more precisely during MIZEX. The best hope is to obtain good imagery across the region and then correlate temporal changes in floe size with data thickness, ice strain, wind and water stress, and floe rotation. Ideally the coverage should extend from the ice edge into the zone of large floes.

For modeling the thermodynamics of the summer MIZ, the most important variables are those that affect the absorption and distribution of shortwave energy within the system. For the ice cover these include ice concentration, thickness, surface albedo, and floe size distribution. Shortwave radiation that enters the ocean through leads and areas of thin ice causes melting to occur at both the edges and bottoms of floes and appears to be a major factor in the decay and retreat of the ice cover. However, little is known about the rate at which this heat is lost to the ice because the transport is complicated by waves, floe movements, mixed layer stratification, floe breakup, mechanical erosion, and lateral advection of ice and water across the edge. At this point we know so little about these processes that we are uncertain how to treat the interaction of shortwave radiation with the ice and ocean in mesoscale models.

To address these problems, we need to: (1) identify the principal mechanisms that transfer heat from the water to the ice and determine their relative magnitudes, (2) monitor how the decay pattern of the ice cover changes with concentration, thickness, floe size, dynamic activity, mixed layer stability, and so forth, and (3) define how ice decay and heat transfer processes vary across the MIZ. Of particular importance in understanding the heat and mass balance of the MIZ is data on spatial and temporal changes in the state of the ice cover, process studies in leads, and ablation data not only from the edge but also from the interior.

In addition to ice concentration, ice thickness and floe size distribution emerged as variables almost everyone would like to know. It was felt that thickness measurements, in particular, had not been given sufficient emphasis. Terry Tucker said that his group would need another person to obtain adequate ground-based thickness data. It was pointed out that submarine sonar data would (of course) be of great value in defining the thickness characteristics of the region, especially upstream of the region. It was suggested that laser profile data might also be helpful for estimating thicknesses and floe sizes.

Finally, it was noted that information on ice velocity upstream of the MIZEX experimental area would also be quite useful, and it was recommend that ARGOS buoys be air-dropped several hundred kilometers north of the main experimental region.

ATMOSPHERIC SUBGROUP DISCUSSIONS

E. ANDREAS

Surface fields

Surface fields of pressure (wind speed, stress), temperature, and humidity should be available in a timely manner for two reasons: (1) to serve as forcing conditions for numerical models, and (2) to provide the synoptic background for the MIZEX measurements, and thus guide the prioritizing of analyses.

Turbulence measurements in the surface layer

The sensible and latent heat fluxes should be measured in as many locations as possible, but especially near the ice edge in open water, where the fluxes will likely be largest. The surface stress should likewise be measured in many locations.

The bulk transfer coefficients for momentum, heat, and moisture, which are used to model the turbulent fluxes, should also be determined for as many surfaces as possible. The coefficients must then ultimately be related to some surface parameter, such as ice concentration, that is readily modeled.

Radiation measurements

The radiation fields, which are the main energy inputs to the surface in summer, are seemingly being overlooked. As a minimum requirement, global radiation should be measured on each ship. This would require only one radiometer per ship and someone to write down data once every hour.

It would also be relatively easy to make occasional aerial surveys of the global radiation to investigate its spatial variability.

An aircraft would also be an ideal platform from which to determine albedo, which is certainly quite variable across the MIZ. Airborne albedo measurements can be coupled with simultaneous surface photographs or in-situ surface observations to determine how the albedo depends on ice concentration, ice type and thickness, and surface conditions (wet or dry).

Cloud observations

To be of the most use, the radiation measurements must be complemented with detailed observations of the clouds. Thus, each ship should have a trained meteorological observer responsible for making hourly observations of cloud coverage, type, and height.

There are, of course, more sophisticated ways to make cloud observations. Sky cameras with timed shutters could be mounted on the ships. Radiosonde data should yield cloud heights and thicknesses. Or observers on MIZEX aircraft may have a better perspective on the clouds than surface observers.

A key use for the radiation measurements and this cloud data would be to check the cloud dependence in the radiative flux parameterizations used in most models. The cloud observations will also aid in identifying the existence of secondary atmospheric flow—sometimes recognizable as cloud streets.

Secondary flows, which are often associated with the abrupt changes in surface conditions found in the MIZ, affect the turbulent exchange in the atmospheric boundary layer and, thus, make the usual parameterizations of the surface fluxes suspect.

Radiosondes

Radiosonde soundings from ships working in the area will improve the synoptic analysis fields in the MIZEX region.

There are also many characteristics of the MIZ that can best be investigated with radiosondes. Cloud extents and any frontal structures associated with the ice edge are good examples. Radiosonde data will also facilitate verification of the similarity functions describing the vertical distributions of velocity and temperature within the atmospheric boundary layer. Because these were derived for more horizontally homogeneous conditions, it is not clear that the same functions apply in the MIZ.

Since the spatial derivative in the along-ice-edge direction is often ignored, there should be a two-dimensional radiosonde array to confirm this assumption. A minimum requirement is a line of three radiosonde stations across the ice edge: one in the ocean, a second at the ice edge within the ice, and a third deeper into the ice. The fourth station in the array should be at the ice edge along a line perpendicular to the across-edge line. Spacing between stations should typically be 50 km.

Because a slight change in wind direction can mean the difference between on-ice and off-ice winds, the radiosondes should be released simul-

taneously at intervals of no more than 6 hours. Any time a ship makes a crossing of the ice edge would be an ideal time for a transect of closely spaced radiosonde soundings.

Additional aircraft observations

The photo mosaics compiled for the Pilot Experiment show the potential value of aerial photography. From these photos the two-dimensional distribution of the open water fraction should be determined and made available to the many who need that information.

The transects of overlapping photos from the Pilot Experiment also suggest the use of stereoscopic photography to determine surface roughness. This is a quantity that the atmospheric investigators, the ice modelers, and the oceanographers can all use.

Laser profilometry is another method of obtaining surface roughness.

Ackley, Stephen, U.S. Army Cold Regions Research and Engineering Laboratory, 72 Lyme Road, Hanover, New Hampshire 03755. AV 684-4100, FTS 836-4100, (603) 646-4100, ext. 4258

Andreas, Edgar, U.S. Army Cold Regions Research and Engineering Laboratory, 72 Lyme Road, Hanover, New Hampshire 03755. AV 684-4100, FTS 836-4100, (603) 646-4100, ext. 4436

Bratchie, Ian, Scott Polar Research Institute, Lensfield Road, Cambridge, United Kingdom CB2 1ER. 66499, ext. 411

Budgell, W. Paul, Institute of Ocean Sciences, P.O. Box 6000, 8760 West Spanish Road, Sidney, British Columbia, Canada. (604) 656-8330

Cattle, Howard, United Kingdom Meteorological Office, London Road, Bracknell, Berkshire, United Kingdom RG12 257. 344-20242, ext. 2447 (TELEX 848160/847010)

Connors, Donald, Naval Underwater Systems Center, Newport, Rhode Island. (401) 841-3307

Hachmeister, Lon, Science Applications, Inc., 13400 Northrup Way, Suite 36, Bellevue, Washington 98005. (206) 747-7152

Hakkinen, Sirpa, Mesoscale Air-Sea Interaction Group, Meteorology Annex, Florida State University, Tallahassee, Florida 32306. (904) 644-6532

Hibler, William D. III, U.S. Army Cold Regions Research and Engineering Laboratory, 72 Lyme Road, Hanover, New Hampshire 03755. AV 684-4100, FTS 836-4100, (603) 646-4100, ext. 4287

Houssais, Marie-Noelle, Laboratoire Océanographie Physique, Museum d'Histoire Naturelle, 43-45 rue Cuvier, 75231 Paris, Cedex 05, France. 707-85-44

Johannessen, Ola, University of Bergen, Bergen, Norway. (47-5) 226973

Johnson, Leonard, Office of Naval Research, Code 425, 800 North Quincy Street, Arlington, Virginia 22217. AV 226-4118, (02) 696-4118/4119

Keffer, Thomas, Woods Hole Oceanographic Institute, Department of Physical Oceanography, Woods Hole, Massachusetts 02543. (617) 548-1400, ext. 2548

Lepparanta, Matti, Institute of Marine Research, P.O. Box 33, SF-00931, Helsinki 93, Finland

Lettau, Bernhard, National Science Foundation, 1800 G Street, N.W., Washington, D.C. 20550. FTS 357-7894

Ling, Chi-Hai, U.S. Geological Survey, Rm. 119, Thompson Hall, University of Puget Sound, Tacoma, Washington 98416. FTS 390-6516, (206) 593-6516

Markson, Ralph, Airborne Research Associates, 46 Kendall Common Road, Weston, Massachusetts 02193. (617) 899-1834

Martinson, Doug, Woods Hole Oceanographic Institute, Department of Physical Oceanography, Woods Hole, Massachusetts 02543. (617) 548-1400, ext. 2812

Maykut, Gary A., University of Washington, Department of Atmospheric Sciences AK-40, Seattle, Washington 98195. (206) 543-0164

Mellberg, Leonard, Naval Underwater Systems Center, Newport, Rhode Island. (401) 841-4260

Moritz, Richard E., Polar Science Center, University of Washington, Mail Stop JC-10, Seattle, Washington 98105. (206) 543-6613

Shen, Haley, Department of Civil and Environmental Engineering, Clarkson College of Technology, Potsdam, New York 13676

Smith, David C. IV., Department of Oceanography, Texas A&M University, College Station, Texas 77840. (409) 845-0543

Squire, Vernon, Scott Polar Research Institute, Lensfield Road, Cambridge, United Kingdom CB2 1ER. 66499, ext. 411

Symonds, Graham, Bedford Institute of Oceanography, P.O. Box 1006, Dartmouth, Nova Scotia, Canada. (902) 426-3584

Tucker, Walter, U.S. Army Cold Regions Research and Engineering Laboratory, 72 Lyme Road, Hanover, New Hampshire 03755. AV 684-4100, FTS 836-4100, (603) 646-4100, ext. 4268

Twitchell, Paul F., NAVAIR, Code 330G, Washington, D.C. 20301. AV 222-1967; (202) 692-2511

Wadhams, Peter, Scott Polar Research Institute, Lensfield Road, Cambridge, United Kingdom CB2 1ER. (223) 66716

Walsh, John, University of Illinois, Department of Atmospheric Sciences, 1101 West Springfield Avenue, Urbana, Illinois 61801. (217) 333-7521

Warn-Varnas, Alex, NORDA Code 322, N.S.T.L. Station, Mississippi 39529. (601) 688-4835

Weaver, Ron, National Snow and Ice Data Center, CIRES, Campus Box 449, University of Colorado, Boulder, Colorado. (303) 492-5171